Waterside Corrosion of Zircaloy Fuel Rods

NP-2789
Research Project 1250-1

Final Report, December 1982

EPRI-NP--2789

DE83 901120

Prepared by

KRAFTWERK UNION, AG
Hammerbacherstrasse 12 + 14
Postfach 3220
8520 Erlangen 2
Federal Republic of Germany

Principal Investigators
F. Garzarolli
W. Jung
H. Schoenfeld

COMBUSTION ENGINEERING, INC.
1000 Prospect Hill Road
Windsor, Connecticut 06095

Principal Investigators
A. M. Garde
G. W. Parry
P. G. Smerd

NOTICE

PORTIONS OF THIS REPORT ARE ILLEGIBLE. It has been reproduced from the best available copy to permit the broadest possible availability.

Prepared for

Electric Power Research Institute
3412 Hillview Avenue
Palo Alto, California 94304

EPRI Project Manager
H. Ocken

Materials and Corrosion Program
Nuclear Power Division

MASTER

DISTRIBUTION OF THIS DOCUMENT IS UNLIMITED

DISCLAIMER

Portions of this document may be illegible in electronic image products. Images are produced from the best available original document.

ORDERING INFORMATION

Requests for copies of this report should be directed to Research Reports Center (RRC), Box 50490, Palo Alto, CA 94303, (415) 965-4081. There is no charge for reports requested by EPRI member utilities and affiliates, contributing nonmembers, U.S. utility associations, U.S. government agencies (federal, state, and local), media, and foreign organizations with which EPRI has an information exchange agreement. On request, RRC will send a catalog of EPRI reports.

Copyright © 1982 Electric Power Research Institute, Inc. All rights reserved.

NOTICE

This report was prepared by the organization(s) named below as an account of work sponsored by the Electric Power Research Institute, Inc. (EPRI). Neither EPRI, members of EPRI, the organization(s) named below, nor any person acting on behalf of any of them: (a) makes any warranty, express or implied, with respect to the use of any information, apparatus, method, or process disclosed in this report or that such use may not infringe privately owned rights; or (b) assumes any liabilities with respect to the use of, or for damages resulting from the use of, any information, apparatus, method, or process disclosed in this report.

Prepared by
Kraftwerk Union, AG
Erlangen, Federal Republic of Germany
and
Combustion Engineering, Inc.
Windsor, Connecticut

EPRI PERSPECTIVE

PROJECT DESCRIPTION

The two primary goals of the EPRI core-materials subprogram are to improve core-component reliability and to extend fuel burnup. The latter issue is being addressed by projects that monitor fuel performance and projects that investigate specific phenomena which may limit the ability of current designs to achieve extended burnup. One such phenomenon, the corrosion of Zircaloy cladding, was investigated in this project (RP1250-1). Nondestructive and destructive examination techniques were used to obtain oxide film-thickness measurements. Destructive examination techniques were used to characterize pertinent physical and chemical properties of the oxide films.

PROJECT OBJECTIVES

The project was designed (1) to obtain extensive experimental measurements of Zircaloy corrosion under typical PWR operating conditions, (2) to identify the factors responsible for the observed difference between in-reactor corrosion rates and those deduced from specimens exposed in an autoclave, and (3) to develop a corrosion model with predictive capabilities. It was anticipated that such a comprehensive approach would permit an assessment of the importance of Zircaloy corrosion on fuel rod performance at extended burnup.

PROJECT RESULTS

Statistically significant measurements (from over 700 fuel rods) of Zircaloy corrosion were obtained. These data indicate that Zircaloy corrosion and related phenomena (e.g., hydrogen pickup) do not impose design or operating restrictions on PWR fuel rods operated through four cycles (~40 GWd/MTU). Additional data are needed to draw such a conclusion for operation through five cycles, but the limited data reported here are encouraging. The data suggest that the key determinants responsible for the observed in-reactor acceleration of Zircaloy corrosion are irradiation-induced damage in the oxide and thermal-hydraulic factors. The model development task suggests that additional work is needed. Sophisticated treatment of thermal-hydraulic effects is necessary if further progress is to be made.

This report should be of interest to utility personnel with responsibilities and interests in the areas of materials performance and thermal hydraulics of core components.

Howard Ocken, Project Manager
Nuclear Power Division

ABSTRACT

There is an economic incentive to extend average fuel-rod-discharge burnup to about 50 GWd/t. For these higher burnups it is necessary to know if increased waterside corrosion of the cladding will influence fuel-rod performance. For this reason, EPRI sponsored a joint program with C-E and KWU with the objective of investigating PWR waterside corrosion. This final report presents and discusses the results of various subtasks that comprised this project.

In the review of corrosion data and models in the literature it was concluded that the PWR environment enhances the corrosion rate by about three times that expected from ex-reactor tests. A nondestructive device was developed to measure oxide-film thickness present on a fuel rod. A large number of fuel rods were characterized in both spent-fuel-pool and hot-cell campaigns.

Chemical, physical and microstructural attributes of irradiated and unirradiated oxide films were measured. These included determinations of chemical composition, crystal structure, microstructure, density, specific heat, thermal conductivity, and post-irradiation autoclave corrosion behavior. It was concluded that there were no major differences between irradiated and unirradiated oxide films which could be attributed to the formation of the oxide in a PWR environment.

Procedures used to calculate the fuel-rod surface temperature were reviewed. Local variations in the oxide-film thickness, both axially and circumferentially, have been attributed to the presence of grids and differences in subchannel configurations which influence the local-heat-transfer coefficient which in turn affects the cladding temperature.

A model has been developed to predict in-reactor corrosion behavior. It adequately describes the performance of fuel rods in Reactors A and D but overpredicts corrosion in Reactors C and E. The observed differences in corrosion in different reactors may be related to differences in their thermal/hydraulic behavior.

It is concluded that the ability to extend the burnup of PWR fuel to ~50 GWd/t will depend on the specific fuel design and the thermal/hydraulic characteristics of individual cores.

ACKNOWLEDGMENTS

The efforts of many individuals at Combustion Engineering (C-E), Kraftwerk Union (KWU) and Battelle Columbus Laboratories (BCL), have all contributed greatly during the execution of this project.

The authors wish to thank G. W. Parry, C-E Program Manager and Dr. H. Stehle, KWU, Division General Manager, Fuel Element Laboratories for their help and guidance.

The work of the following individuals is gratefully acknowledged.

H. Basso, KWU	Hot Cell PIE Data
R. Eberle, KWU	Computer Analysis
D. Jorde, KWU	NDE Technique Development/Data Evaluation
H. Knaab, KWU	Report Review
R. Manzel, KWU	Data Evaluation
R. Riess, KWU	Coolant Chemistry Data
P. Suchy, KWU	T&H Analysis
H. Schoenfeld, KWU	Hot Cell PIE Data
M. G. Andrews, C-E	Review of Reports
R. N. Duncan, C-E	Review of Reports
J. R. Politano, C-E	Analysis of Data
D. B. Scott, C-E	Hot Cell PIE
B. Woodman, A. Kosmin and E. L. Filshtein, C-E	Development of Corrosion Model
R. C. Marshall, C-E	T&H Analysis
D. R. Farmelo, BCL	Hot Cell PIE
V. Pasupathi, BCL	Hot Cell PIE

CONTENTS

PART 1

Section		Page
1	INTRODUCTION	1-1
	References	1-3
2	IDENTIFICATION OF BACKGROUND DATA AND MEASUREMENTS	2-1
	Reactor Design and Operating Characteristics	2-1
	Primary Coolant Chemistry	2-1
	Pre-Irradiation Characterization of Zircaloy-4 Cladding	2-1
	Introduction	2-1
	Second Phase Particles	2-7
	Autoclave Corrosion Tests of Archive Cladding	2-7
	General Post-Irradiation Characterization of Fuel Cladding and Fuel Rods	2-11
	Background	2-11
	Fuel Rod Characterization	2-11
	Fuel Cladding Hydrogen and Nitrogen Content	2-13
	References	2-22
3	OXIDE FILM THICKNESS MEASUREMENTS	3-1
	Non-Destructive Examination (NDE) Techniques	3-1

CONTENTS (Cont'd)

Section		Page
	Background	3-1
	Equipment, Design and Operation	3-2
	Typical Results	3-5
	Destructive Examination Techniques	3-5
	Comparison of Non-Destructive (NDE) and Destructive Techniques	3-11
	Non-Destructive (NDE) Measurements	3-11
	Experimental Program	3-11
	Discussion of Data	3-11
	Conclusions	3-25
	References	3-26
4	CHARACTERIZATION OF THE OXIDE FILM	4-1
	Introduction	4-1
	Materials and Evaluation Techniques	4-2
	Results	4-8
	Microstructure of the Oxide Film	4-8
	Density, Specific Heat and Thermal Conductivity	4-17
	X-ray Diffraction	4-21
	Elemental Analyses of the Oxide	4-21
	Impedance Measurements	4-21
	Surface Area and Pore Volume - Measurements	4-24
	Autoclave Testing of Irradiated Fuel Cladding Samples	4-29

CONTENTS (Cont'd)

Section		Page
	Discussion	4-33
	Conclusions	4-37
	References	4-38
5	COOLANT CHEMISTRY EFFECTS	5-1
	Introduction	5-1
	Experimental	5-2
	Autoclave Electrochemical Measurements	5-2
	Mini-autoclave Corrosion Test with the Addition of Impurities	5-5
	Special Analyses of the PWR Coolant Chemistry	5-5
	Results	5-9
	Electrochemical Measurements	5-9
	Influence of Impurities on Corrosion	5-16
	Primary Coolant Chemistry	5-19
	Special Measurements of Impurities in the Reactor Coolant	5-19
	Discussion of Coolant Chemistry Effects	5-24
	Conclusions	5-26
	References	5-27

CONTENTS (Cont'd)

Section		Page
6	THERMAL-HYDRAULIC CALCULATIONS	6-1
	Introduction	6-1
	Survey of Correlations for Fully Developed Flow	6-1
	Influence of Spacer Grids	6-6
	Influence of Subchannel Geometry within the Fuel Assembly	6-7
	Circumferential Temperature Variations	6-14
	Conclusion	6-14
	References	6-16
7	ANALYSIS OF OXIDE THICKNESS DATA	7-1
	Introduction	7-1
	Statistical Analysis Methodology	7-4
	Results	7-6
	Discussion	7-15
	Conclusions	7-22
	References	7-24

PART 2

OXIDE THICKNESS DATA (microfiche insert, inside back cover)

ILLUSTRATIONS

Figure		Page
2-1	Distribution of Second Phase Particles in Various Tubing Lots	2-9
2-2	γ-Scan, Profilometry and Eddy Current Probe Hot Cell Results for One Cycle Rod 0801/62001, Reactor A, After a Burnup of 11,300 MWd/t	2-14
2-3	γ-Scan, Profilometry and Eddy Current Probe Hot Cell Results for 2 Cycle Rod 390/52001, Reactor A, After a Burnup of 22,500 MWd/t	2-15
2-4	Detailed Eddy Current Probe, Profilometry Results for 2 Cycle Rod 390/52001, Reactor A, After a Burnup of 22,500 MWd/t	2-16
2-5	Hydrogen Pickup of Zircaloy-4 in a PWR Environment	2-21
3-1	Schematic of the Principle of an ECT Oxide Thickness Probe (Proximity Probe)	3-3
3-2	Oxide Layer Thickness Measuring Device Shown Attached to the TV Camera	3-4
3-3	Schematic Showing the Oxide Layer Thickness Measuring Device in Operation in the Spent Fuel Pool Characterizing Peripheral Fuel Rods of a Fuel Assembly	3-6
3-4	Single Rod Oxide Film Thickness Measurement in the Spent Fuel Pool	3-7

ILLUSTRATIONS (Cont'd)

Figure		Page
3-5	Single Rod Oxide Film Thickness Measurement System (Probe Shown in Retracted Position)	3-8
3-6	Schematic Illustration of Poolside Eddy Current Examination Types	3-9
3-7	Oxide Layer Thickness Trace for a Fuel Rod After 3 Cycles of Irradiation	3-10
3-8	Metallographic Characterization of the Outer Oxide Layer of Rod 299/27152, Reactor A	3-12
3-9	Comparison of Oxide Film Measurements Using Both NDE and Metallography	3-13
3-10	Burnup Dependence of Corrosion	3-15
3-11	Oxide Layer Thickness as a Function of Burnup for Reactor A	3-16
3-12	Oxide Layer Thickness as a Function of Burnup for Reactor C	3-17
3-13	Oxide Layer Thickness as a Function of Burnup for Reactor D	3-18
3-14	Oxide Layer Thickness as a Function of Burnup for Reactor E	3-19

ILLUSTRATIONS (Cont'd)

Figure		Page
3-15	Influence of Rod Average Power on Zircaloy-4 Clad Oxide Layer Thickness at Peak Corrosion Position for 3 Cycle Rods of Reactors C, D and E	3-20
3-16	The Tubing Lot-to-Lot Dependence of In-Reactor Corrosion for Reactor A	3-21
3-17	Results of Successive Zircaloy-4 Clad Oxide Layer Thickness Measurements on Fuel Rods from Reactor D	3-22
3-18	Oxide Layer Thickness Measurements of Non-Fueled Rods from PWR-A	3-23
4-1	Equivalent Electrical Circuit for an Oxide with a Dense and a Porous Sublayer Used in Analysis of Impedance Data	4-7
4-2	SEM Micrograph of Cathodic Vacuum Etched Sample 3 Formed in PWR-A	4-11
4-3	Spherical Granule Cluster Structure of an Oxide Taken From the High Temperature Region of a Fuel Rod From PWR-A. The Metal was Removed and the Oxide Fractured (Sample 3)	4-12
4-4	Columnar and Spherical Granule Cluster Structure of an Oxide Taken From a Fuel Rod from a BWR. The Metal Was Removed and the Oxide Fractured (Sample 8)	4-13

ILLUSTRATIONS (Cont'd)

Figure		Page
4-5	Oxide/Metal Interface of an Oxide Taken From the High Temperature Region of a Fuel Rod From PWR-A. It was Fractured in Liquid Nitrogen While the Oxide was Still Attached to the Metal Substrate (Sample 3)	4-14
4-6	Surface of Oxide/Metal Interface of Stripped Oxide Samples From a Fuel Rod From PWR-A	4-15
4-7	View of Metal/Oxide Interface for a Sample From the Peak Temperature Position of a Fuel Rod From PWR-A (Sample 3). The Granular Structure is Fully Developed in the Interface Region	4-16
4-8	Thermal Conductivity of ZrO_2	4-20
4-9	Typical Impedance - Measurements in 1M H_2SO_4	4-23
4-10	Results of Impedance Measurements on Oxidized Samples	4-25
4-11	Comparison of Measured Roughness Factors With Literature Data	4-27
4-12	Porosity Distribution Curves Based on Desorption Hysteresis	4-28
4-13	Post-Irradiation Autoclave Corrosion Tests of Samples from a BWR	4-30

ILLUSTRATIONS (Cont'd)

Figure		Page
4-14	Post-Irradiation Autoclave Corrosion Tests of Samples from PWR-D	4-31
4-15	Post-Irradiation Autoclave Corrosion Tests of Samples from PWR-A	4-32
4-16	Summary of Post-Irradiation Autoclave Corrosion Tests	4-34
5-1	Primary Coolant Sampling System	5-7
5-2	Influence of Various Impurities on the Corrosion Potential of Oxidized Zircaloy in Pressurized Water (1.5 ppm Li, 600 ppm B) at 290°C	5-13
5-3	Comparison of the Polarization behavior of Oxidized Zircaloy and Platinum at 290°C in Pressurized Water (1.5 ppm Li, 600 ppm B and <10 ppb O_2)	5-14
5-4	Influence of Various Impurities in 290°C Water on the Polarization Behavior of Zircaloy Sample D pre-oxidized at 290°C for 750 days	5-15
5-5	SEM Examinations of Crud Formed in Reactors A and E Illustrating the Differences in Porosity	5-23
6-1	Influence of Water Flow Area to Total Cross-Sectional Area on Heat Transfer Characteristics of Tube Bundles.	6-4

ILLUSTRATIONS (Cont'd)

Figure		Page
6-2	Oxide Layer Thickness Profile, and Heat Transfer Coefficient Profile of Rod 365/41008, Reactor A	6-8
6-3	Comparison of Calculated Heat Transfer Coefficient with Empirical Correlations	6-9
6-4	Comparison of Measured and Calculated Oxide Layer Thickness Profile for a 4 Cycle Rod from PWR-D	6-10
6-5	Differences in the Subchannel Geometry within the Core Illustrated with a One Quarter Fuel Assembly Schematic	6-11
7-1	Comparison of the Predictions of the Dalgaard Model with Reactor A Corrosion Observations	7-2
7-2	Comparison of the Ex-Reactor Stehle Corrosion Model with the Reactor A Corrosion Observations	7-3
7-3	Methodology Used to Develop the Corrosion Model	7-5
7-4	Time Dependence of Corrosion (Pairwise Correlation)	7-9
7-5	Temperature Dependence of Corrosion (Pairwise Correlation)	7-10
7-6	Neutron Flux Dependence of Corrosion (Pairwise Correlation)	7-11
7-7	Burnup Dependence of Corrosion (Pairwise Correlation)	7-12
7-8	Flux Dependence of Corrosion (Temperature Constant)	7-13

ILLUSTRATIONS (Cont'd)

Figure		Page
7-9	Comparison of the Corrosion Predictions of Equations 7-1 to 7-4 with the Reactor A Observations	7-17
7-10	Comparison of the Corrosion Predictions of Equations 7-1 to 7-4 with the Reactor D Observations	7-18
7-11	Comparison of the Corrosion Predictions of Equations 7-1 to 7-4 with the Reactor C Observations	7-19
7-12	Comparison of the Corrosion Predictions of Equations 7-1 to 7-4 with the Reactor E Observations	7-20
7-13	The Interrelationship Between Measured Oxide Film Thickness and the Bias in the Prediction of Corrosion	7-23

TABLES

Table		Page
2-1	KWU PWR Thermal and Hydraulic Data	2-2
2-2	Cycle Length of Specific KWU Reactors	2-3
2-3	Reactor Coolant Inlet Temperatures	2-4
2-4	Primary Coolant Water Chemistry Data for Specific KWU Reactors	2-5
2-5	Typical Unirradiated Properties of Zircaloy Cladding Tubing	2-6
2-6	Tubing Lot Identification	2-8
2-7	Corrosion Tests of Archive Cladding in Water at 350°C	2-10
2-8	Summary of Hot Cell Examinations	2-12
2-9	Cladding H_2 and N_2 Content	2-18
2-10	Metallographic Data for Fuel Rods from Reactor A	2-19
2-11	Metallographic Data for Fuel Rods from Reactor D	2-20
3-1	Summary of NDE Measurements	3-14
4-1	Characteristics of Oxides Formed In-Reactor	4-3
4-2	Chemical Analytical Methods Employed for the Elemental Analyses of Oxide and Zircaloy	4-5

TABLES (Cont'd)

Table		Page
4-3	SEM Examination of Oxide Layer	4-10
4-4	Zirconium Oxide Density Data	4-18
4-5	Zircounium Oxide Specific Heat Data	4-19
4-6	Chemical Analyses of Zircaloy-4 Oxides formed in PWR's	4-22
4-7	Results of BET Measurements	4-26
5-1	Samples used for Electrochemical Measurements in 290°C Water	5-3
5-2	Aqueous Solutions Used in the Electrochemical Tests	5-4
5-3	Corrosion Media used for Tests in Mini-Autoclaves	5-6
5-4	Chemical Analytical Methods Used in the Analyses of Impurities in the PWR Coolant	5-8
5-5	Results of Corrosion Potential Measurements at 290°C for Samples A1 and A2.	5-10
5-6	Results of Corrosion Potential Measurements at 290°C for Samples A, B and C.	5-11
5-7	Results of-Corrosion-Potential Measurements at 290°C for Platinum and Zircaloy B and D Samples.	5-12

TABLES (Cont'd)

Table		Page
5-8	Influence of Impurities on Out-of-Pile Corrosion at 350°C in Mini-Autoclaves	5-17
5-9	Impurity Concentrations in the Primary Coolant of PWR-A and E	5-20
5-10	X-ray Diffraction and EDMA - Analysis of Circulating Crud From Reactors A and E.	5-22
6-1	Calculated Heat Transfer Coefficients for KWU Reactor A	6-3
6-2	Summary of Nusselt Number Correlations for fully developed Flow Conditions (Nu_∞)	6-5
6-3	Predicted Variation in Waterside Corrosion due to Differences between Subchannels within a Fuel Assembly	6-13
7-1	Relative Importance of Variables	7-7
7-2	Optimium Corrosion Equation Constants	7-16
7-3	Comparison of Model Predictions for the Different Reactors Examined	7-21

SUMMARY

There is an economic incentive to extend the average fuel rod discharge burnup to about 50 GWd/t. For these higher burnups, it is necessary to know whether the increased waterside corrosion of the cladding may decrease fuel rod reliability. It is apparent that many factors can influence the waterside corrosion and these need to be better understood in order to minimize corrosion at these higher target burnups. For this reason, EPRI sponsored a joint program with C-E and KWU to investigate PWR waterside corrosion under EPRI Contract RP 1250-01. This final report presents and discusses the results of various subtasks that comprised this project. These subtasks are:

A. Review of the literature data,

B. Nondestructive measurements of the thickness of oxide layers formed in-reactor,

C. Characterization of oxide films formed in- and ex-reactor,

D. Thermal conductivity measurements of oxide films formed in- and ex-reactor,

E. Development of a corrosion model.

The review of corrosion data and models in the literature was presented in an earlier report (1). It was concluded that the zirconium oxide corrosion film thickness strongly depends on burnup. Good agreement was observed between the oxide thickness values measured by a destructive metallographic technique and by the non-destructive eddy current technique. The PWR environment enhanced the corrosion rate by up to about three times that expected from ex-reactor tests. The enhancement factor varies from reactor to reactor and within a given reactor from cycle to cycle. Oxide film thermal conductivity and coolant chemistry were identifed as major factors influencing the corrosion behavior. The need for the thermal conductivity data on irradiated oxide was emphasized. Oxygen concentration in the coolant is known to enhance corrosion very strongly. Possible concentration of lithium in the oxide may result in a similar effect.

Oxide layer thickness data from Zircaloy-4 clad fuel rods irradiated to burnups up to 41.6 GWd/t in four KWU PWRs were compiled (2). Poolside nondestructive measurements using an eddy current probe were conducted (3). The axial variation in the oxide layer thickness was determined and distinct minima in the grid regions were observed. The post-transition hydrogen pickup fraction was found to be less than 16% of the theoretical or maximum value.

The results of Task C were presented in a report issued earlier (4). Post-irradiation autoclave corrosion tests were performed to determine the effect of prior in-reactor exposure on the subsequent out-reactor corrosion rate. Impurities were not found in the oxide in sufficient concentrations to suggest that they were responsible for the observed enhancement in corrosion. X-ray diffraction measurements on unirradiated and irradiated oxide films showed that oxides consist mainly of the monoclinic phase. Some line broadening was observed in the irradiated oxide implying irradiation damage in the oxide film. Transverse samples of the oxide films showed a lamellar structure with circumferentially oriented cracks. The oxides formed in PWRs had an equiaxed granular structure. The metal-oxide interface had a diffuse structure which was difficult to resolve. It was concluded that there are no major differences between oxides formed in the PWR environment and those formed during out-reactor autoclave corrosion tests.

The oxide density was measured by pycnometry and metallography. Corrosion in a PWR environment does not appear to significantly influence the oxide layer density. Specific heat measurements are consistent with the literature data and show that irradiation has no effect on the specific heat of zirconium oxide. The thermal conductivity of several oxide samples, formed in PWRs and in autoclaves, was measured. The thermal conductivity of the autoclave oxide samples varies between 1.9 to 2.4 w/m.K with little or no temperature dependence from room temperature to 650°C. The thermal conductivity of three irradiated oxide films ranged from 1.5 to 2.0 w/m.K, which is a reduction of approximately 30% over the unirradiated values.

Electrochemical measurements show that some impurities in the coolant, for example O^{2-}, Cr^{6+}, and NO_3^-, can have a strong influence on corrosion potential and may therefore affect the corrosion rate of Zircaloy in water at 350°C. However, the concentration levels of these impurities necessary to observe the enhanced corrosion are well above those measured in the coolant. Therefore the in-reactor corrosion enhancement cannot be explained on the basis of the coolant chemistry effects.

Procedures used to calculate the fuel rod surface temperature under non-boiling conditions were reviewed (3). A reasonable correlation was found between oxide layer thickness measurements and temperatures calculated by using a local heat transfer coefficient. The local variation in the thermal-hydraulic conditions, i.e. the heat transfer coefficient, may be responsible for the axial and circumferential variation of oxide film thickness on fuel rods. The thermal-hydraulic models for the calculation of the heat-transfer coefficient have been refined. The axial variation of the heat transfer coefficient has been modelled. Preliminary analysis of a fuel assembly from Reactor A indicates that differences between subchannels of PWR fuel may lead to a variation of up to 20% in the corrosion of fuel rod operating at a given power level.

As part of the development of the corrosion model, all oxide layer thickness measurements were incorporated to an automated data base. The time/temperature history at the metal/oxide interface was calculated using simulator calculations with simplifying assumptions. An analysis using correlation coefficients revealed that the temperature of the metal/oxide interface is the most important variable influencing the corrosion rate while for the oxide layer thickness, time, temperature and burnup were all important variables. Pairwise analyses were conducted to evaluate the data trends. The optimized corrosion model is derived in terms of pre-transition and post-transition corrosion rates as well as the thickness at transition as functions of important variables (temperature, neutron flux) and empirical constants. The model predicts the data from Reactor A and D very well. However, for Reactor C and E data the agreement between observed and predicted values is poor. It is concluded that additional improvements in the thermal and hydraulic calculations to account for the temperature dependent heat transfer coefficient, subchannel effects, and local grid effects would improve the corrosion model. The observed differences in the corrosion in different reactors may be related to the differences in the thermal hydraulic behavior of the reactors.

REFERENCES

1. F. Garzarolli, D. Jorde, R. Manzel, G. W. Parry and P. G. Smerd. CE/KWU/EPRI. "Review of PWR Fuel Rod Waterside Corrosion Behavior,"RP 1250-1. Task A. Combustion Engineering, Inc., June 1979, CE NPSD-79, August 1980, EPRI NP-1472.

2. F. Garzarolli, R. Manzel, P. Suchy and J. R. Politano. CE/KWU/EPRI "Recent PWR Waterside Corrosion Data Acquisition and Review of Clad Surface Temperature Calculation," RP 1250-01, Combustion Engineering, Inc., June 1981, CE NPSD-140.

3. H. D. Goddard, J. P. Lareau, T. R. Slade, P. A. Van Saun and R. G. Weber, CE/KWU/EPRI. "Non-Destructive Measurement of Zirconium Oxide Corrosion Films on Irradiated Zircaloy Clad Fuel Rods." RP 1250-01. CE NPSD-102. Combustion Engineering, Inc., June 1981.

4. F. Garzarolli, H. Schoenfeld, D. B. Scott and P. G. Smerd. CE/KWU/EPRI Task C Interim Report. "Characterization of Zirconium Oxide Corrosion Films on Irradiated Zircaloy Clad PWR Fuel Rods." RP 1250-01. Combustion Engineering, Inc., NPSD-192.

PART 1

Section 1

INTRODUCTION

The waterside corrosion of Zircaloy fuel cladding does not limit the operation of PWRs for typical coolant conditions and design burnups of ~35 GWd/t. The current trends in the nuclear industry are to increase coolant inlet temperatures to improve thermal efficiency and to extend design burnups to 50 GWd/t to decrease fuel cycle costs and to reduce spent fuel storage requirements. Such modifications will increase Zircaloy waterside corrosion. It is essential to estimate the amount of corrosion under these more demanding conditions and to evaluate its effects on the proposed new design limits. The broad objectives of this program are:

- to obtain a data base on Zircaloy corrosion,
- to characterize the physical and chemical properties of the corrosion films in this operating regime and
- to develop an analytical correlation that predicts the in-reactor corrosion of Zircaloy-4 in PWR environments.

The resulting data base and corrosion model can then be used to estimate the corrosion performance of PWR fuels operating to extended exposures.

This final report summarizes the work done under EPRI Contract RP 1250-01. Parts of this work were presented in earlier reports (1 - 7). Section 2 presents the background information needed to analyze the corrosion data and includes reactor design and operating characteristics, primary coolant chemistry, preirradiation characterization of Zircaloy-4 cladding, and general post-irradiation characterization of fuel cladding and fuel rods.

Section 3 describes the oxide film thickness measurements. The equipment and results using the non-destructive eddy current technique are described. The destructive metallographic technique is discussed and the results are presented. The non-destructive and destructive technique results are compared.

The results of the oxide film characterization program are discussed in Section 4. Several chemical and physical properties of the corrosion films were evaluated. Experimental techniques used and the results obtained are presented. The influence of coolant chemistry on Zircaloy corrosion is discussed in Section 5. The thermal-hydraulic calculations are described in Section 6. Correlations for fully developed flow are summarized and influences of spacer grids and subchannel geometry within the fuel assembly are discussed. The analysis of the oxide thickness data is presented in Section 7. A corrosion model is derived on the basis of statistical analysis methods.

REFERENCES

1. F. Garzarolli, D. Jorde, R. Manzel, G. W. Parry and P. G. Smerd. C-E/KWU/EPRI "Review of PWR Fuel Rod Waterside Corrosion Behavior" RP 1250-01. Task A. Combustion Engineering, Inc., June 1979, CE NPSD-79, August 1980, EPRI NP-1472.

2. F. Garzarolli, R. Manzel, P. Suchy and J. R. Politano. CE/KWU/EPRI "Recent PWR Waterside Corrosion Data Acquisition and Review of Clad Surface Temperature Calculation," RP1250-01. Combustion Engineering, Inc., June 1981, CE NPSD-140.

3. F. Garzarolli, D. Jorde, R. Manzel, J. R. Politano and P. G. Smerd. "Waterside Corrosion of Zircaloy Clad Fuel Rods in a PWR Environment", Zirconium in the Nuclear Industry - Fifth Conference, ASTM STP 754, D.G. Franklin, Ed; 1982 pp 430-449.

4. F. Garzarolli, P. Suchy and P. G. Smerd. "Observations and Analysis of the Corrosion Behavior of PWR Fuel", Proc. ANS Topical Meeting on LWR Extended Burnup - Fuel Performance and Utilization, Williamsburg, Virginia April 4-8, 1982.

5. H. Stehle, F. Garzarolli, A. M. Garde and P. G. Smerd. "Factors Contributing to the In-reactor Waterside Corrosion of Zircaloy", Paper Presented at the 6th ASTM International Conference on Zirconium in the Nuclear Industry, Vancouver B.C., Canada, July 1, 1982.

6. F. Garzarolli, H. Schoenfeld, D. B. Scott and P. G. Smerd. C-E/KWU/EPRI, Task C Interim Report "Characterization of Zirconium Oxide Corrosion Films on Irradiated Zircaloy Clad PWR Fuel Rods". RP 1250-01. Combustion Engineering, Inc., May 1982, CE NPSD-192.

7. H. D. Goddard, J. P. Lareau, T. R. Slade, P. A. Van Saun and R. G. Weber. CE/KWU/EPRI, "Non-destructive Measurements of Zirconium Oxide Corrosion Films on Irradiated Zircaloy Clad Fuel Rods", RP 1250-01. Combustion Engineering, Inc., June 1981, CE NPSD-102.

Section 2

IDENTIFICATION OF BACKGROUND DATA AND MEASUREMENTS

The data presented in this section provide background information required to analyze the fuel rod corrosion information presented later.

REACTOR DESIGN AND OPERATING CHARACTERISTICS

The reactor and fuel design and operating characteristics that influence corrosion behavior are listed in Table 2-1 (1). This table shows that the fuel clad outer diameter and wall thickness are a constant 1.075 cm (0.423 in.) and 0.0725 cms (0.029 in.) respectively, while the active fuel length varies by almost 50%, from 265.0 cm in Reactor C to 390.0 cm in Reactor D. The number of spacer grids per fuel assembly is 7 in Reactors B, C and E, 8 in Reactors A and F, and 9 in Reactor D.

The cycle lengths of the reactors are summarized in Table 2-2 in effective full power days (EFPD). The reactors were predominantly operated in a base load scheme at full power. The nominal coolant inlet temperature, which varied little from cycle to cycle, is given in Table 2-3.

PRIMARY COOLANT CHEMISTRY

The most important features of the primary coolant chemistry of the six reactors are summarized in Table 2-4, which gives the range of actual measured values for the various reactor cycles. The measurements will be discussed in more detail in Section 5.

PRE-IRRADIATION CHARACTERIZATION OF ZIRCALOY-4 CLADDING

Introduction

Standard KWU Zircaloy-4 cladding was employed in the fabrication of the fuel rods. The typical properties of the unirradiated material are summarized in Table 2-5.

Table 2-1

KWU PWR THERMAL AND HYDRAULIC DATA

Reactor	Power MW(th)	Fuel Assembly Type*	No. of FA's	No. of Spacer Grids	System Pressure (bar)	Coolant Flow Rate (kg/s.rod)	Active Length (cm)	Fuel Rod Diam. (cm)	Cladding Thickness (cm)
A	1044	14x14	121	8	149	0.292	270.0	1.075	0.0725
B	1891	15x15	157	7	155	0.353	298.5	1.075	0.0725
C	1365	15x15	121	7	155	0.375	265.0	1.075	0.0725
D	3540	16x16	193	9	155	0.426	390.0	1.075	0.0725
E	2360	15x15	177	7	155	0.393	298.5	1.075	0.0725
F	2806	15x15	177	8	158	0.381	340.0	1.075	0.0725

*Fuel Rods x Fuel Rods

Table 2-2

CYCLE LENGTH OF SPECIFIC KWU REACTORS

CYCLE LENGTH IN EFFECTIVE FULL POWER DAYS (EFPD)

Cycle No.	A	B	C	D	E	F
1	512	409	357	432	315	304
2	272	233	298	254	261	294
3	290	312	275	312	258	
4	307		270	282	223	
5	298		306		227	
6	268					
7	302					
8	301					
9	285					
10	317					
11	290					

Table 2-3

REACTOR COOLANT INLET TEMPERATURE

COOLANT INLET TEMPERATURE (°C)

Cycle No.	A	B	C	D	E	F
1	281	290	289	283	291	293
2	281	290	289	283	291	293
3	281	290	289	283	290	
4	281		289	283	291	
5	282		289		291	
6	282					
7	283					
8	283					
9	283					
10	283					
11	284					

Table 2-4

PRIMARY COOLANT WATER CHEMISTRY DATA FOR SPECIFIC KWU REACTORS

Reactor	Cycle	Conductivity at 25°C (Mhos/cm)	pH Value (RT)	Lithium (ppm)	Hydrogen (ppm)	Oxygen (ppb)	Chloride (ppb)	Ammonia (ppb)	Nitrate (ppb)	Iron (ppb)
A	2	2-10	5-6	0-0.1	0.3-1.0	<40	<200	<1000	NM	<10-60
	3	2-20	6-7	1-2	3.2-3.8	<10	<200	<1000	NM	<10-40
	4	5-25	5-7	0-1.9	2.4-4.6	<5	<100	<1000	NM	<10-50
	5	10-25	6	0-1.1	2.4-2.6	<5	<100	<1000	NM	<10-100
	6	20-35	6-7.5	1-2	2.4-3.0	<5	<100	<1000	NM	<10-100
	7	10-35	6-7.5	1-2	1.8-3.4	<5	<100	<1000	NM	<10-100
	8	10-35	5.2-8	1-2	2.6-4.0	<5	<100	<1000	NM	<10-70
	9	10-35	5.2-8	1-2	2.6-3.0	<5	<100	<1000	NM	<10-50
	10	10-35	4.5-8	1-2	2-4	<5	<100	<1000	NM	<10-50
	11	10-35	5-8	1-2	2-4	<5	<100	<1000		
B	1	25	6-7	1.4(0.1-2.5)	3.7(0.3-4.9)	25	20-100	<1000	NM	NM
	2	25	7-8	1.5(0.1-2.9)	3.2(0.6-4.4)	-		-	NM	NM
	3	25	5-5	1.3(0.1-3.9)	3.3(0.3-3.9)	20,1200	50	500	NM	NM
C	1	10-25	6	1-1.5	2-4	<5	<200	<500	NM	<5-40
	2	10-25	5-7	1-2	2-4	<5	<200	<500	NM	<5-40
	3	10-25	5-8	1-2	2-4	<5	<200	<500	NM	<5-40
	4	10-25	6-8	1-2	2-4	<5	<200	<500	NM	<5-40
	5	10-25	6-8	1-2	2-4	<5	<200	<500	NM	<5-40
D	1	10-40	6-7	0.2-2	1.6-2.0	<5	<200	<20-70	NM	<5-100
	2	10-25	NA	1-2	2.4-3.4	<5	<200	<500	NM	<5-100
	3	10-25	NA	1-2	2-4	<5	<200	<100-500	NM	<5-100
	4	10-25	NA	1-2	2-4	<5	<200	500	NM	<5-100
E	1	15-25	6.5-7.5	1-2	2-3.1	<10	25-50	500-1000	NM	<5-40
	2	15-25	6.2-7.1	0.7-1	2.1-3.3	<10	25-100	50-300	<5-20	<5-40
	3	15-25	6.5-8.5	0.7-1	1.6-4.3	<10	<200	50-300	<5-30	<5-40
	4	15-25	6.6-7.1	0.7-1	2.3-3.7	<2	<200	200-1000	10-200	<5-40
	5	15-25			2-4	<2	<200	<500	NM	<5-40
F	1	NA	NA	1-2	2-4	<1	<200	NM	NM	<10-50
	2	NA	6.5-8.2	1-2	1.5-3.5	<1	<200	NM	NM	<10-50

NA - Not available
NM - Never measured

Table 2-5

TYPICAL UNIRRADIATED PROPERTIES OF ZIRCALOY-4 CLADDING

Property		Value	Property	Value
Chemical Analysis			Microstructure	
Sn	wt %	1.55	% recrystallized	2%
Fe	wt %	0.21		
Cr	wt %	0.12	Texture	
O	wt %	0.12		
			Ø angle	40°
Al	ppm	49	Max relative intensity	5
Pb	ppm	<25		
B	ppm	0.2	OD Surface Roughness (μm)	2.0
Cd	ppm	<0.2		
Ca	ppm	<10	Corrosion Test in Steam at 400°C	
Cl	ppm	<5		
Co	ppm	<10	Wt gain after 3 days for	
Hf	ppm	64	as-received material (mg/dm^2)	19
C	ppm	130		
Cu	ppm	16	Wt gain after 3 days for pickled	
Mg	ppm	<10	tubing (mg/dm^2)	15
Mn	ppm	<25		
Ni	ppm	<35		
N	ppm	35		
Ti	ppm	<25		
V	ppm	<25		
H	ppm	21		
W	ppm	<25		
U	ppm	1.7		
Nb	ppm	<50		
Si	ppm	67		

The identity of the Zircaloy-4 tubing lot numbers and the fuel rod identification numbers are given in Table 2-6. This information is available for specific test fuel assemblies or characterized standard fuel assemblies.

Second Phase Particles

Some limited measurements of the second phase particle size and distribution in both Zircaloy-4 and Zircaloy-2 were made using both transmission electron microscopy (TEM) and scanning electron microscopy (SEM). The results, given in Figure 2-1, show that generally there is not a large variation in tubing from lot-to-lot, although Lot x appears to have a larger number of very fine second phase particles.

Autoclave Corrosion Tests of Archive Cladding

The objective of these tests was to determine the lot to lot variability in the corrosion behavior of the as-received tubing.

Experimental Details. 50 mm long tubing samples were machined from archive tubes. The tubing outer surface was either in the abraded or electropolished condition to reflect the surface condition of the fuel rods tested in-reactor. These samples were capped by welding end plugs to both ends of the tubing section. Additional samples were also pickled to determine the corrosion behavior of the base metal; 30 μm was removed by pickling in a HNO_3 - HF solution. With the exception of the pickled specimens all samples were tested in duplicate.

A 10 liter stainless steel static autoclave was used. The corrosion tests were conducted at 350°C in deionized water and the samples examined after cumulative exposures of 7, 14, 30, 60, 121, 180, 240, 300 and 360 days.

Prior to each autoclave test cycle, the autoclave was purged with argon gas, evacuated and an overpressure of 0.25 bar hydrogen and 5 bar argon maintained; this resulted in <0.01 ppm oxygen in the coolant. In the last autoclave cycle an initial oxygen level of 500 ppm was present in the water.

Results and Discussion. Based on these measurements the time to transition was estimated to be in the range 60-130 days. A transition time of 180 days was predicted by the equations in Appendix B of reference 1. Once the change to post-transition kinetics occurred the corrosion rate was constant. The results are given in Table 2-7. The mean corrosion rate was 0.25 mg/dm^2-day. This is in close

Table 2-6

TUBING LOT IDENTIFICATION

Lot No.	Reactor	Reactor Cycle	Fuel Assembly No.	Fuel Rod Identification
1	A	4,5	247/365	42, 43, 45, 53, 67, 71, 79, 82, 98, 103, 105, 109, 122, 150
2	A	4,5	249	P37, P122, P133
3	A	5,6,8	281	147, 152, 188, 548, 867
4	A	6-8,10	317/390	0404, 0504, 0509, 0512, 0601, 0607, 0609
5	A	6-8	317	0905 1001 1005
6	A	7-11	365/390 0801/0901	36001, 36003, 36005, 36006, 37001, 38001, 40002, 40004, 40006, 41008, 42003, 43001, 43002, 43004, 45003, 45003, 45004
7	A	7-9	363/364 365/366	46001, 48002, 48003, 49001, 50001
8	A	8-11	390/0801	52001, 52002, 52004, 53001, 53002, 53004, 58001, 58003, 59023
9	A	8-10	390	56003, 57003
10	A	9-11	0801	60001, 62001, 62002, 63001, 63002, 63003, 64001, 64002
11	C	3-5	181	all fuel rods in the fuel assembly
12	C	3-4	157	all fuel rods in the fuel assembly
13	D	1-3	193	all fuel rods in the fuel assembly
14	D	1-4	191	all fuel rods in the assembly
15*	CC-I	1-4	BT01/02	

*From another EPRI - Program.

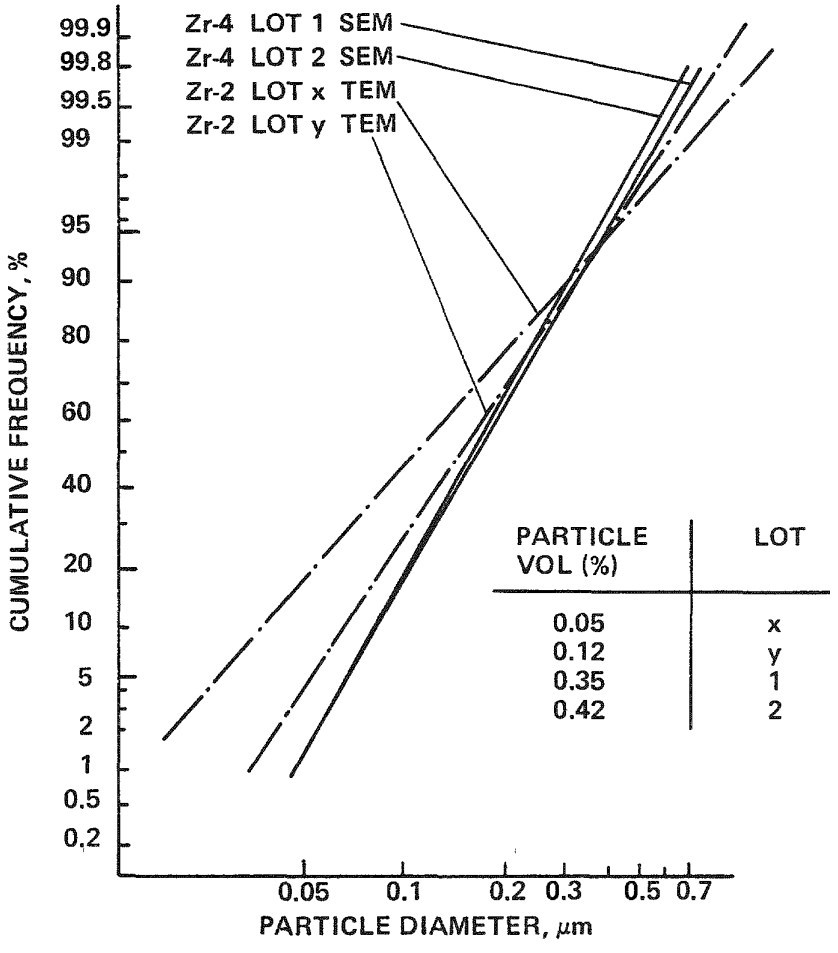

Figure 2-1. Distribution of Second Phase Particles in Various Tubing Lots

Table 2-7

CORROSION TESTS OF ARCHIVE CLADDING IN WATER AT 350°C

Lot Number	O.D. Surface Treatment	Corrosion Rate of as received material (mg/dm^2-d)		Corrosion rate of pickled tubes (mg/dm^2-d)	
		120-300 days(1)	300-360 days(2)	120-300 days(1)	300-360 days(2)
1	Electropolished	0.242	0.45	0.285	0.163
10	Electropolished	0.223	0.515	0.270	0.202
11	Electropolished	0.273	0.458	0.305	0.413
12	Electropolished	0.275	0.456	0.305	0.452
13	Electropolished	0.238	0.381	0.272	0.188
14	Electropolished	0.247	0.362	0.283	0.177
Mean		0.25	0.433	0.287	0.265
One Sigma		0.02	0.06	0.02	0.13
2	Ground	0.217	0.318	0.187	0.383
3	Ground	0.264	0.168	0.250	0.240
4	Ground	0.176	0.350	0.171	0.090
5	Ground	0.217	0.372	0.283	0.148
6	Ground	0.271	0.373	0.187	0.473
7	Ground	0.235	0.552	0.265	0.333
8	Ground	0.297	0.561	0.309	0.405
9	Ground	0.202	0.298	0.256	0.222
15	Ground	0.224	0.429		
Mean		0.234	0.380	0.239	0.287
One Sigma		0.04	0.01	0.05	0.13

(1) O_2 <0.01 ppm (2) O_2 400 ppm.

agreement with the predictions of the equations in Appendix B of Reference 1 of 0.28 mg/dm^2-day. The tubing surface treatment did not appear to significantly change the corrosion behavior. The standard deviation associated with the corrosion rate was only 0.019 mg/dm^2-day (8%) for electropolished or abraded tubing while the standard deviation for pickled tubing was 0.039 mg/dm^2-day (16%). Corrosion was generally higher under oxygenated conditions for samples having an electropolished or ground surface finish; the corrosion rate of pickled samples only increased slightly.

GENERAL POST-IRRADIATION CHARACTERIZATION OF FUEL CLADDING AND FUEL RODS.

Background

Fuel rods examined in this program operated over range of powers from 40 W/cm to 340 W/cm and burnups ranging from 3.3 GWd/t to 45 GWd/t. The cladding fluence exposure varied from 0.5 x 10^{21} n/cm^2 to 9 x 10^{21} n/cm^2 (E>0.821 MeV)*.

After completing their irradiation the fuel rods were examined in the reactor pool. Fuel rods from Reactors A and D were then sent to the KWU hot cells for a detailed inspection; in some cases this included a destructive examination. These rods had axially averaged burnups of 11.2-41.6 GWd/t. A summary of the work conducted is presented in Table 2-8. A brief description of the techniques employed may be found in Reference 2.

Fuel Rod Characterization

Visual Inspection. The visual inspection revealed that the fuel rods from all Reactors (A to F) were essentially crud free; some had a light dusting of powdery crud. The one-cycle rods had black, pre-transition oxide layers on the lower half of the rod, followed by a zone with mixed black and gray coloration; the upper third of the fuel rod had a gray, post-transition coloration. The upper plenum region of the rod was black. The axial height at the region where the color change is observed decreases with increasing exposure.

Eddy Current Defect Testing. Eddy current defect testing verified rod integrity; no defects in the cladding were observed.

---

* 1 x 10^{21}(E > 0.821 MeV) = 0.89 x 10^{21}(E> 1 MeV)

Table 2-8

SUMMARY OF HOT CELL EXAMINATIONS

Reactor	Fuel Rod Identification	Exposure EFPD	Exposure MWd/MTU	Visual	E.C. Defect Testing	γ-scan	Profilometry	E.C. Oxide	Metallography
A	0801/62001	285	11300		X	X	X	X	2
	63001	285	11200					X	X
	64002	285	11200						X
	247/365/67	906	41600					X	3
	299/27152	1156	35200	X	X		X	X	2
	28245	1156	35200	X	X	X	X	X	
	317/0512	871	31800						X
	0609	871	31200						X
	365/40006	888	31500			X	X	X	
	43002	603	22600					X	X
	43004	888	31300					X	X
	46001	603	22700					X	X
	390/52001	586	22500			X	X	X	X
	52002	301	11500						X
	53001	586	21700						X
	53002	301	11500						X
D	47/12125	432	17300					X	X
	89/8000	998	35600	X			X	X	X
	8534	998	35600	X	X	X	X	X	
	96/11475	686	26100						X

Integral Gamma Scanning. Integral gamma-scanning was used to determine the axial power profile for the one-cycle rod and the axial burnup profile for the multiple-cycle rods.

For the one-cycle rod, the gamma profile in Figure 2-2 represents mainly the power for the last quarter of the cycle, because of the dominant contribution of the short-lived isotopes Ba/La 140, Ce/Pr 141, and Zr/Nb 95.

Axial burnup profiles, (Figure 2-3) were determined for the multi-cycle rods. The dominant contributions are from long-lived isotopes Ce/Pr 144, Ru/Rh 106, and Cs/Ba 137.

Profilometry. Profilometry showed the fuel rod diameters decrease with increasing exposure. This irradiation-induced creepdown is a response to the coolant pressure and is illustrated in Figure 2-2. A detailed section (between grids 5 and 6) of a trace is given in Figure 2-4. The oxide measurements made on this rod are also given in Figure 2-2. The measurement technique and the results will be discussed in more detail in Section 3. However, knowledge of the oxide layer thickness allows the diametral measurements to be corrected for the presence of the oxide*. This procedure allows a distinction to be made between dimensional changes due to clad creep and growth and those due to oxidation.

After correcting for the increase in diameter due to oxidation, relatively uniform creepdown over the rod length was observed. Generally rods had thick oxides between grids and thinner oxides at grid positions, and locally less creepdown was observed at the spacer grid positions. This observation is consistent with the relationship between clad creep and clad temperature; higher creepdown at the peak corrosion position is due to the thermal barrier effect of the oxide. This effect was most readily observed on multi-cycle rods with oxide layer thicknesses >20 μm.

Fuel Cladding Hydrogen and Nitrogen Content

During the corrosion process oxygen from the water reacts to form a layer of ZrO_2 on the surface of the tubing, while some of the hydrogen diffuses through the oxide and is taken up by the base metal. The hydrogen uptake was measured primarily by

---

* For Zr, the Pilling-Bedworth ratio is 1.56 (volume of oxide formed per unit volume of metal.

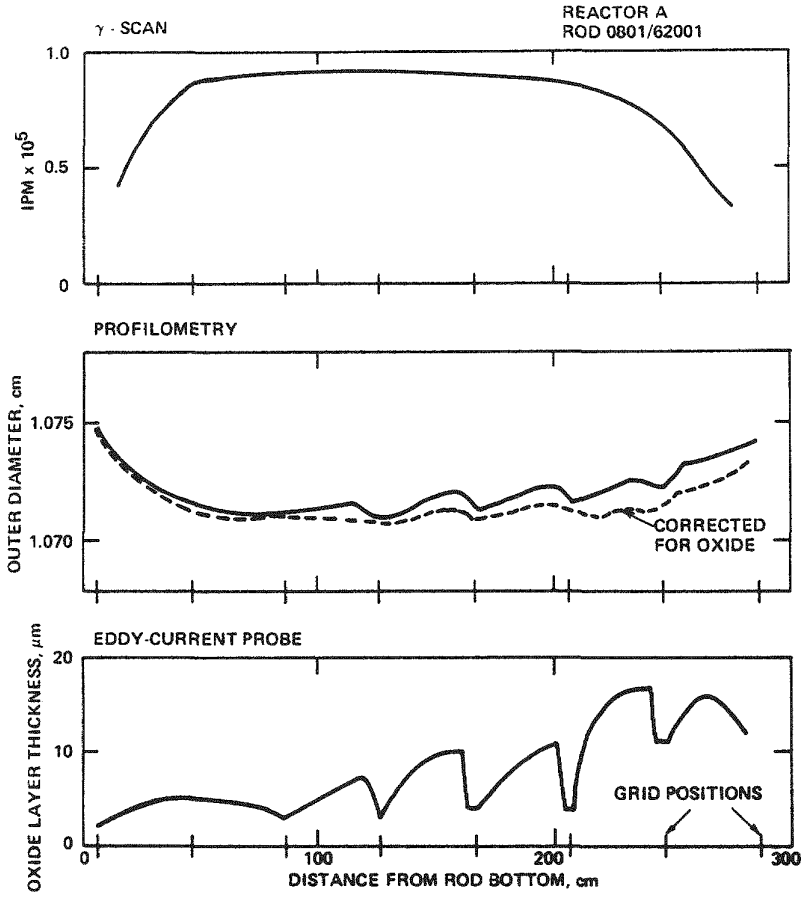

Figure 2-2. γ-scan, Profilometry and Eddy Current Probe Hot Cell Results for One Cycle Rod 0801/62001, Reactor A After a Burnup of 11,300 MWd/t

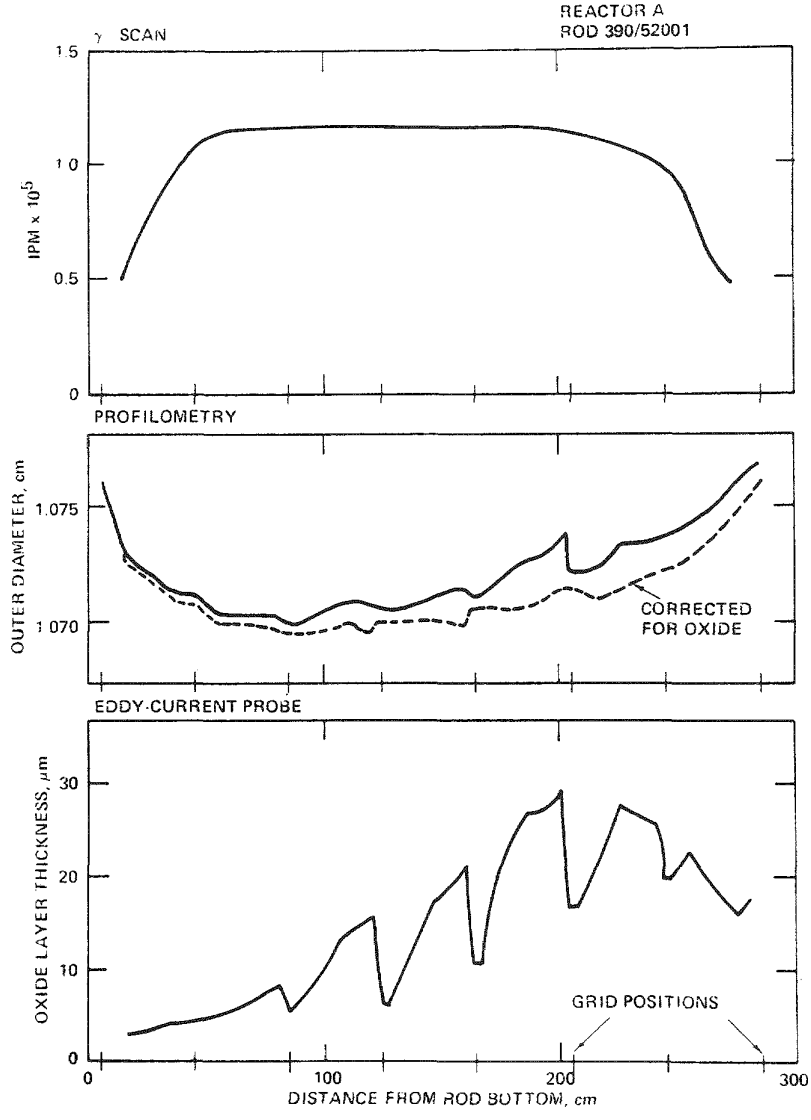

Figure 2-3. γ-scan, Profilometry and Eddy Current Probe Hot Cell Results for 2 Cycle Rod 390/52001, Reactor A, After a Burnup of 22,500 MWd/t

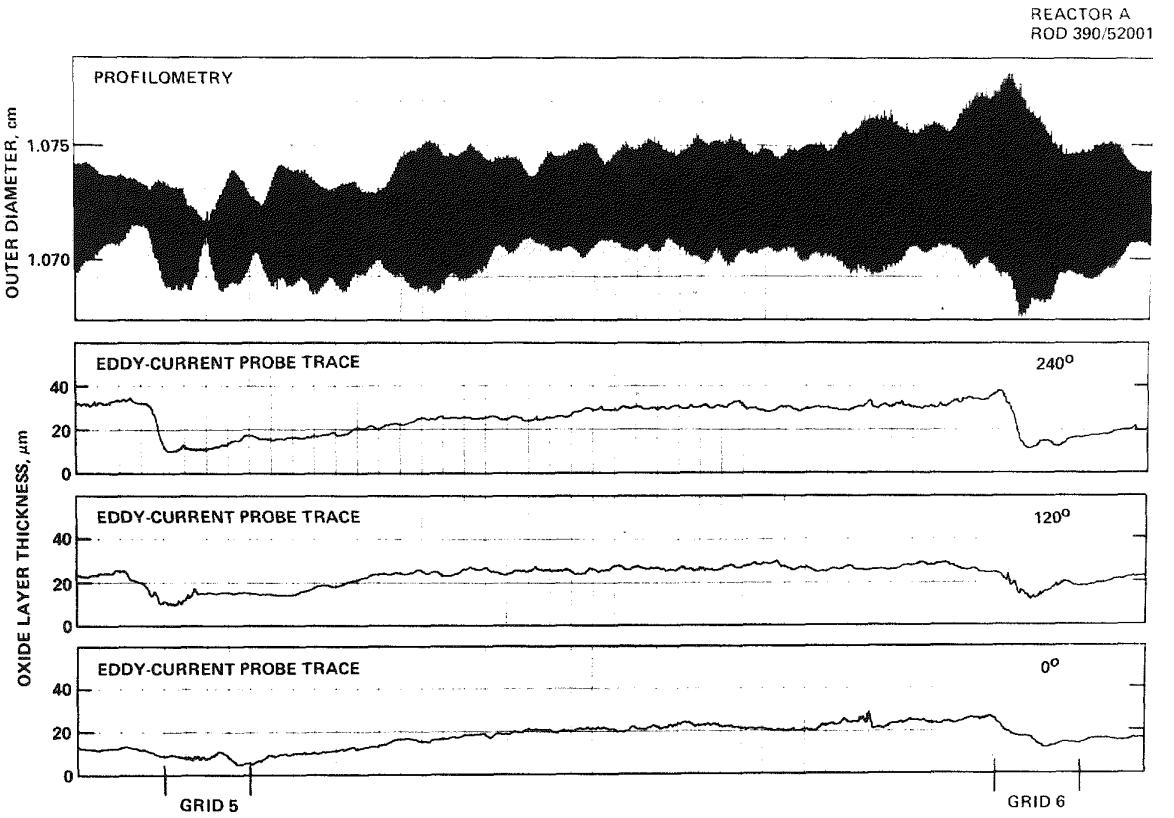

Figure 2-4. Detailed Eddy Current Probe, Profilometry Results for 2-Cycle Rod 390/52001, Reactor A, After a Burnup of 22,500 MWd/t

metallography; the hydrogen content was estimated by comparing the hydride distribution and appearance with known visual standards. The metallographic technique has already been described in Reference 2. These estimates were checked by conducting hot extraction gas measurements on some samples. This latter technique also was used to determine whether there was nitrogen pickup in the cladding. In the hot extraction measurements 0.1 gm samples of tubing were heated in a platinum crucible and the evolved gases analysed by mass spectroscopy.

The hot extraction data for the irradiated samples are presented in Table 2-9. No nitrogen was picked up during the corrosion process. As expected there was an increase in the hydrogen content. The hydrogen levels measured by hot extraction agree with those estimated from metallography. The oxide layer thickness measurements, as well as the estimated hydrogen concentrations for the rods of Reactor A, are listed in Table 2-10. Similar results for Reactor D are listed in Table 2-11. Detailed results of the metallographic examinations are presented in Appendix C of Reference 2. All the hydrogen pickup data are presented in Figure 2-5. Other hot extraction data (3, 4) confirm the hydrogen pickup fractions estimated in this program. For samples in the post-transition range, the hydrogen pickup fraction was found to be less than 16%. Thinner oxides had a larger pickup fraction than thicker oxides.

Table 2-9

CLADDING H_2 and N_2 IMPURITY CONTENT

Sample No.	Reactor	Exposure (EFPD)	Local Oxide Thickness (μm)	Concentration based on vacuum extraction (ppm)				Hydrogen Pickup Fraction (%)
				As received		After Irradiation		
				H_2	N_2	H_2	N_2	
1	PWR-A	306	10	20	38	37,42	$\leq$ 40	4.9
2	PWR-A	871	10	50	13	30	$\leq$ 40	4.4
3	PWR-A	871	40	50	13	91	$\leq$ 40	8.8
4	PWR-D	433	11	12	33	37	$\leq$ 40	6.0
5	PWR-D	687	5	12	33	13,25	$\leq$ 40	8.6
6	PWR-D	687	20	12	33	38,40	$\leq$ 40	3.3
7	BWR	701	15	10	40	4	$\leq$ 40	---

Table 2-10

METALLOGRAPHIC DATA FOR FUEL RODS FROM REACTOR A

Fuel Rod Identification	Surface Treatment	Irrdiated During Reactor Cycle	Average Rod Power (W/cm) During Cycle 1	2	3	4	5	Axial Position (cm)	Oxide Layer Thickness, μm Range	Mean	Estimated Hydrogen Concentration (ppm)	Pickup Fraction (%)
0801/62001	ground	9	240					76.8-79.3	2-6	4	40	16
								235	6-14	9	60	13
63001	ground	9	225					235	6-18	10	60	12
64002	ground	9	225					235	6-12	8	50	11
247/365/67	electropol.	4+5+8	275	300	210			130	2-8	4	35	16
								189	8-36	18	45	5
								232-235	18-28	23	34	3
299/27152	electropol.	6+7+8+9	217	206	187	98		236	20-50	32	50	3
								241	20-52	32	55	3
317/0512	ground	6+7+8	235	245	188			189	12-40	28	35	2
0609	ground	6+7+8	220	213	179			189	22-52	31	35	2
365/43002	ground	7+8	207	219				224	18-30	25	35	3
43004	ground	7+8+9	200	223	175			235	26-50	34	100	7
46001	ground	7+8	224	210				189	16-30	20	60	7
390/52001	ground	8+9	220	222				235	20-30	25	80	6
52002	ground	8	220					235	7-12	9	30	3
53001	ground	8+9	196	229				235	20-34	26	50	3
53002	ground	8	220					235	6-12	9	40	6
299-801/27295	electropol.	6+7+8+9+11	213	206	190	198		56	6-16	11	35	4
								235	32-78	53	180	8
								2446-2471	18-44		150-200	

Table 2-11

METALLOGRAPHIC DATA FOR FUEL RODS FROM REACTOR D

Fuel Rod Identification	Surface Treatment	Irradiated During Reactor Cycle	Average Rod Power (W/cm) During Cycle 1	2	3	Axial Position (cm)	Oxide Layer Thickness (μm) Range	Mean	Estimated Hydrogen Concentration (ppm)	Pickup Fraction (%)
47/12125	electropol.	1	265			345	4-8	6	<30	<7
89/8000	electropol.	1+2+3	251	193	160	375	18-32	25	60-80	5-7
96/11475	electropol.	1+2	258	234		370	12-22	16	30	2
191/3886	electropol.	1+2+3+4	192	232	180 175	375	28-48	36	100	6

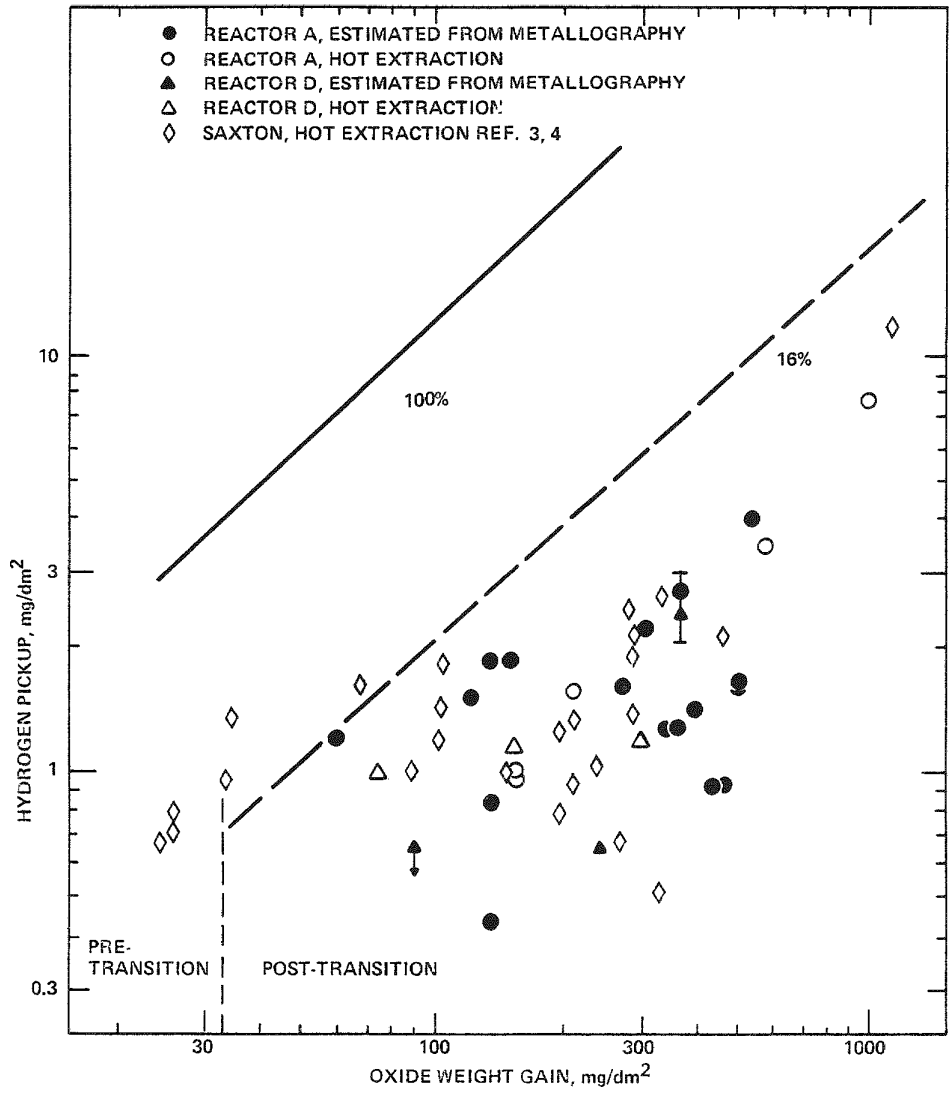

Figure 2-5. Hydrogen Pickup of Zircaloy-4 in a PWR Environment

REFERENCES

1. F. Garzarolli, D. Jorde, R. Manzel, G. W. Parry and P. G. Smerd. CE/KWU/EPRI."Review of Fuel Rod Waterside Corrosion Behavior", RP 1250-01. Task A. Combustion Engineering, Inc., June 1979 CE NPSD-79, August 1981, EPRI NP-1472.

2. F. Garzarolli, R. Manzel, P. Suchy and J. R. Politano. C-E/KWU/EPRI. "Recent PWR Waterside Corrosion Data Acquisition and Review of Clad Surface Calculation" RP 1250-01. Combustion Engineering, Inc., June 1981, CE NPSD-140.

3. W. R. Smalley. "Saxton Core II, Fuel Performance Evaluation, Part I: Materials". Westinghouse Electric Corporation, September 1971, WCAP-3385-56, Part I.

4. W. R. Smalley. "Evaluation of Saxton Core III, Fuel Materials Performance", July 1974. WCAP-3385-57.

Section 3

OXIDE FILM THICKNESS MEASUREMENTS

This section describes the nondestructive and destructive techniques used to measure the oxide layer thickness and presents the generated data. Some of the general trends in the data are then discussed, including the effects of burnup and rod power history and the influence of tubing lot-to-lot variability on in-reactor corrosion behavior.

NON-DESTRUCTIVE EXAMINATION (NDE) TECHNIQUES

Background

Traditionally, Zircaloy corrosion oxide film data have been obtained by destructive examination of selected fuel rods in a hot cell. This involves the careful preparation of metallographic sections from which zirconium oxide thickness measurements can be obtained. This technique is costly, time consuming, and limits the number of data points which can be obtained. It also precludes the ability to track the progress of clad oxidation with increasing exposure on individual fuel rods during successive refueling outages.

An eddy-current probe was developed by Kraftwerk Union (KWU) (1, 2) to non-destructively measure ZrO_2 corrosion films which have formed on irradiated fuel rods. This device has been used successfully to measure the oxide film thickness on both peripheral rods in assemblies and also on single rods removed from assemblies in spent fuel pools. Subsequently, similar probes have been designed and used by the other U.S. nuclear fuel vendors, e.g. General Electric (3) and Westinghouse (4).

It has been adapted for use in the U.S. by Combustion Engineering (C-E) and has been applied in recent outage fuel inspection campaigns supported by EPRI or DOE at Calvert Cliffs Unit One (CC-1), Fort Calhoun and Arkansas Nuclear One - Unit 2.

This section describes the KWU technique, the adaptation of the KWU measurement system by C-E, and some of the results obtained. The measurement system is described in detail in Reference (5).

Equipment, Design and Operation

The principle of the technique is illustrated in Figure 3-1. The eddy current coil carries a high frequency (3MHz) current which induces an eddy-current flow in the Zircaloy cladding substrate. This in turn produces an opposing electrical field which affects the impedance of the coil. The net coil impedance is affected by the proximity of the coil to the metal, and therefore the coil impedance provides an estimate of the distance of the coil from the metal substrate. The distance from the coil to the metal substrate is the sum of the thickness of the insulating oxide layer and the separation of the coil from the wear resistant diamond probe tip. This latter dimension can be accounted for by calibration. The technique is sensitive to minor changes in the oxide layer thickness and the response is essentially linear over the oxide thickness range of 0 to 400 μm.

The mechanical positioning and translation devices were designed to position the test coil normal to the fuel rod while translating the probe along the length of the rod after it has been removed from its fuel assembly, or while it is located on the periphery of the fuel bundle. A high degree of precision is required in order to maintain orthogonality.

A type T3-SP model* sensing coil was used with a 1.5mm diameter, 0.52 mm thick diamond tip attached by an epoxy cement. The transducer is mounted in a spring-loaded housing that has 2 degrees of freedom. In addition, the probe is spring-loaded within the housing. This measurement head is shown in Figure 3-2. A type EW8d3T3* Permascope provided an analog meter display. In order to minimize the electronic equipment sensitivity to temperature, the Permascope cabinet temperature may be maintained at a temperature of 140°F using blanket heaters.

The output can be recorded by a strip chart recorder or by a magnetic tape recorder. In the latter form the data are amenable to automated data reduction by computer.

* Supplied by Helmut Fischer GMBH & Co
Industriestr. 21, D-7032 Sindelfingen 6
W. Germany

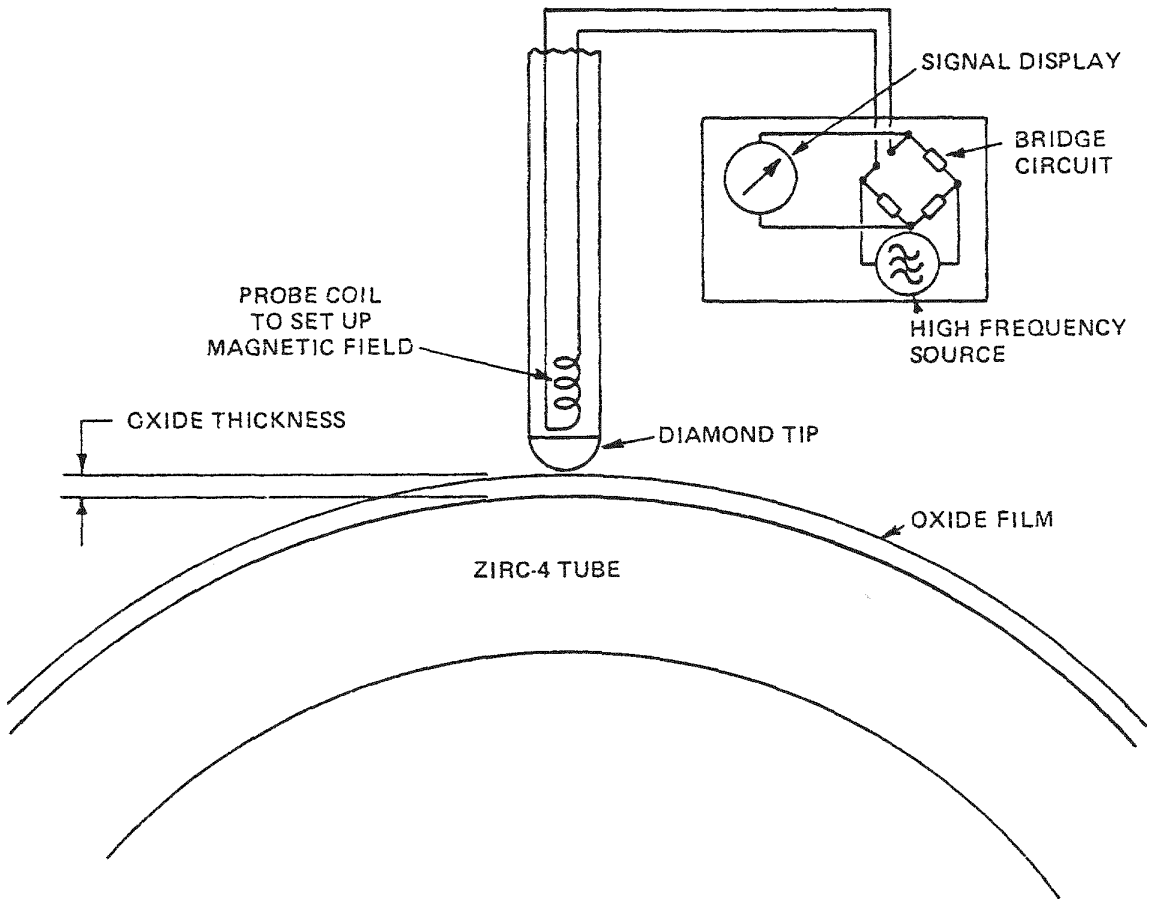

Figure 3-1. Schematic of the Principle of an ECT Oxide Thickness Probe (Proximity Probe)

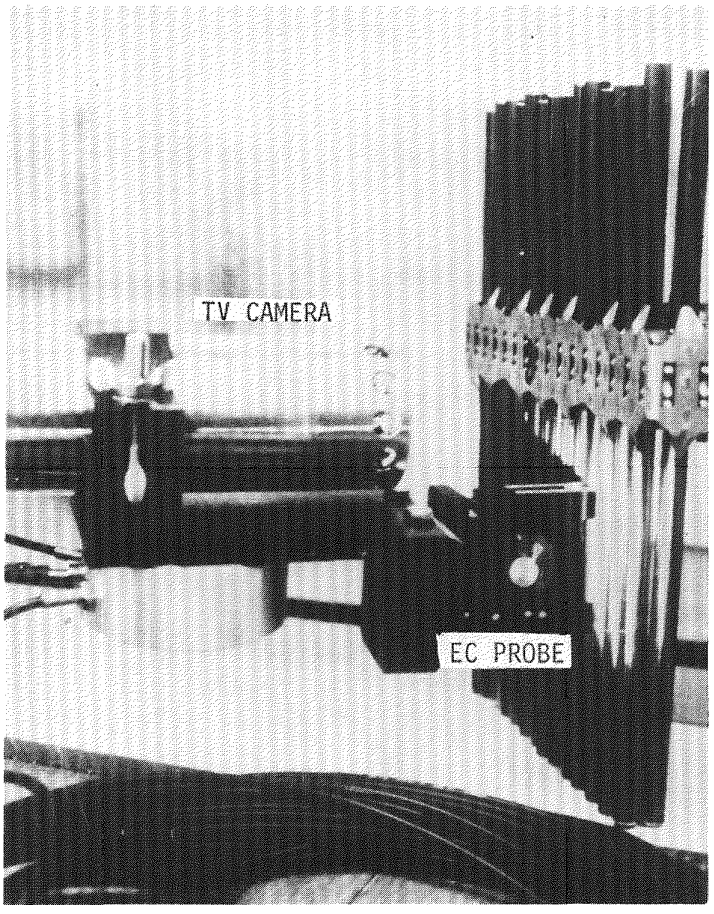

Figure 3-2. Oxide Layer Thickness Measuring Device Shown Attached to the TV Camera

The system is first calibrated in air using a Mylar tape of known thickness which is wrapped around an as-received Zircaloy tube. The final calibration is made underwater in the reactor pool using oxidized Zircaloy tubes with known oxide film thickness. The equipment reproducibility is $\pm$ 2 μm.

KWU and C-E have successfully employed the NDE equipment in many reactor spent fuel pools and in confirmatory measurements in the hot cells (1, 2, 5, 6). Schematic diagrams showing the system (Figures 3-3, 3-4 and 3-5) illustrate the techniques used to measure the oxide layer thickness of fuel rods located in peripheral positions in the fuel assembly and of individual rods after they have been removed from the fuel assembly. A detailed description of the equipment may be found in Reference (5). Three types of traces were made: spiral and linear scans along the length of the entire rod were made on single rods and linear scans between grid positions were made on peripheral rods in the fuel assembly. The types of measurements are illustrated in Figure 3-6.

Typical Results

A typical linear trace for one azimuthal orientation is shown in Figure 3.7 which was directly plotted by computer from the magnetic data tape. It can be seen that the oxide layer thickness increases with axial position and is a maximum between the fifth and seventh grids from the bottom of the rod. Within the grid positions, the oxide layer is thinner. This thickness distribution is characteristic of PWR fuel rods.

The fuel rods contain thin, loosely adherent crud deposits. In some cases the first scan was repeated and compared with the initial scan for reproducibility to ensure that the loose crud was not resulting in a measurement bias. Some rods were also cleaned in the single rod cleaning station using resilient brushes and remeasured. The data indicate that reproducible measurements were obtained even in the presence of loose crud since the diamond tip acts as an effective crud scraper.

DESTRUCTIVE EXAMINATION TECHNIQUES

In a few cases the oxide layer thickness was also determined by destructively examining some fuel rods after shipping them to a hot cell. Typically, a 5.0 cm long section of a fuel rod was cut and impregnated with epoxy to minimize any damage to the oxide. Standard mounting and polishing techniques were then used to prepare the sample. These samples were then examined using optical microscopy. Cross-

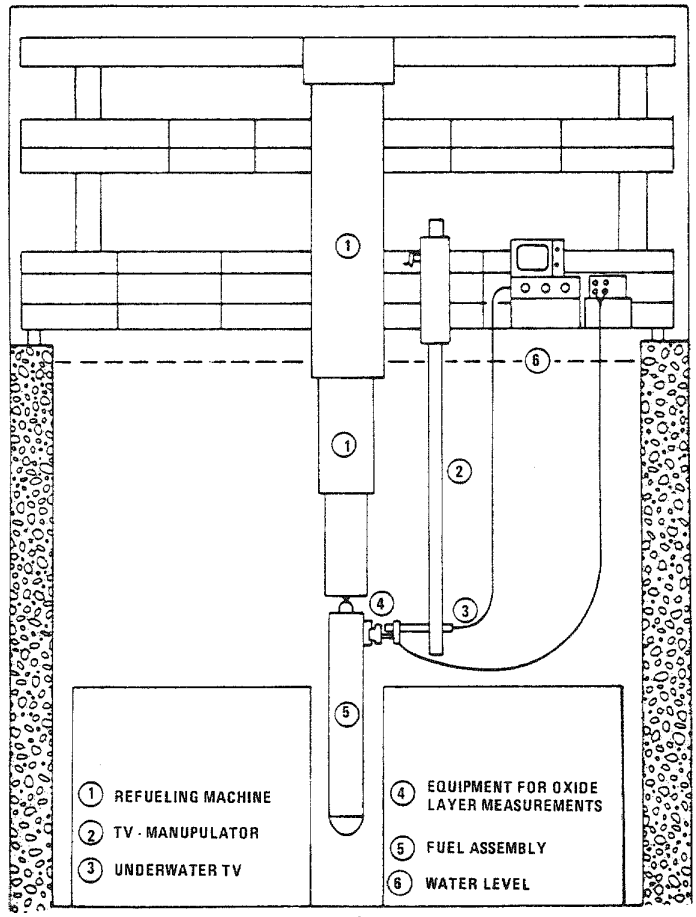

Figure 3-3. Schematic Showing the Oxide Layer Thickness Measuring Device in Operation in the Spent Fuel Pool Characterizing Peripheral Fuel Rods of a Fuel Assembly

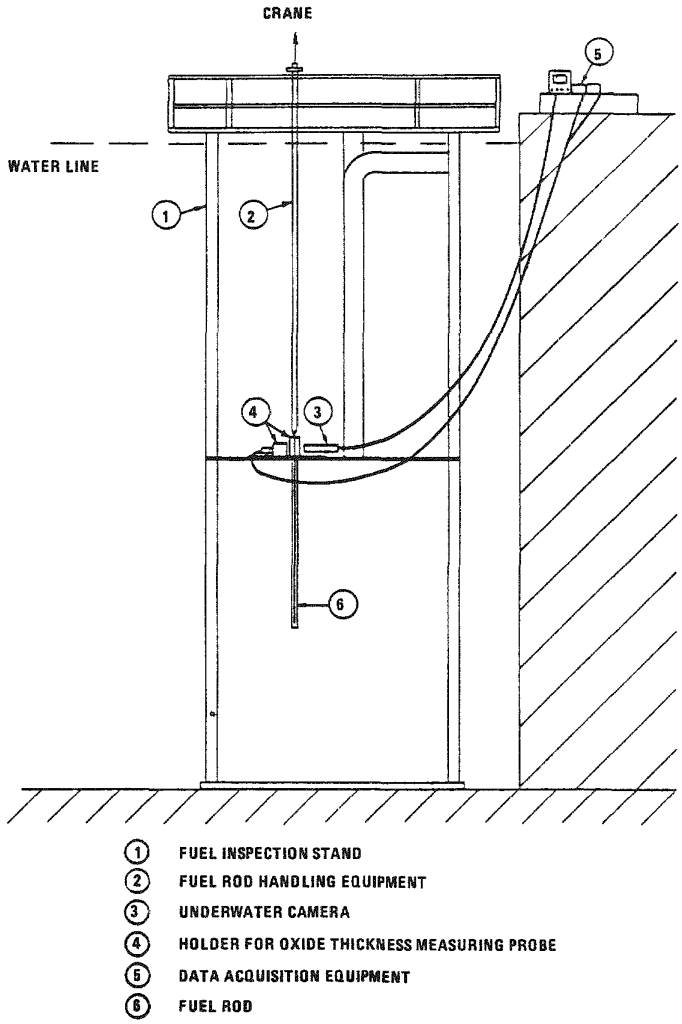

Figure 3-4. Single Rod Oxide Film Thickness Measurement in the Spent Fuel Pool

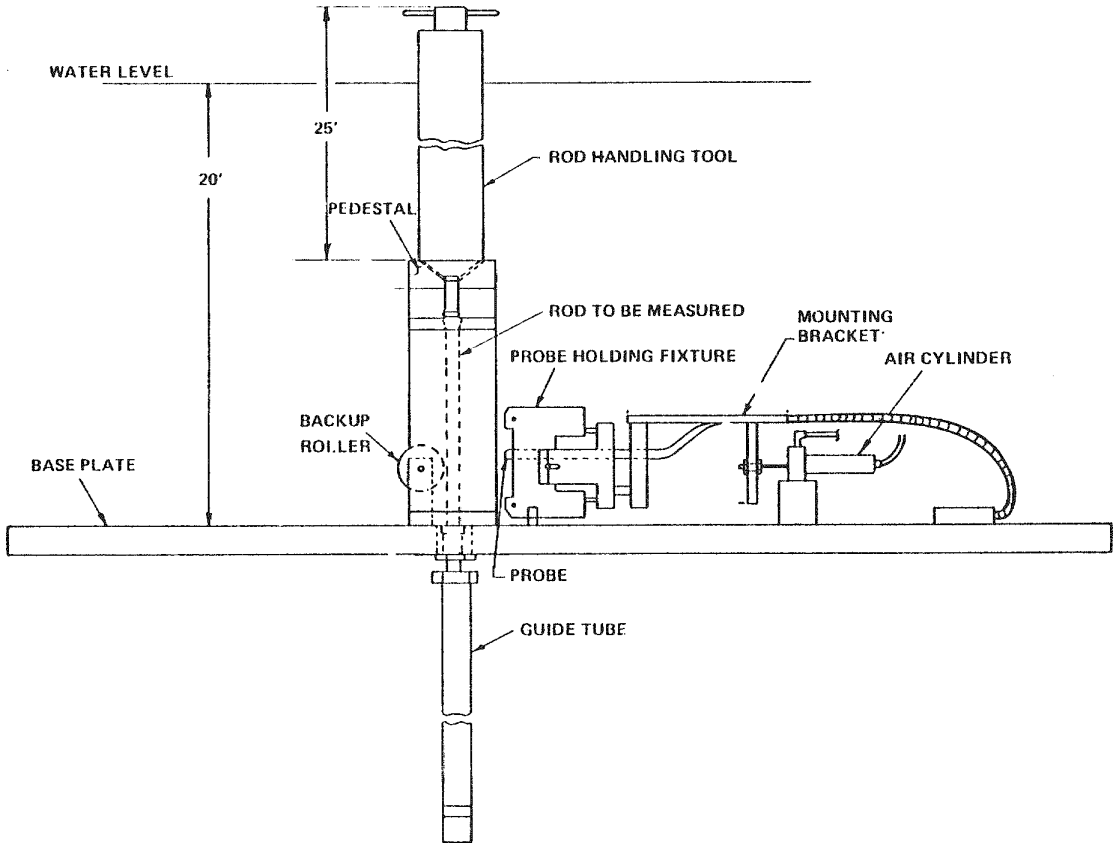

Figure 3-5. Single Rod Oxide Film Thickness Measurement System (Probe Shown in Retracted Position)

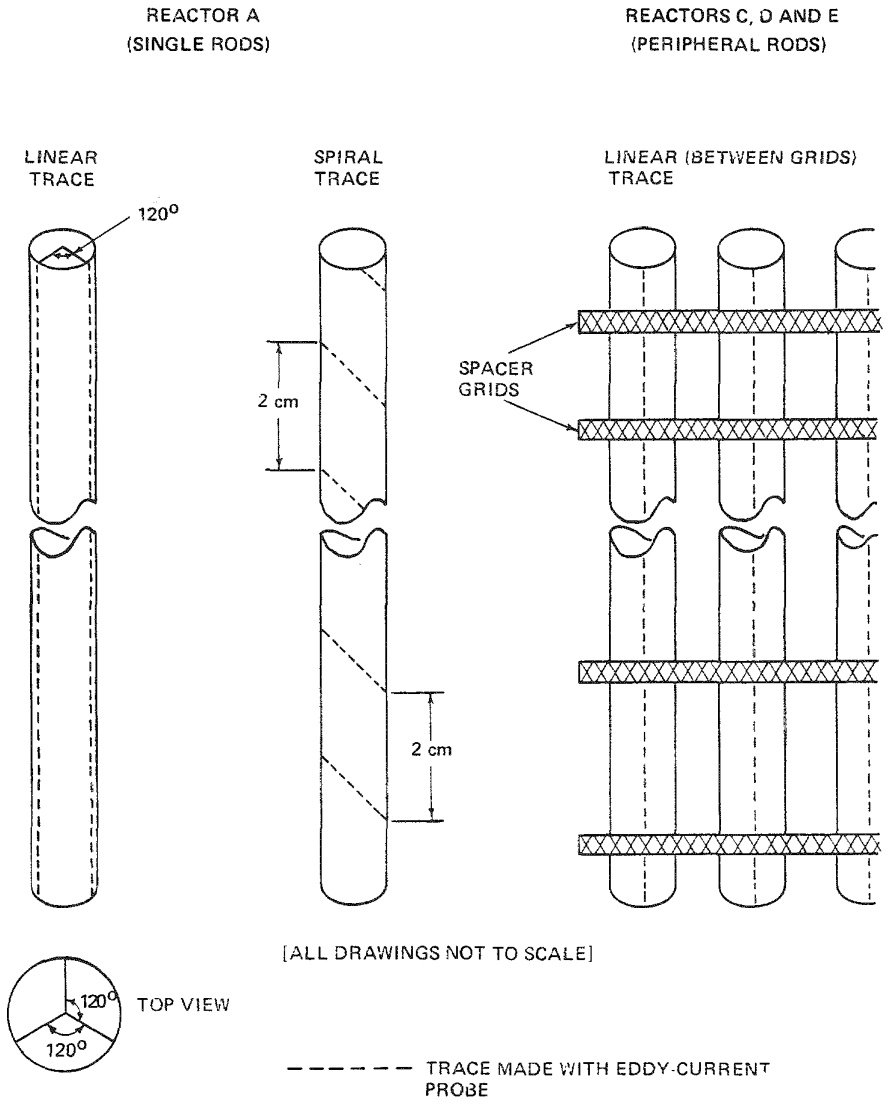

Figure 3-6. Schematic Illustration of Poolside Eddy Current Examination Types

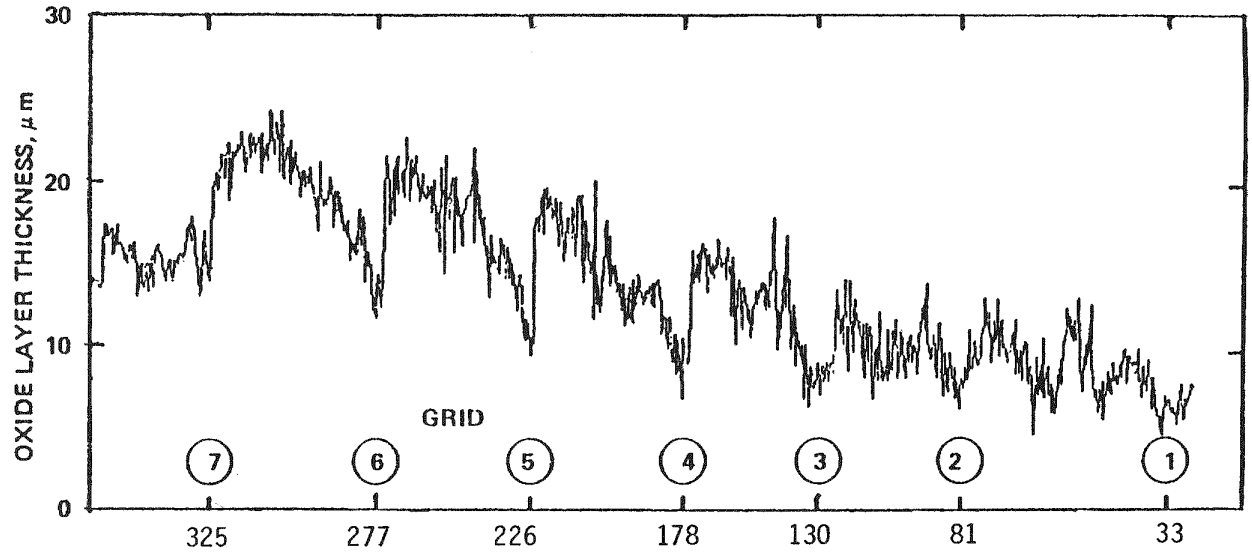

Figure 3-7. Oxide Layer Thickness Trace for a Fuel Rod After 3 Cycles of Irradiation

sections of the fuel rod were photographed at 10X while 'typical' oxide layer photographs were taken at 500X. An example of the irradiated cladding evaluated in this manner is given in Figure 3-8. The other measurements are reported in Appendix C of Reference (4).

COMPARISON OF NON-DESTRUCTIVE EXAMINATION (NDE) AND DESTRUCTIVE EXAMINATION TECHNIQUES

Metallographic examinations were conducted on sections of fuel rod which had been previously characterized using the NDE eddy current equipment in order to confirm the accuracy of the eddy current technique for oxide thickness measurements. Measurements were made on fuel rods from this program and on fuel from Calvert Cliffs Unit I as part of the another EPRI sponsored program (RP586-1). A comparison of the results using both methods is presented in Figure 3-9. The comparison shows that most of the data are within $\pm$ 5 μm of the metallographic thickness data. This excellent agreement with the metallographic measurements provides an independent check of the accuracy of the eddy current measuring system.

NON-DESTRUCTIVE (NDE) MEASUREMENTS

Experimental Program

The NDE experimental program is outlined in Table 3-1. This presents the number of fuel rod measurements that were conducted, the time at power in EFPD, the associated burnup and power range and the reactor of interest. The results are presented in volume II of this report. The hot cell measurements are summarized in Tables 2-10 and 2-11.

Discussion of Data

The oxide layer thickness data from Reactors A, C, D and E reported in Reference (1), together with more recent data, are plotted in Figures 3-10 to 3-18.

Figure 3-10 shows the increase in mean oxide layer thickness (measured over a length of 5 cm) at the peak rod temperature position for the six PWR's studied. The highest corrosion is observed in Reactor F, the plant with the highest inlet temperature (293°C). The lowest corrosion was measured in Reactor C, which has relatively short fuel rods and a relatively high coolant flow rate. The data points in Figure 3-10 represent the average response of several fuel rods.

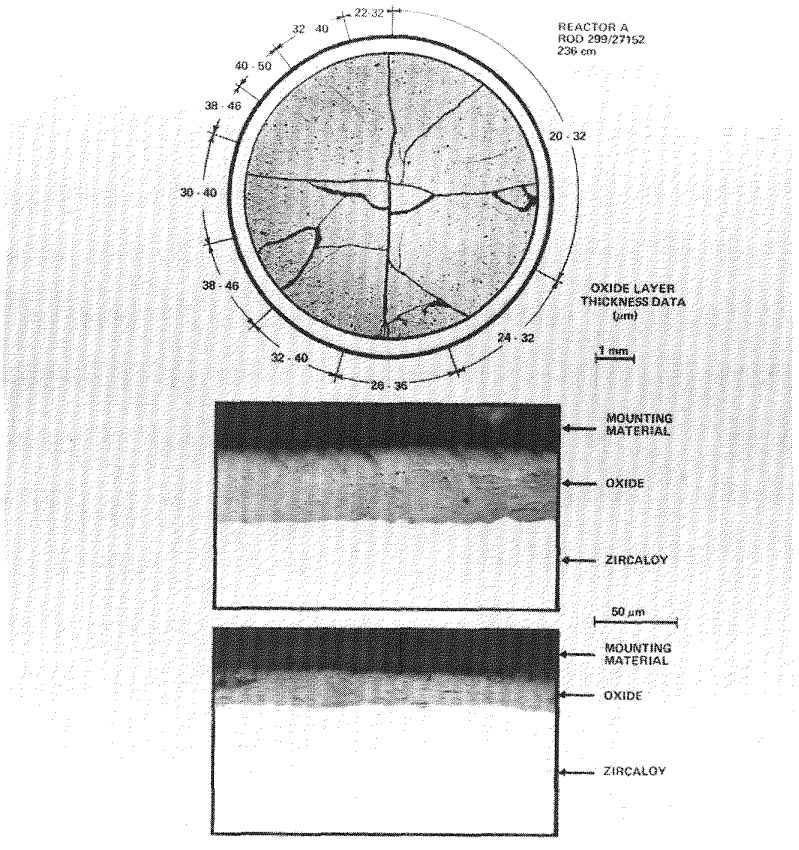

Figure 3-8. Metallographic Characterization of the Outer Oxide Layer of Rod 299/27152, Reactor A

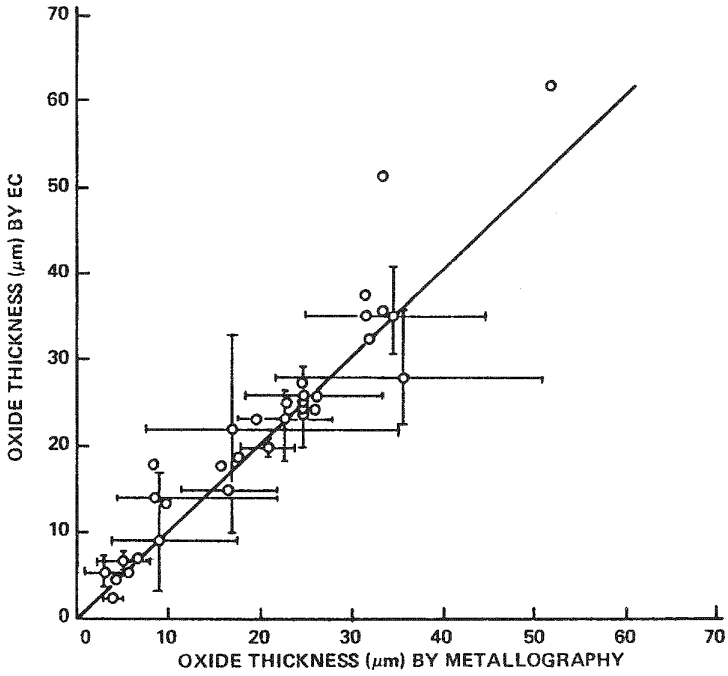

Figure 3-9. Comparison of Oxide Film Measurements Using Both NDE and Metallography

Table 3-1

SUMMARY OF NDE MEASUREMENTS

Reactor	Number of Rods Measured	Maximum Exposure (EFPD)	Power Range (W/cm)	Burnup Range GWd/t
PWR-A	121	1446	42-405	11.2 - 45
PWR-C	172	930	70-270	3.3 - 35.2
PWR-D	123	1280	55-260	9.2 - 43.5
PWR-E	238	1057	58-338	8.3 - 40.5
PWR-F	71	593	90-300	13.1 - 26.

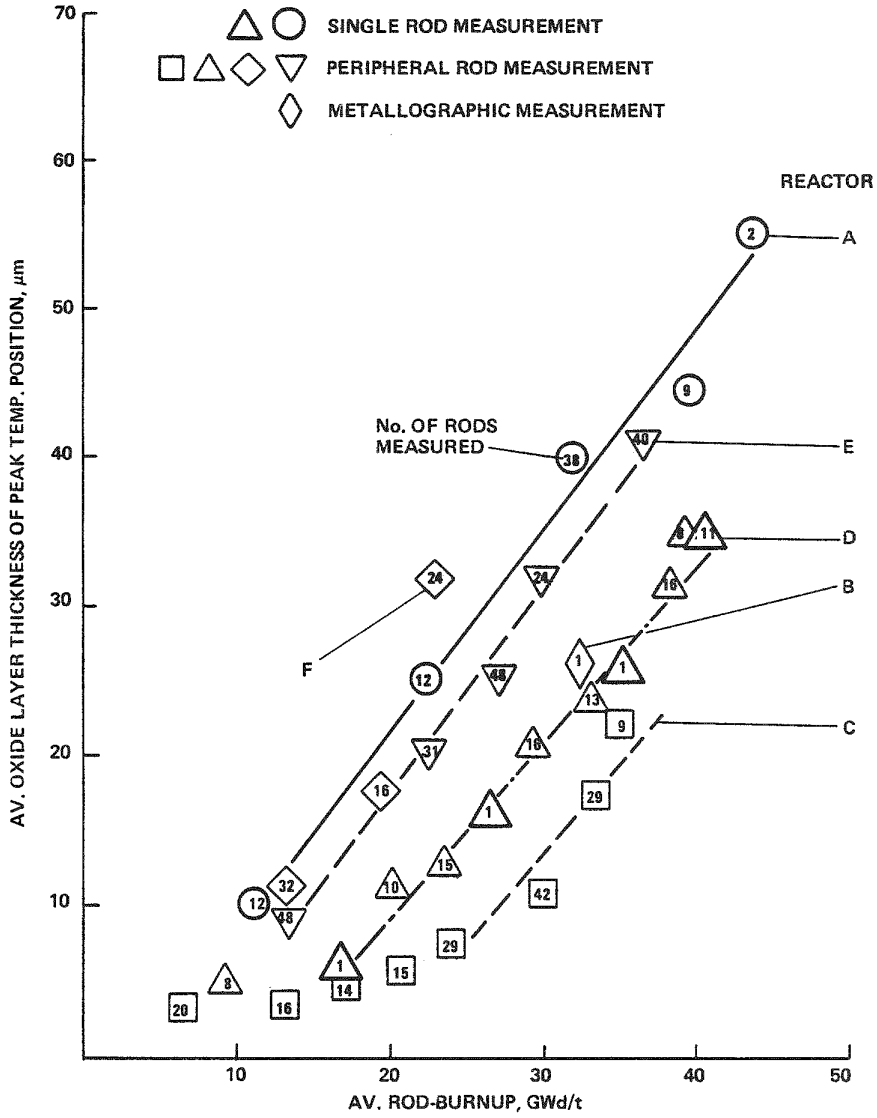

Figure 3-10. Burnup Dependence of Corrosion

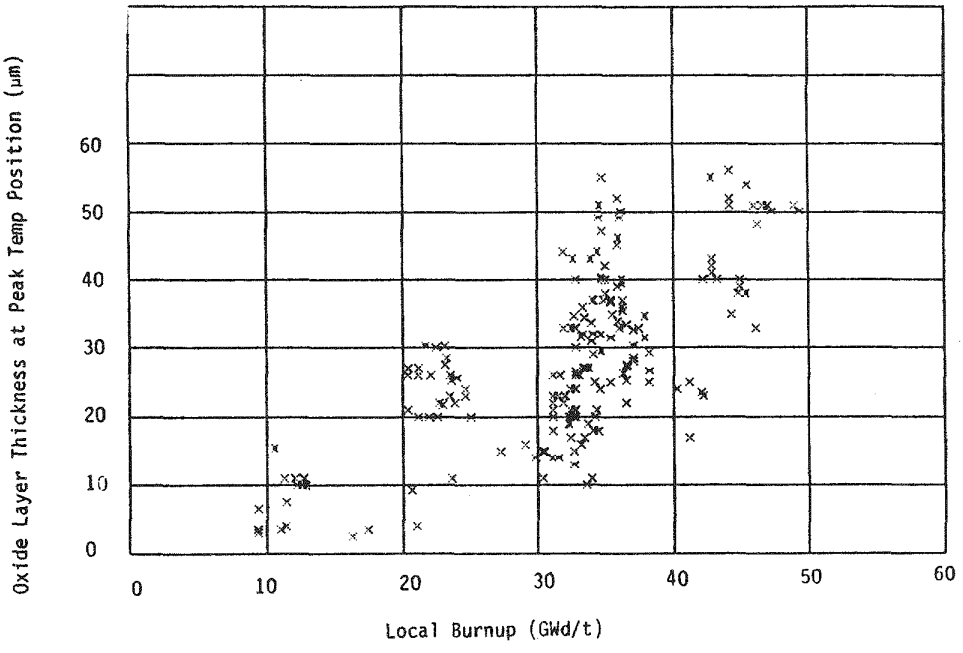

Figure 3-11. Oxide Layer Thickness as a Function of Burnup for Reactor A

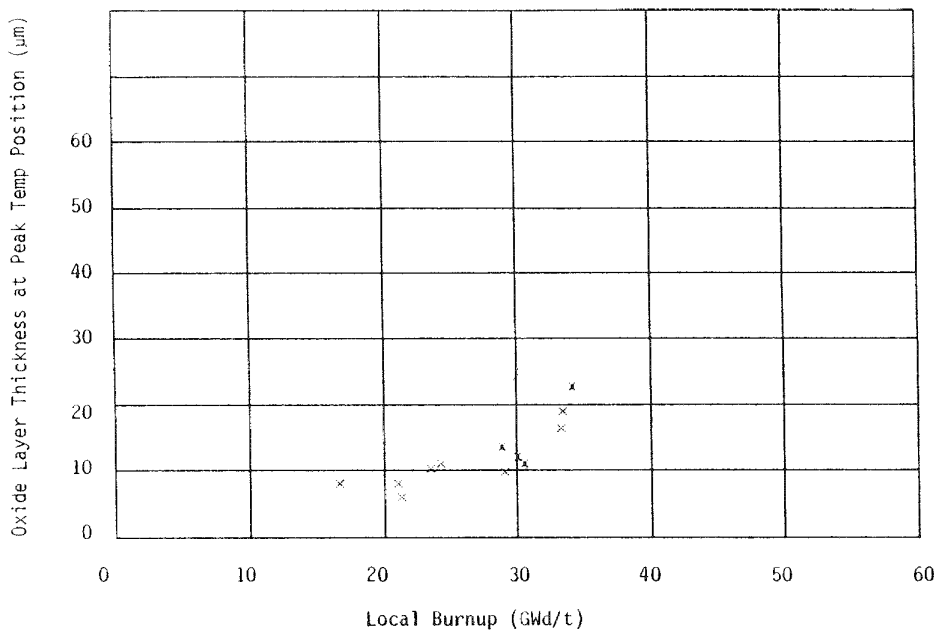

Figure 3-12. Oxide Layer Thickness as a Function of Burnup for Reactor C

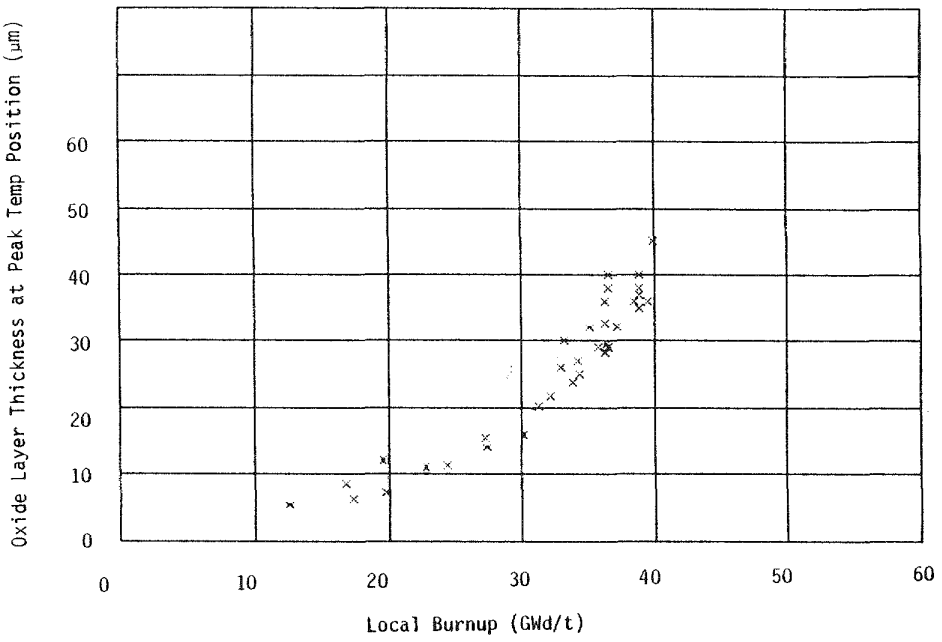

Figure 3-13. Oxide Layer Thickness as a Function of Burnup for Reactor D

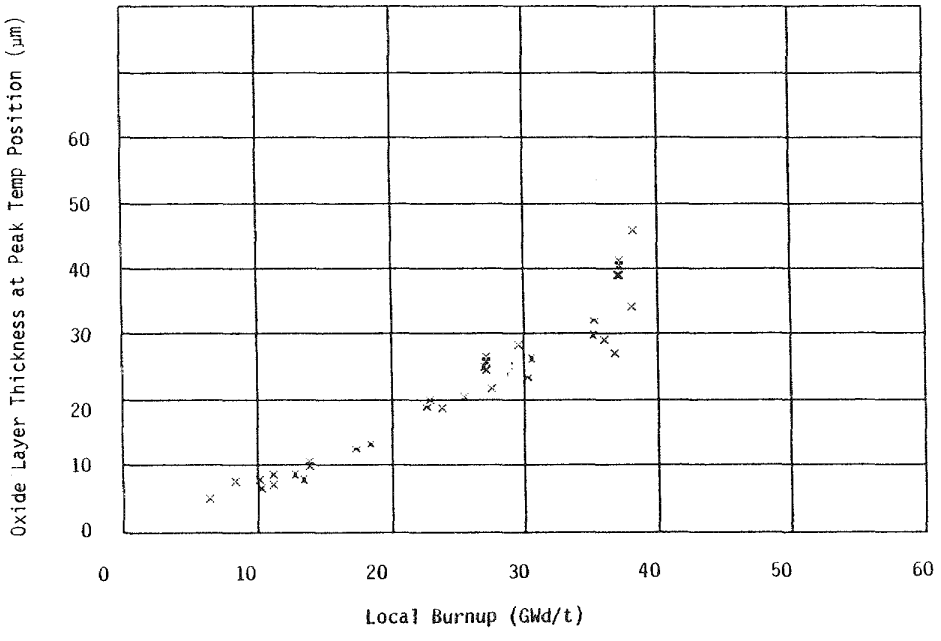

Figure 3-14. Oxide Layer Thickness as a Function of Burnup for Reactor E

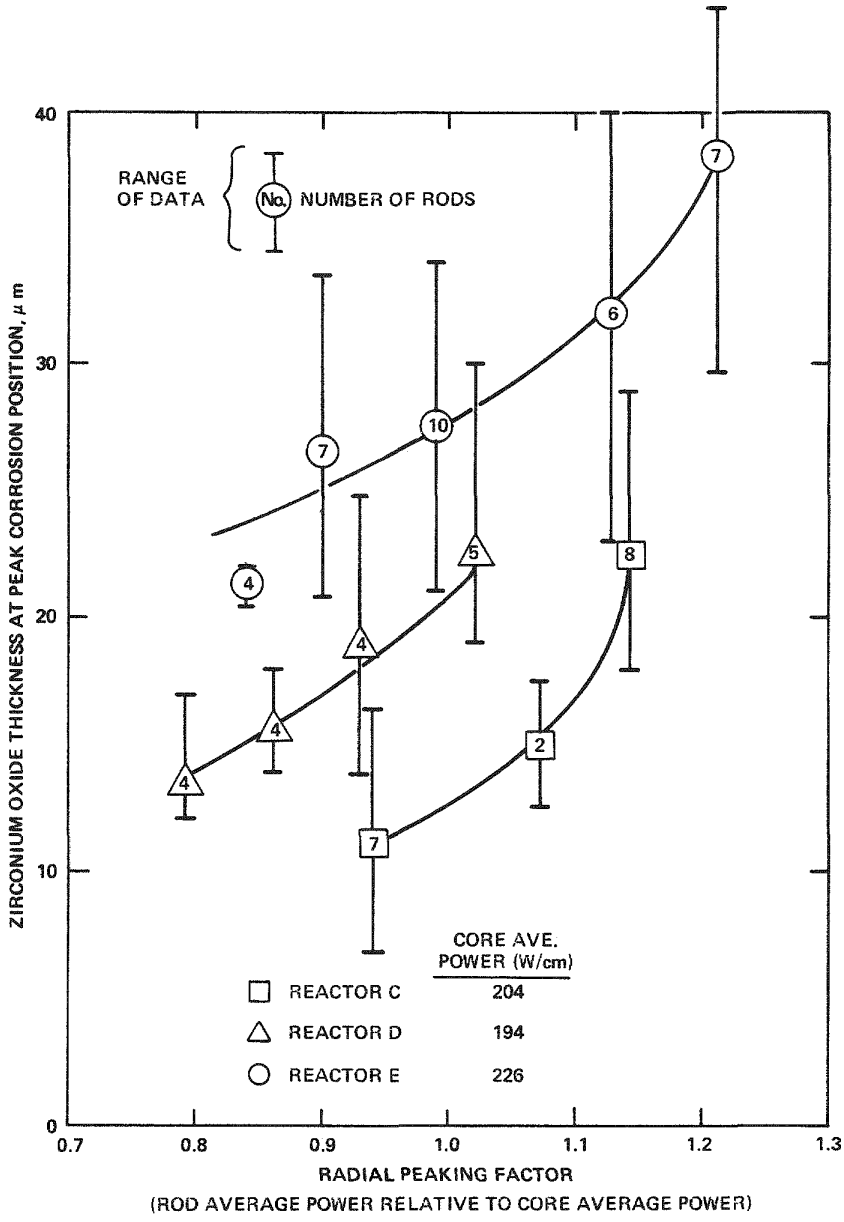

Figure 3-15. Influence of Rod Average Power on Zircaloy-4 Clad Oxide Layer Thickness at Peak Corrosion Position for 3-Cycle Rods of Reactors C, D and E

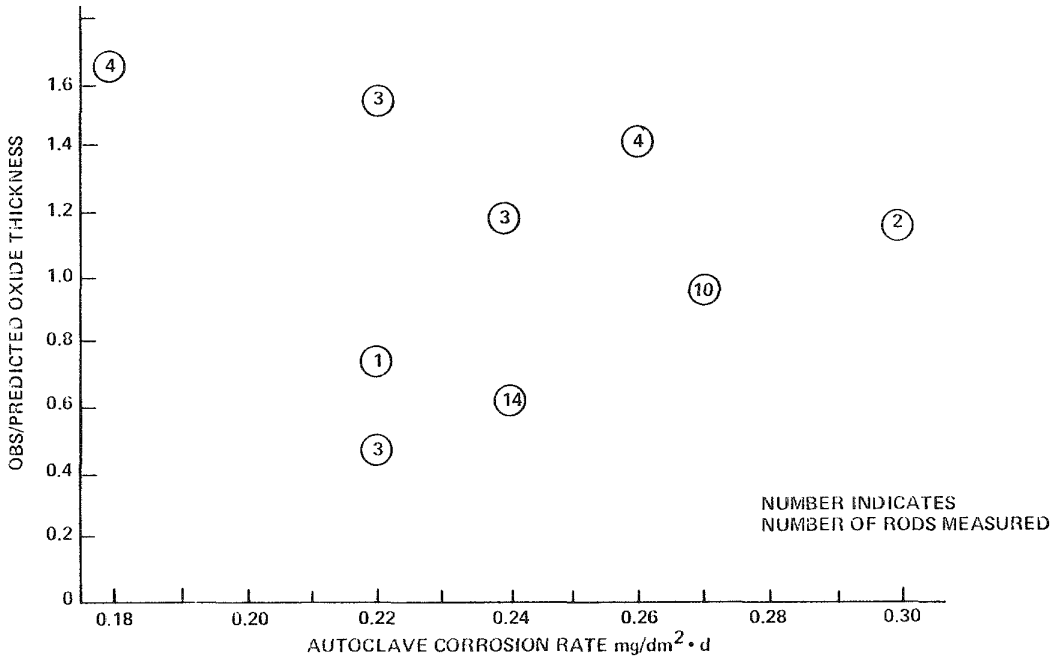

Figure 3-16. The Tubing Lot-to-Lot Dependence of In-Reactor Corrosion for Reactor A

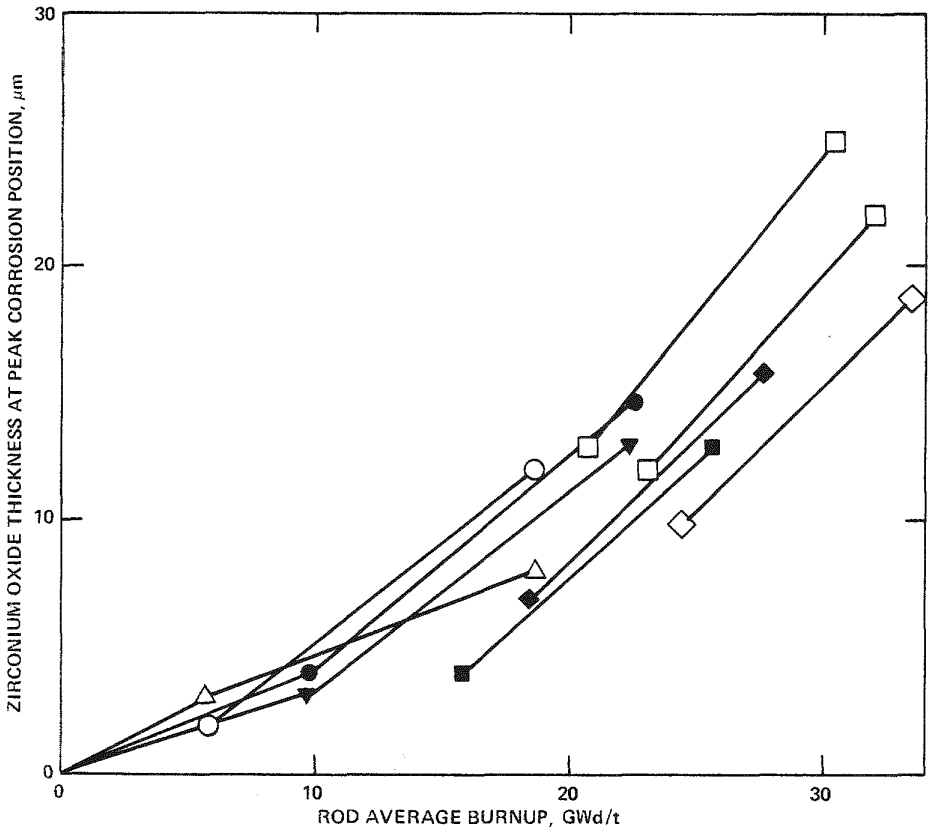

Figure 3-17. Results of Successive Zircaloy-4 Clad Oxide Layer Thickness Measurements on Fuel Rods from Reactor D

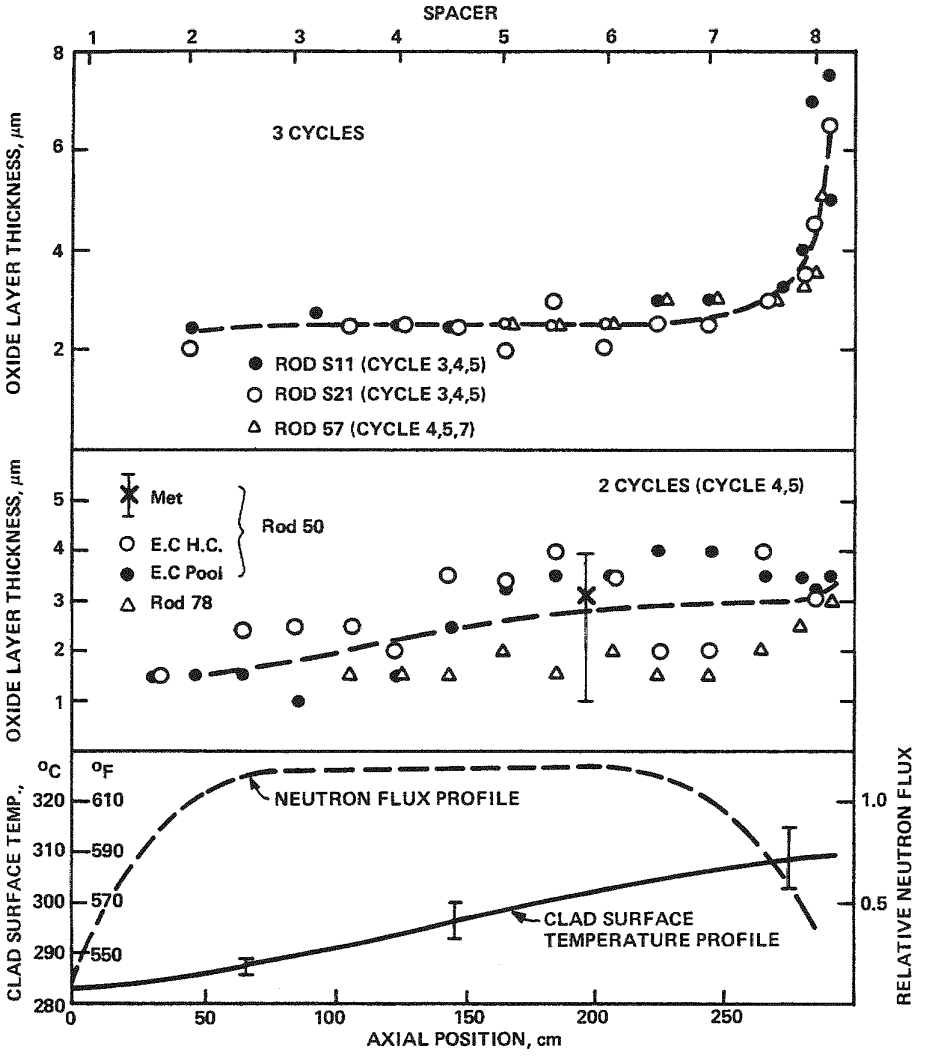

OXIDE LAYER THICKNESS OF NON-FUELED RODS FROM PWR-A

Figure 3-18. Oxide Layer Thickness Measurements of Non-Fueled Rods from PWR-A

The burnup dependence is also illustrated in Figure 3-11 where the mean oxide layer thickness at the peak rod temperature position for fuel from Reactor A is plotted as a function of local burnup. At a given burnup the variability may be quite large. There are several reasons for the observed scatter, including rod-to-rod differences in power history and variability due to the different cladding lots tested. Similar plots are given for Reactors C, D and E in Figures 3-12 to 3-14. The dependence of corrosion on rod power is illustrated in Figure 3-15 where oxide layer thickness is shown as a function of rod power relative to reactor power. The oxide thickness increases with increasing power.

Variations of the ex-reactor cladding corrosion properties within specification limits may influence corrosion in-reactor. The in-reactor corrosion performance of fuel rods fabricated from several cladding lots has been followed. The fuel rods have encountered a variety of power histories and have been irradiated in Reactors A, C and D. In order to account for these additional variables the performance has been expressed as a ratio of observed to predicted oxide layer thickness based on the corrosion model discussed in Section 7. (The constants for the model are given in Table 7-2.) That is, the corrosion performance of the fuel rods is compared to the average predicted corrosion behavior. It should be noted that the model provides a good estimate of the corrosion behavior of rods in Reactors A and D. For simplicity only the data from Reactor A have been compared with the post-transition corrosion rate determined on archive samples in water at 350°C, Figure 3-16. These measurements suggest that there is no obvious correlation between in-reactor corrosion performance and ex-reactor corrosion behavior at 350°C.

Figure 3-17 shows oxide layer thicknesses measured on fuel rods from Reactor D after various exposures. The oxide layer thicknesses were originally measured after a certain exposure, returned to the reactor for additional exposure, then removed and remeasured. This type of sequential measurement on the same rod is most useful for model development.

Measurements made on non-fueled test rods also provide information which is useful in developing a corrosion model since the uncertainties associated with the rate controlling temperature are reduced to estimating the local coolant temperature. Data from test rods irradiated for two and three cycles are given in Figure 3-18.

Conclusions

An eddy-current probe to nondestructively measure oxide layer thickness has been developed and successfully used by KWU and C-E in many outage fuel inspection campaigns. It has been shown that measurements of oxide layer thickness using this technique are within $\pm$ 5 μm of the thickness measured using destructive metallography. Oxide layer thickness increases with increasing power, burnup and time. It also appears to be sensitive to the reactor inlet temperature. In-reactor corrosion performance does not correlate with the ex-reactor corrosion behavior in water at 350°C. Measurements of oxide film thickness from more than 700 fuel rods have been completed. These data are analyzed in Section 7.

REFERENCES

1. F. Garzarolli, D. Jorde, R. Manzel, G. W. Parry and P. G. Smerd. CE/KWU/EPRI. "Review of PWR Fuel Rod Waterside Corrosion Behavior".RP 1250-01. Task A. Combustion Engineering, Inc., June 1979, CE NPSD-79, August 1980, EPRI NP-1472.

2. K. P. Francke, D. Jorde, R. Manzel, F. Rutsch and E. Vogt. "Eddy-Current Testing as a Tool for Post-irradiation Examination", BNES International Conference on Post-Irradiation Examinations, Grange-over-Sands, U.K., May 13-16, 1980.

3. J. A. Baumgartner, W. E. Baily, R. A. Proebstle and J. F. Schardt. "Extended Burnup Fuel Investigations in Commercial Reactors", American Nuclear Society Topical Meeting on LWR Extended Burnup - Fuel Performance and Utilization, April 4-8, 1982.

4. H. W. Wilson, E. Roberts, J. B. Melehan, R. S. Kaiser, J. D. Bein, H. H. Kunishi. "Fuel Performance Characteristics at Extended Burnup", American Nuclear Society Topical Meeting on LWR Extended Burnup - Fuel Performance and Utilization, April 4-8, 1982.

5. H. D. Goddard, J. P. Lareau, T. R. Slade, P. A. Van Saun and R. G. Weber. CE/KWU/EPRI, "Non-destructive Measurement of Zirconium Oxide Corrosion Films on Irradiated Zircaloy Clad Fuel Rods". RP 1250-01, Combustion Engineering, Inc., June 1981, CE NPSD-102.

6. F. Garzarolli, R. Manzel, P. Suchy and J. R. Politano. CE/KWU/EPRI. "Recent PWR Waterside Corrosion Data Acquisition and Review of Clad Surface Temperature Calculation", RP 1250-01. Combustion Engineering, Inc., June 1981, C-E NPSD-140.

Section 4

CHARACTERIZATION OF THE OXIDE FILM

INTRODUCTION

In several publications (1 to 12) the in-reactor corrosion of Zircaloy in water and steam was compared with the ex-reactor corrosion behavior and, it was concluded that corrosion is enhanced by neutron irradiation. However, the degree of enhancement was found to be markedly influenced by the corrosion environment. In high purity water, containing no additives, where oxygen and oxidizing radicals are formed due to radiolysis, the corrosion was found to be enhanced by a factor of 10 or more (1 to 7). In addition nodular corrosion was often seen.

In Pressurized Water Reactors (PWRs), where the radiolytic formation of oxygen and oxidizing radicals in the coolant is decreased by the addition of hydrogen to the coolant, the corrosion of Zircaloy was found to be less enhanced by irradiation. An increase in corrosion by a factor of 1-3 has been reported (2, 3, 5, 6, 7, 9, 10, 11). However, the visual appearance of the oxide layers and their microstructure formed either in-reactor or ex-reactor are very similar, irrespective of irradiation and heat flux conditions.

Corrosion behavior appears to be strongly dependent on the temperature at the metal-oxide interface. Under heat flux conditions, this temperature increases as the oxide layer thickens, further increasing the corrosion rate. The temperature rise across the oxide depends on its thermal conductivity. Little or no data are available on the thermal conductivity of irradiated oxide films. Because the thermal conductivity depends on the density of the film and the nature of cracking, these parameters must be determined especially for highly exposed fuel rods. It is necessary to know the value of the thermal conductivity of the oxide in order to predict corrosion, especially for rods having widely varying power histories.

This Section deals with the results of the characterization of the physical and chemical properties of the corrosion films. The implications of these observations on the proposed corrosion mechanisms and on the in-reactor corrosion behavior are discussed. All irradiated samples investigated within this program are specimens cut from standard fuel rods after various burnups.

MATERIALS AND EXPERIMENTAL TECHNIQUES

In this program both irradiated and unirradiated fuel cladding have been evaluated. The unirradiated oxide samples were formed under a variety of conditions: temperature (360°C to 650°C), environment (air, steam or water), and exposure times (up to 813 days). The irradiated cladding originated from two PWRs, (labelled A and D) as well as from one BWR, enabling the influence of coolant conditions on oxide film formation to be studied. Samples were taken from different axial positions on PWR fuel rods so that any effect due to surface temperature could be assessed. The in-reactor residence time of the fuel rods examined ranged from 300 to 1200 days; irradiated oxides up to 70 μm thick were destructively examined. An enhancement factor comparing in-reactor corrosion to an out-of-pile model was calculated according to Appendix A of reference (10).

Prior to sectioning, the fuel rods were characterized in detail, including non-destructive measurements of the oxide film thickness. The sample axial positions as well as the local oxide film thicknesses are given in Table 4-1, together with the parameters which reflect their prior irradiation history.

The techniques used to characterize the oxide layers included optical and scanning electron microscopy, x-ray diffraction, chemical analysis, secondary ion mass spectroscopy, and ion microprobe and electron microprobe analysis. Preliminary impedance, surface area and pore volume measurements were made on unirradiated samples. The impedance measurements provide a description of the character of the oxide layer and an estimate of the thickness of the dense inner layer in the case of oxides with a duplex layer structure. BET (Brunauer-Emmett-Teller) measurements give an estimate of the surface roughness, and pore volume measurements can give a measure of the size of the pores present in the oxide. Autoclave corrosion testing was also conducted on irradiated samples to evaluate the extent of any "memory" of the in-reactor exposure. These measurements were conducted in the hot cells of the Battelle Memorial Institute (BMI), in Columbus, Ohio, USA, Argonne National Laboratory (ANL) in Argonne,

Table 4-1

CHARACTERISTICS OF OXIDES FORMED IN-REACTOR

Sample No.	Reactor	Exposure Time (EFPD)	Neutron Fluence (E>1 Mev) $n/cm^2 \times 10^{21}$	Axial Position from Bottom of rod (cms)	Oxide Thickness μm	Calculated Corrosion Enhancement Factor	Postulated Environment within the Porous Oxide
1	PWR-A	306	2	220	10	3	340°C water
2	PWR-A	871	6.5	110	10	3	320°C water
3	PWR-A	871	6.5	230	40	3.5	345°C steam
9	PWR-A	586	4.5	220	15	n.d.	n.d.
10	PWR-A	903	7	220	50	n.d.	n.d.
4	PWR-D	433	3	365	10	1.5	345°C steam
5	PWR-D	687	6	150	5	2	320°C water
6	PWR-D	687	6	320	20	2.5	345°C steam
7	PWR-D	687	6	365	20	2.5	345°C steam
11	PWR-D	998	7.5	360	29	n.d.	n.d.
8	BWR	701	4	20	15 (nodular)	>10	290°C steam

n.d. - not determined

Illinois, USA, and Kraftwerk Union AG (KWU) in Karlstein, Germany. Thermal conductivity measurements were performed by the United Kingdom Atomic Energy Authority (UKAEA) at their facility in Springfields, Salwick, in the United Kingdom.

Standard optical microscopy and scanning electron microscopy (SEM) were conducted to evaluate the microstructure of the oxide layer. The samples examined included (1) transverse sections through the metal and oxide film, (2) oxide films stripped from the Zircaloy metal to examine the metal/oxide and the water/oxide interfaces, and (3) fractured oxide cross sections. In preparing samples for examination, the tube sections were first cleaned in an ultrasonic bath to remove loose crud and oxide particles. The oxide films were stripped from the Zircaloy metal by dissolving the metal in hydrofluoric acid. The oxide films were rinsed in water and alcohol, dried, and supported on glass or mesh screens during the preparation. Finally, they were gold or carbon coated. The transverse metallographic sections were examined in the as-polished condition and after cathodic vacuum etching. Optical microscopy and SEM were conducted on the samples listed in Table 1. An additional group of unirradiated archive samples from PWR-A and PWR-D fuel rods was examined by optical microscopy.

X-ray diffraction analyses were conducted using a Guinier camera with Cu-K_α radiation. The oxide samples were milled to a fine powder, and TaCl was added for calibration purposes. For some samples the relative broadening of the (111)-peak was also determined using an x-ray goniometer and a scintillation counter.

The chemical analytical techniques employed to determine the impurity levels of important elements are given in Table 4-2. Zircaloy was dissolved in an etchant and analyzed for Si, B and Li, F and Cl. The remaining oxide was dissolved in $KHSO_4$ and the Si-, B- and Li- levels were determined, while pyro-hydrolysis was used to extract the fluorine and chlorine. The H-, N- and O-gas content was extracted by vacuum fusion in a platinum crucible.

Secondary ion mass spectroscopy (SIMS) was used to obtain the relative concentration of impurities present on the surface of the oxide sample being examined. Both ion microprobe analysis (IMA) and electron microprobe analysis (EMA) were employed to determine impurity concentration profiles across the oxide layer.

Table 4-2

CHEMICAL ANALYTICAL METHODS EMPLOYED FOR THE ELEMENTAL ANALYSES OF OXIDE AND ZIRCALOY

Element	Method	Detection Limit $\mu g/cm^2$
Si	Spectral photometry	2
B	Spectral photometry	2.5
Li	Atomic Absorption	0.1
F	Ion Selective Electrode	3
Cl	Photometry	3
H	Mass Spectrometry	30
N	Mass Spectrometry	30
O	Mass Spectrometry	30

AC impedance measurements on oxidized samples immersed in a one molar H_2SO_4 electrolyte provide information on the structure of the oxide. The electrolyte permeates the pores and cracks, partially short circuiting the insulating oxide film. These impedance measurements provide an estimate of the extent of permeation. Tubular or disc shaped samples, a platinum electrode and a mercury sulfate reference electrode were immersed in the electrolyte. A Wanking potentiostat Type Bank 75L in series with a frequency analyzer, Type Solartron 1170 were used. The zero current potential was first determined and then held constant using the potentiostat. An A-C voltage of $\pm$ 50 μv was superimposed and the frequency response measured using the frequency analyzer. Impregnation was effected using a vacuum impregnation technique. The equivalent electrical circuit used in the evaluation is given in Figure 4-1. The values of the equivalent resistances and capacitances were calculated using a computer optimization routine which produced a best fit to the measured data. The thickness of the dense inner layer was then calculated from the capacity of unoxidized Zircaloy and using a dielectric constant of 20 for ZrO_2. A detailed description of the technique may be found in reference 13.

Adsorption and capillary condensation of liquids such as liquid nitrogen provide a useful technique to evaluate the distribution of pores in the size range 2-4 μm. Some preliminary measurements were conducted on unirradiated samples. The technique used was similar to that reported in (13, 14). A microbalance (Gast System) was used with a sensitivity of $\pm$ 0.1 μg. The gas pressure was controlled using high purity nitrogen gas. The samples were evacuated to $<10^{-5}$ mbar and then heated to 300°C before making the BET measurements.

The post-irradiation autoclave tests were conducted at several temperatures on irradiated tubing in a 1 liter static autoclave with deionized water containing 600 to 1,000 ppm boron, 1.3 ppm lithium and 2 to 3 ppm hydrogen. The corrosion tests were initiated at 280°C and samples were removed and weighed after 3, 10, 30, 50, 70, 90 and 110 days of testing. The temperature was then increased incrementally to 300, 325, and 350°C and then decreased to 300°C for a total corrosion test period of 240 days. The tubular samples used were about 50 mm long. Only the corrosion behavior of the outer surface of the irradiated cladding was of interest. Rather than plugging the tubes to prevent corrosion of the inner surface during the autoclave testing, the irradiated samples were prepared by removing fuel and refinishing the tubing inner surface by mechanically abrading and pickling. Unirradiated control samples given the

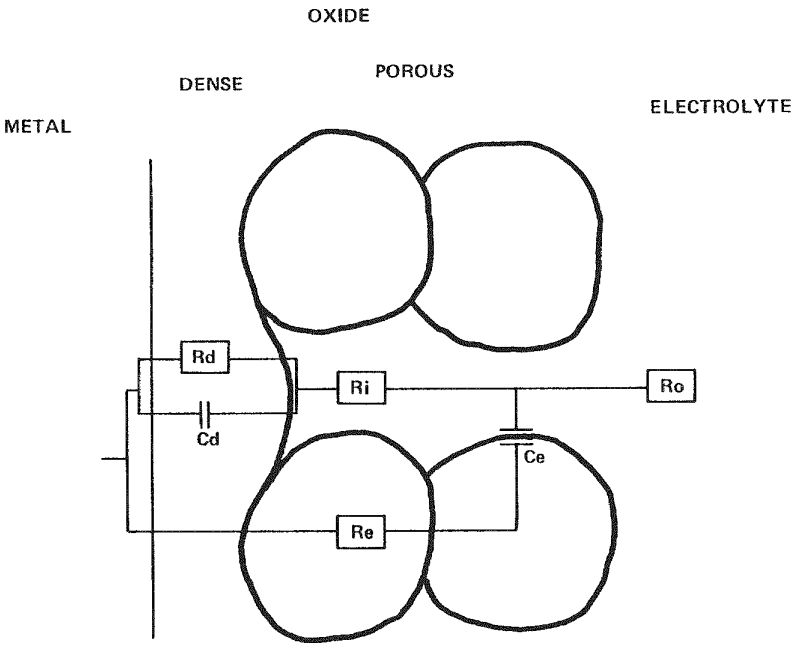

Figure 4-1. Equivalent Electrical Circuit for an Oxide with a Dense and Porous Sublayer Used in Analysis of Impedance Data

same surface treatment as the irradiated sample were also tested and these data used to correct the weight gains of the irradiated samples for the corrosion of the tubing inner surface.

Oxide density measurements were made in dibutyl phthalate using conventional pycnometry. In addition, the oxide film density was measured by first determining the layer thickness using metallography and then weighing the residual oxide film following dissolution of the metal substrate.

The thermal conductivity of the oxide films was determined from diffusivity measurements, using the oxide layer density and its specific heat. The specific heats of unirradiated and irradiated oxides were measured using differential scanning calorimetry (15) within the temperature range +50°C to +725°C. The oxide flakes were crushed to a fine powder and approximately 50 mg were encapsulated in a gold pan for the measurement. The laser flash or heat pulse technique (16) was employed to measure the diffusivity of the half-tube sections of Zircaloy-4 and oxidized Zircaloy-4 in the temperature range 20 - 550°C. Relatively large clam-shelled sections of tubing were tested to avoid damaging the oxide layer during sample preparation. The heat pulse was supplied by a ruby laser and was applied to the oxide face of the tube half shell samples; the temperature transient was monitored on the rear (metal) side by a lead sulfide detector. The measurements were performed in a vacuum furnace at temperatures of up to 650°C. For one sample the measurements were repeated in an argon purge gas at 1 bar; the thermal diffusivity was unaffected. The oxide layer thicknesses ranged from 15 to 50 μm. The thickness of the layers was determined metallographically after testing at the location of the measurement.

RESULTS

The results of the test program to evaluate the physical and chemical characteristics of the oxide layer are summarized in this section. The detailed results can be found in references (17, 18 and 19).

Microstructure of the Oxide Film

A careful examination of irradiated and unirradiated mounted and polished corrosion samples, using both optical microscopy and SEM, revealed a rather

uniform and dense oxide film, with circumferentially oriented microcracks. Cathodic vacuum etching enhanced the resolution of the oxide microstructure. Fig. 4-2 shows these features in a 50 μm thick oxide film formed in-reactor. Work by Cox (20) and Bryner (21) suggests that the cracks may have been produced by the sample preparation method. This crack pattern also was observed on fractured samples examined in the SEM (Table 4-3).

The average intercrack spacing was rather uniform (about 2 μm) but appeared to be greater for the thicker oxide layer samples. Furthermore, the intercrack spacing appears to decrease towards the metal/oxide-interface. The cracks in the oxide were predominantly circumferential in nature. This provides some support for corrosion models which involve oxide cracking as part of the corrosion process. One model proposed by Dawson et al. (14) requires that circumferential and radial cracks form during corrosion. However, this model is not completely confirmed since radial cracks were only rarely observed and there was not a strong difference between the crack pattern in the last 2 μm formed and in the remainder of the oxide.

The SEM observations of the microstructure of oxide film samples are shown in Figure. 4-3 to 4-7 and summarized in Table 4-3. The substructure of the oxide consists of spherical clusters of "cauliflower" like granules (Figure. 4-3) of size 0.15-0.3 μm. The fine granules within the cluster range in size from 0.04-0.1 μm. The features of the substructure do not always develop to the same extent. Only in the case of oxides grown under BWR conditions have columnar-type clusters occasionally been observed (Figure. 4-4). The autoclaved samples had an oxide microstructure similar to those of irradiated PWR oxides.

The outer thick post-transition oxide layer is generally assumed to be non-protective; the corrosion rate is mainly controlled by the characteristics of the innermost part of the oxide close to the metal substrate. Therefore, most attention was given to characterizing the oxide/metal interface.

In order to minimize any influence of the metal stripping operation on the oxide microstructure, two samples with oxide still on the metal substrate were cooled in liquid nitrogen and fractured. Figure. 4-5 shows an oxide/metal interface area. Even at high magnification the crystalline oxide extends almost to the metal surface. It was difficult to resolve the crystalline structure

Table 4-3

SEM EXAMINATION OF OXIDE LAYER

Sample Identification No.	Oxide/Metal-Interface Characteristic	Extent of Low Resolution Layer (μm)	Size and Nature of Granule Cluster (μm)	Size of Granules (μm)	Average Intercrack Spacing (μm)
ex-reactor water[1]	diffuse	0.5	0.5 - 1.0 (spherical)	0.04-0.08	1.5
(autoclave) steam[2]	crystalline	0	0.06 - 0.12	not resolved	3.0
PWR-A 1	mixed[3]	0-0.5			1.6
PWR-A 2	diffuse	0.5	0.08 - 0.7	0.06-0.15	n.d.*
PWR-A 3	mixed[3]	0-0.5	(spherical)		3.0
PWR-D 4	diffuse	1.5			1.8
PWR-D 5	diffuse	0.5	0.08 - 0.3	not resolved	n.d.
PWR-D 6	diffuse	0.5-1.0	(spherical)		2.2
BWR 8	mixed[3]	0-1.0	0.1-0.25 (spherical) 0.2x1.0 (columnar)	not resolved	3.4

[1] 343°C/813 d

[2] 470°C/44d

[3] predominantly crystalline with some diffuse

*n.d. = not determined

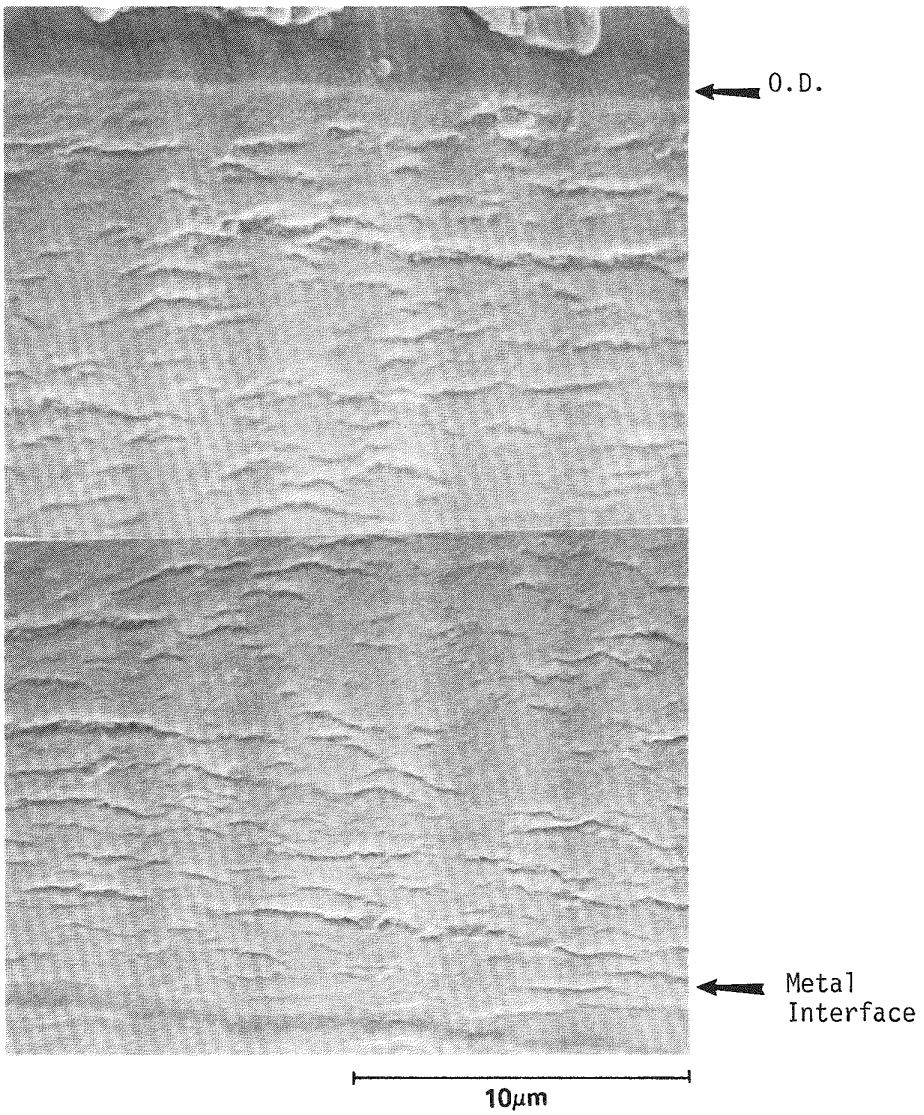

Figure 4-2. SEM Micrograph of Cathodic Vacuum Etched Oxide Sample 3 Formed in PWR-A

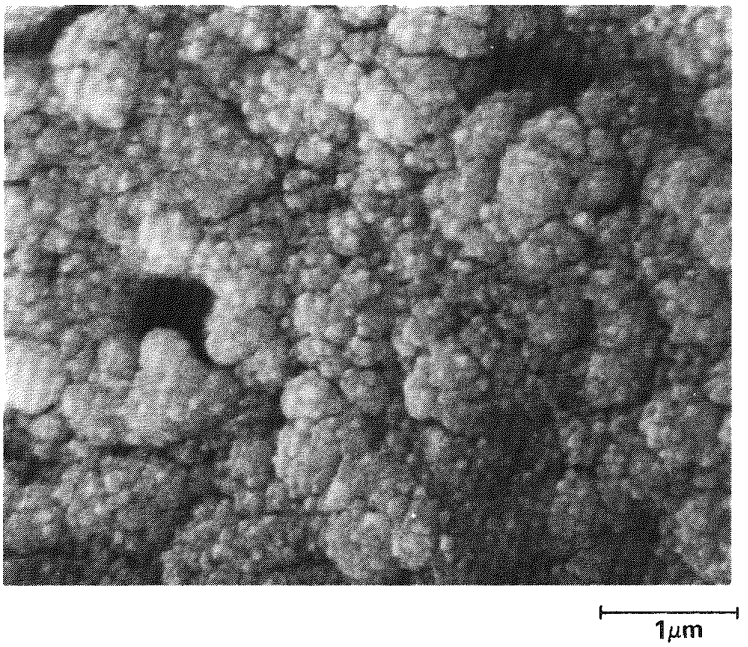

Figure 4-3. Spherical Granule Cluster Structure of an Oxide Taken from the High Temperature Region of a Fuel Rod from PWR-A. The Metal was Removed and the Oxide Fractured (Sample 3).

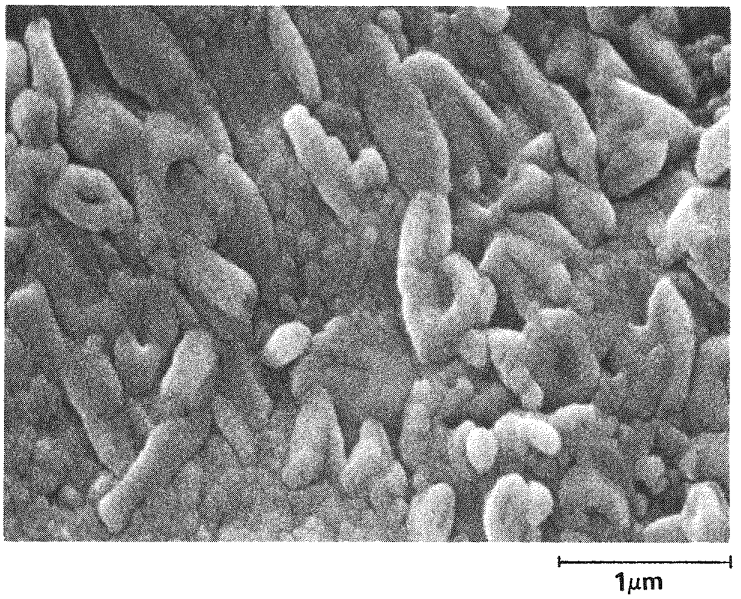

Figure 4-4. Columnar and Spherical Granule Cluster Structure of an Oxide Taken from a Fuel Rod from a BWR. The Metal was Removed and the Oxide Fractured (Sample 8).

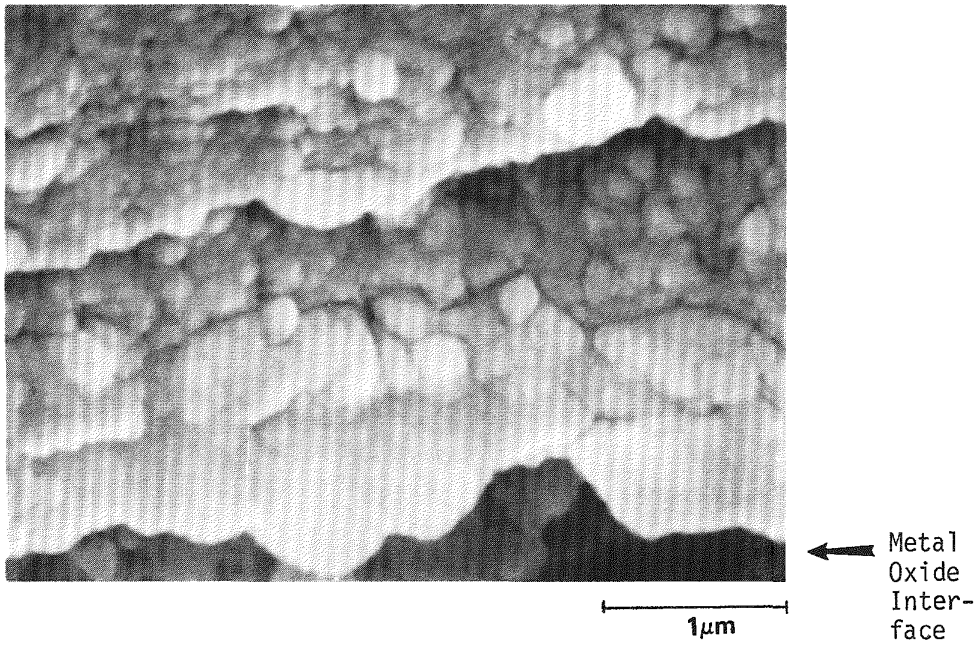

Figure 4-5. Metal/Oxide Interface of an Oxide Taken from the High Temperature Region of a Fuel Rod from PWR-A. It was Fractured in Liquid Nitrogen While the Oxide was Still Attached to the Metal Substrate (Sample 3).

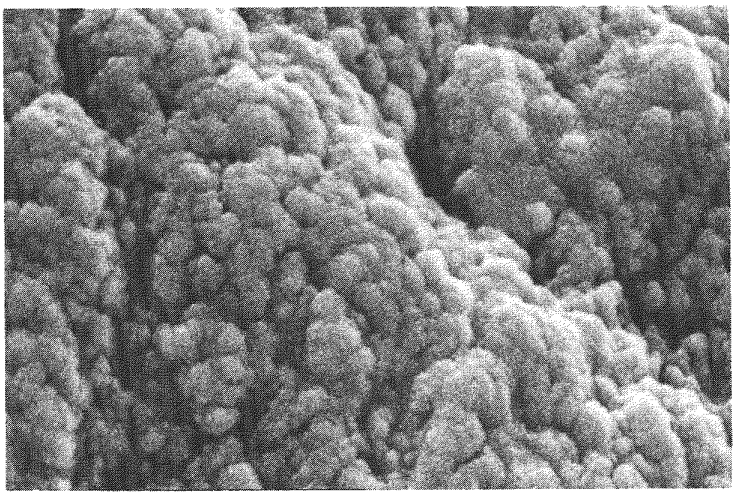

a) Peak Temperature Position (Sample 3)

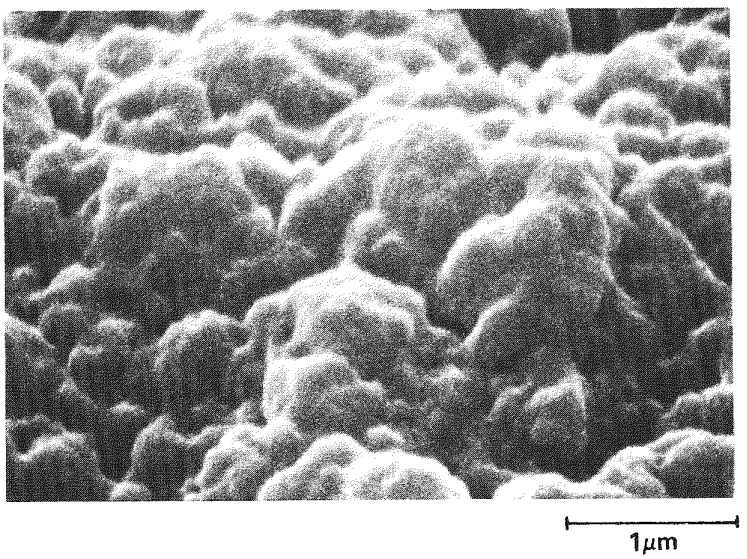

b) Low Temperature Position (Sample 2)

Figure 4-6. Surface of Oxide/Metal Interface of Stripped Oxide Samples from a Fuel Rod from PWR-A

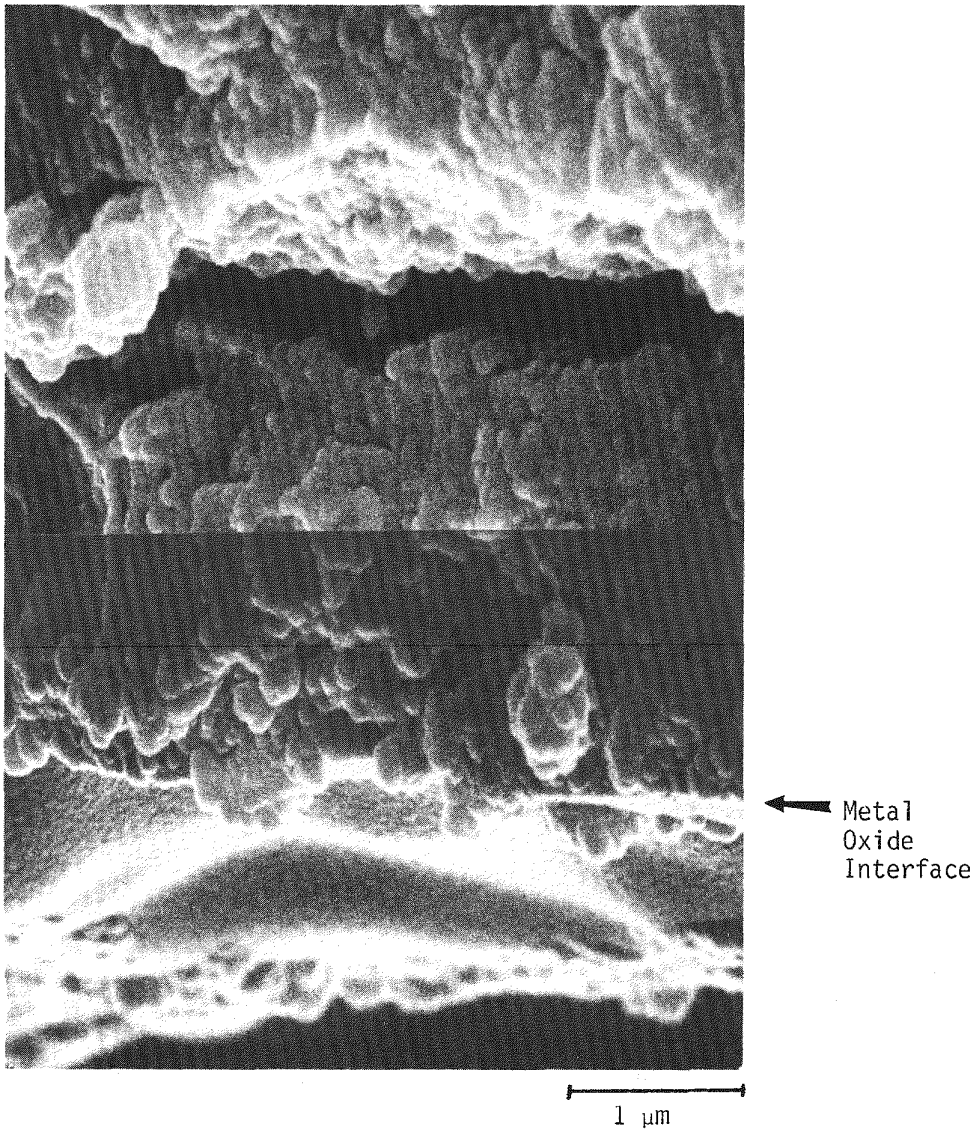

Figure 4-7 View of the Metal/Oxide Interface for Sample from the Peak Temperature Position of a Fuel Rod from PWR-A (Sample 3). The Granular Structure is Fully Developed in the Interface Region.

very close to the interface. This may be indicative of the presence of a dense thin inner-layer, with a thickness less than 0.5 μm.

The metal was chemically removed and the surface of the oxide metal interface was then examined by SEM. Figures 4-6 (a) and (b) show the appearance of this surface for oxide films grown in PWR-A at low and at peak temperature positions. The crystalline morphology seems to be almost fully developed in the peak temperature sample. The low temperature sample appears more diffuse and is very similar in appearance to samples grown in autoclaves in 350°C-water. However, oxides grown under steam conditions (475°C) had a clear crystalline microstructure. On the other hand fractured oxide samples (Figures 4-5 and 4-7) taken from the peak temperature positions from oxides grown in PWR-A showed some regions with a fully developed crystalline morphology, Figure 4-5, and some regions where the inner layer was less developed and diffuse, Figure 4-7. These measurements are summarized in Table 4-3.

Density, Specific Heat and Thermal Conductivity

The oxide density was determined by pycnometry and by the combined use of metallography and micrometer to determine oxide volume followed by dissolution and weighing of the remaining oxide, Table 4-4. The latter technique showed that the density of the unirradiated was 96% TD, whereas the irradiated oxide densities range from 79 to 89% TD. The more accurate pycnometry measurements made on large samples (~1gm) showed that the unirradiated oxide had a density of 91.4% TD while the irradiated oxide was similar, 92.1% TD. It is believed that irradiation does not appear to significantly influence the oxide layer density.

The specific heat was measured on unirradiated oxides formed in autoclave corrosion tests and on irradiated oxides formed in a PWR environment. The results given in Table 4-5 show that irradiation had no effect on the specific heat of the oxides. For example at 177°C the specific heat of unirradiated oxide was 555 J/g.K to be compared with 570 J/g.K for irradiated oxide.

Conductivity determinations were performed on several samples of tubing after autoclaving (958 d/ 343°C, water) to produce an oxide layer thickness of 31 μm. Measurements were also made on the PWR irradiated samples with oxide thickness ranging from 15 to 40 μm (Table 4-1). The results are shown in Fig. 4-8. The thermal conductivity of the autoclave oxide samples varies between

Table 4-4

ZIRCONIUM OXIDE DENSITY DATA

Reactor/Fuel Rod	Rod Average Burnup (MWd/t)	Axial Location from Bottom of Rod (mm)	Oxide Thickness (μm)	Oxide Density Technique	Oxide Density* (% TD)
D 89000	35600	3210-3030	21	Combined Metallography,	80.8, 88.8
A 430004	31300	2316-2266	33	Micrometry and Oxide	88, 88.1
A 28245	35200	2340-2160	21	Weighing	84.2, 80.4
A 28245	35200	2340-2160	24		79.2, 84.5
Autoclave Sample 400°C/18000 (steam)	0		44		96.4, 95.9
Autoclave Sample 400°C/18000 (steam)	0		44	Pycnometry	91.4
Combined Sample from D89000, A430004, A28245,	31300 35600		21-44		92.1

*Theoretical density is 5.82 g/cc

Table 4-5

ZIRCONIUM OXIDE SPECIFIC HEAT DATA

Measurement Temperature °C	Specific Heat Capacity J/g.K	
	Unirradiated	Irradiated
52	490	475
77	515	515
102	530	540
127	545	555
152	555	565
177	565	570
202	570	
227	578	
252	585	
277	590	
302	595	
327	600	
352	604	
377	608	
402	614	
427	622	
452	630	
477	639	
502	649	
527	657	

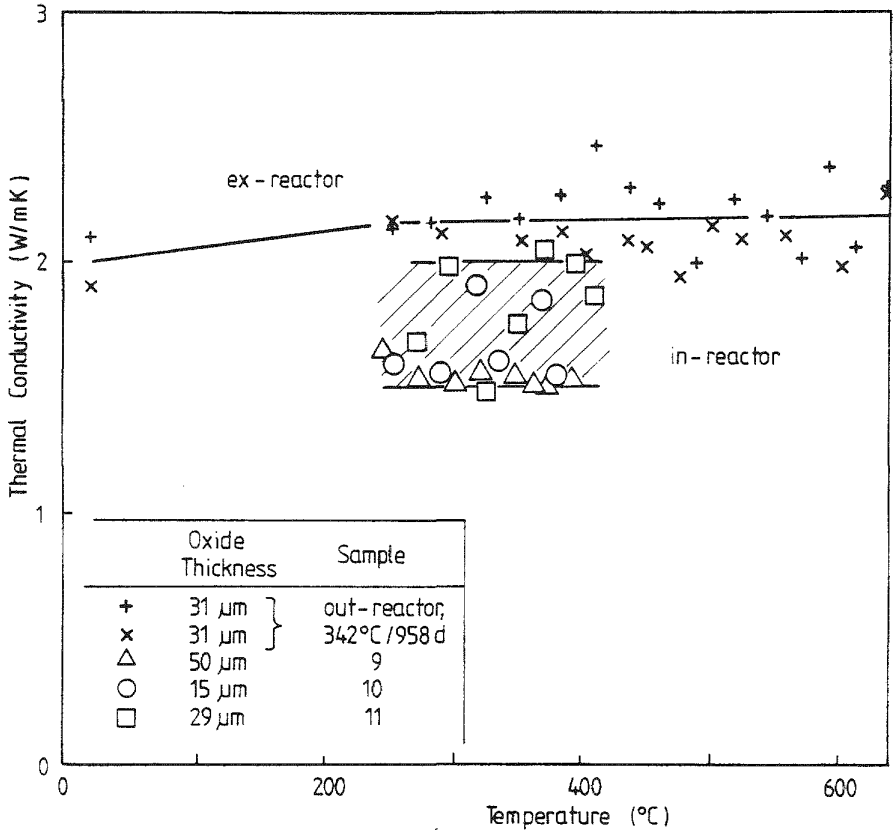

Figure 4-8. Thermal Conductivity of ZrO_2

1.9 to 2.4 W/m K, with little or no temperature dependence from room temperature up to 650°C. The thermal conductivity of the three irradiated oxide films ranged from 1.5 to 2.0 W/m.K, which is approximately 30% less than the unirradiated values. The thickest oxide samples had the lowest conductivity and, as expected, had a smaller scatter band than the thinner oxide samples.

X-Ray Diffraction

X-ray diffraction measurements on oxide films, formed in-reactor and in autoclave corrosion tests, showed that the crystal structure was mainly monoclinic with a trace of the tetragonal (high-temperature) phase. The crystal structure of irradiated and unirradiated films was similar. There was some broadening of the (111)-diffraction peak of the oxides formed in-reactor; the half-width of the peak had doubled. This indicates that the oxide lattice had sustained some irradiation damage.

Elemental Analyses of the Oxide

The results of IMA and electron-probe scans across the thickness of oxide samples showed that the oxide contains the alloying elements Sn, Fe and Cr in proportion to their concentration in the base metal. SIMS, which was conducted on the outer oxide surface, revealed increased Fe- and Cr- concentrations and also small amounts of Cu, possibly indicating the presence of some deposits from the reactor coolant. Boron and lithium compounds are both used in controlling the coolant chemistry; concentrations of up to 50 ppm B and 40 ppm Li were found in the oxides.

Chemical analyses, using the methods given in Table 4-2, were employed to detect the presence of the elements Li, B, F, Cl and Si in the oxide layer. The detection limits depend on the technique used and on the size of the oxide sample evaluated. As shown in Table 4-6, all impurity concentrations, with the exception of Li and in one case Si, were below the detectable limits which are also listed.

Impedance Measurements

The impedance and phase measurements of samples oxidized by anodizing are given in Figure 4-9; the samples were anodized in H_2SO_4 at 200 μA for times of

Table 4-6

CHEMICAL ANALYSES OF ZIRCALOY-4 OXIDES FORMED IN PWRs

Element	Concentration / ppm / Sample 3 PWR-A	Sample 4 PWR-D	Sample 6 PWR-D
B	<160	<750	<350
Li	36	<45	<21
F	<160	<750	<500
Cl	<160	<750	<500
Si	<100	750	<300

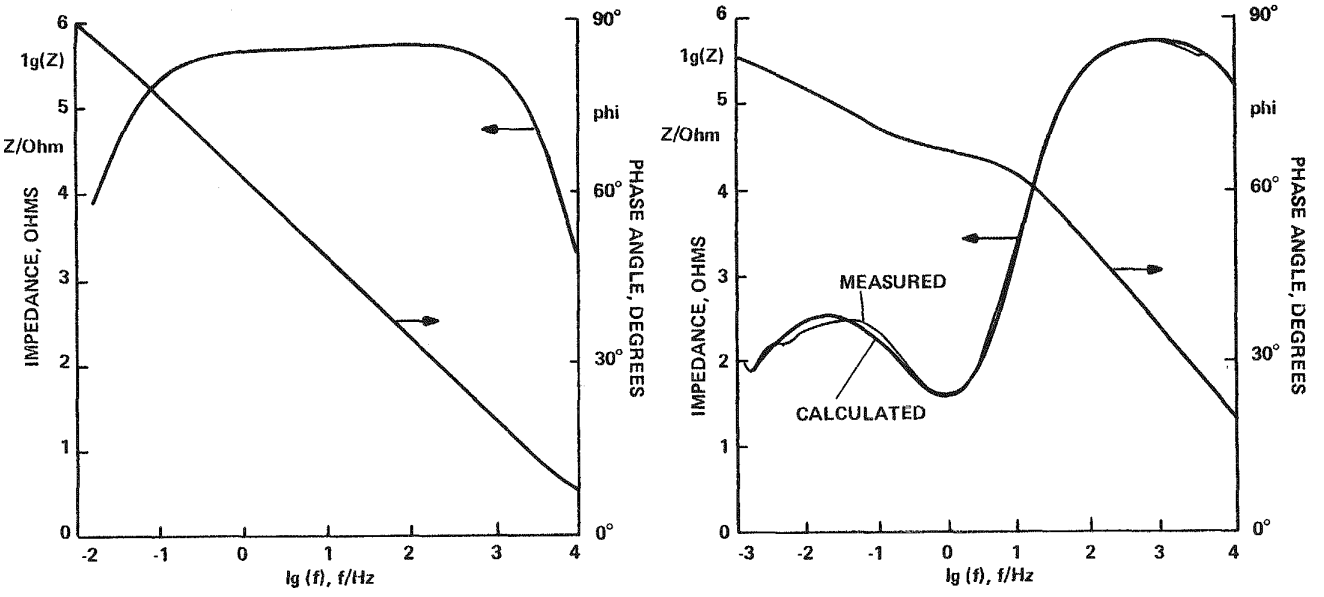

a) MONOLAYER CHARACTERISTIC AFTER AN ANODIC OXIDATION OF 200s

b) DUPLEX LAYER CHARACTERISTIC AFTER AN ANODIC OXIDATION OF 28000s

Figure 4-9. Typical Impedance - Measurements in 1m H_2SO_4

200 and 2800 seconds. The measurements show that the thin oxide, anodized for only 200 seconds, has the characteristics of a mono-layer. However, after 2800 seconds the oxide layer has the characteristics of a duplex oxide. In the latter case the oxide consists of a dense inner layer and a more porous outer layer.

These measurements, together with measurements made on samples oxidized in 350°C water and 650°C oxygen, are presented in Figure 4-10. Also shown are data from reference (13) for samples oxidized in 650°C oxygen. It can be seen that for thin oxides formed in the pre-transition regime up to 2 μm the dense inner oxide layer predominates. However after the transition to post-transition kinetics the porous outer layer grows in thickness and the dense inner layer either remains constant in the case of samples oxidized in 350°C water or actually decreases in thickness in oxides formed in higher temperature oxygen. These results are in agreement with the SEM observation in which the samples formed in 475°C steam are completely crystalline while the samples formed in 350°C water have an inner layer whose structure is difficult to resolve.

Surface Area and Pore Volume - Measurements

The estimated roughness factor (RF), which is the ratio between the geometrical and the BET surface area, the open porosity and the pore size are given in Table 4-7. In Figure 4-11 the results are compared with data from Dawson (14) and Asher (5). The preliminary data from this program agree with the results of Dawson (14) but differ significantly from those of Asher (5), who has used a somewhat different technique to characterize oxides formed out-of-pile. According to preliminary results and the results of Dawson (14) the internal roughness of the oxide is small up to transition and increases markedly during post-transition corrosion. This was expected from the impedance measurements. Fig. 4-12 compares the porosity distribution measured on the 82 μm thick oxide layer sample with measurements of Urquhart et al. (13). There is a significant fraction of the porosity with a pore size of < 10 nm, which represents the presence of pores rather than cracks.

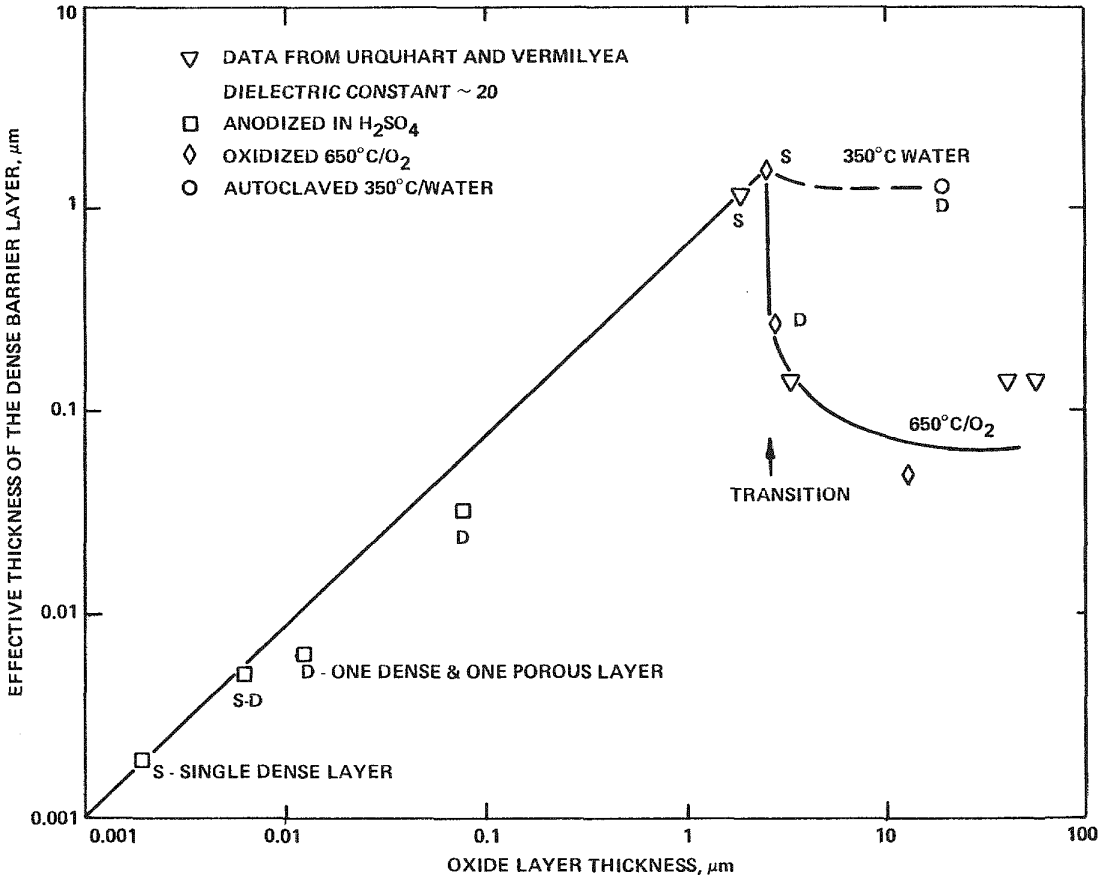

Figure 4-10. Results of Impedance Measurements on Irradiated Samples

Table 4-7

RESULTS OF BET-MEASUREMENTS

Sample	Oxide Thickness (μm)	Roughness Factor	Open Porosity (%)	Mean Pore Size (Å)
410/6.3 d + 500 °C/2.8 d + 550 °C/13.7 d/O_2	82	145, 204 212, 228 219	<0.6	20
350 °C/100 d/water	2	5, 7, 5	--	--
350 °C/350 d/water	5	36, 34	--	--
350°C/1000 d/water	29.5	45, 49	--	--

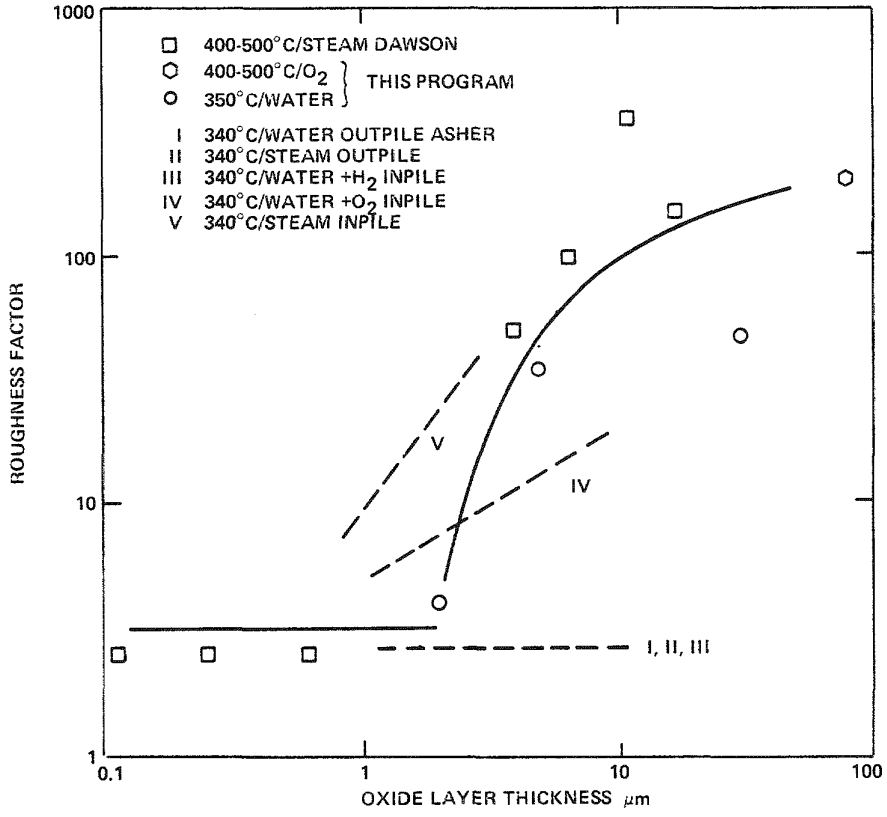

Figure 4-11. Comparison of Measured Roughness Factors with Literature Data

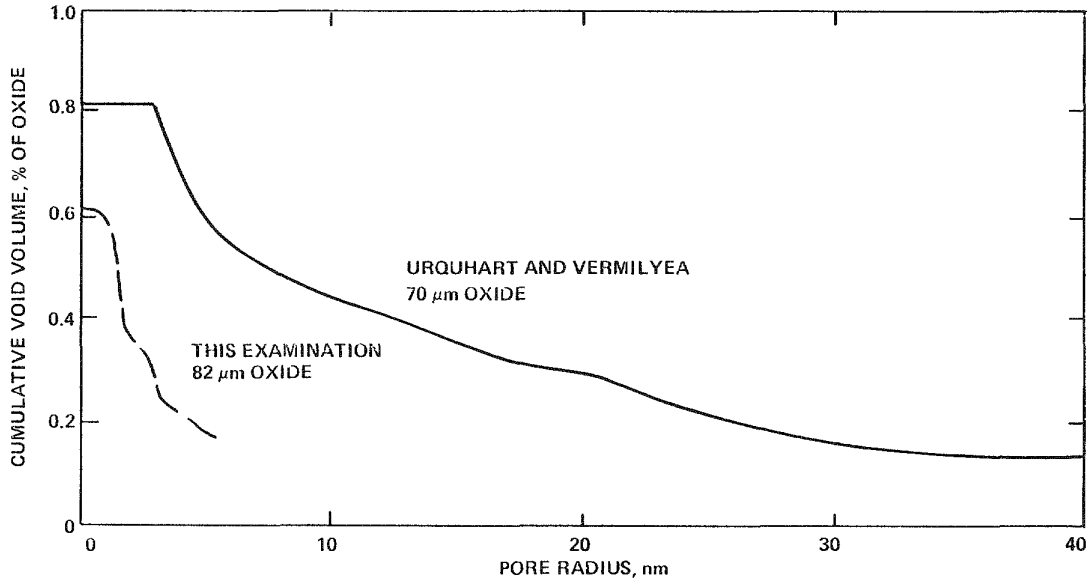

Figure 4-12. Porosity Distribution Curves from Desorption Hysteresis

Autoclave Testing of Irradiated Fuel Cladding Samples

Autoclave tests were conducted on samples previously oxidized in-reactor with the objective of evaluating how rapidly the enhanced corrosion rate would decrease to that anticipated from ex-reactor data. The tests were conducted in deionized water at 155 bars containing 600-1000 ppm B, 13 ppm Li and 2-3 ppm hydrogen.

The test results are presented in Figures 4-13, 4-14, and 4-15. In all cases the data are compared to the ex-reactor, post-transition corrosion rates predicted by equation (2-5) in reference (19). The results from autoclave tests on the BWR cladding are summarized in Figure 4-13. The samples were irradiated at an estimated temperature of about 290°C. After corrosion testing for 10 days the samples showed an average corrosion rate close to that measured in-reactor. However, with continued exposure at 280°C for 110 days, the corrosion rate continually decreased; after 110 days it was close to that expected from thermal corrosion alone. After increasing the corrosion temperature to 325 and to 350°C the measured corrosion rate agreed well with the ex-reactor rate anticipated for those temperatures. Decreasing the autoclave corrosion temperature to 300°C resulted in a reduction in the corrosion rate to a value slightly below that expected ex-reactor.

The results of autoclave tests for the samples from PWR-D are shown in Figure 4-14. Three samples were used, representing different exposure times and different axial positions. The final in-reactor corrosion rate and the final temperature at the metal/oxide-interface are shown for each sample. The post-irradiation corrosion behavior was similar for all three samples. The measured autoclave corrosion rates were higher by a factor of 2 over typical ex-reactor rates up to a test temperature of 325°C or a total exposure time of 180 days. At 350°C the corrosion rate agreed well with the expected ex-reactor rate.

The samples from PWR-A behaved differently than the samples from PWR-D, and the results are shown in Figure 4-15. During the first 30 to 50 days, samples from the high temperature position continued to corrode rapidly, although the autoclave corrosion temperature was approximately 60°C lower than the in-reactor exposure temperature. Furthermore, these samples continued to exhibit enhanced corrosion throughout the entire test. The samples from the low temperature position in the reactor behaved similarly to the samples from the PWR-D (i.e., the memory effect was less pronounced).

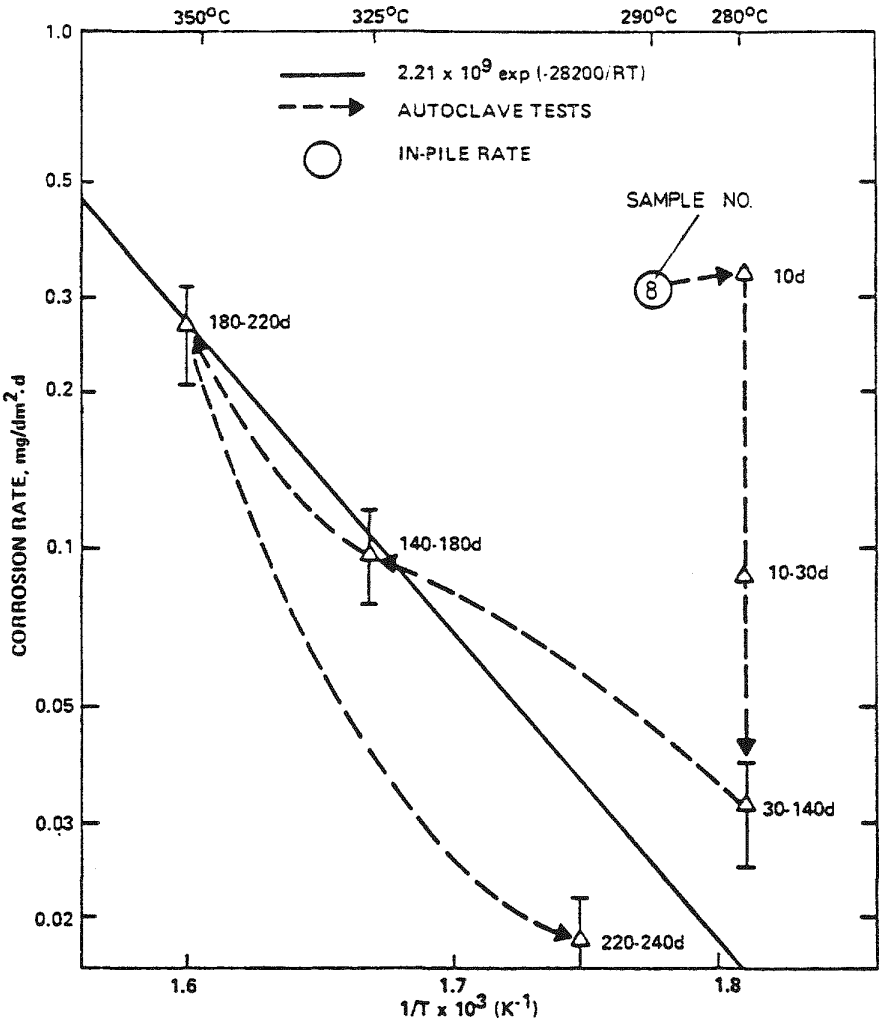

Figure 4-13. Post-Irradiation Autoclave Corrosion Tests of Samples from a BWR

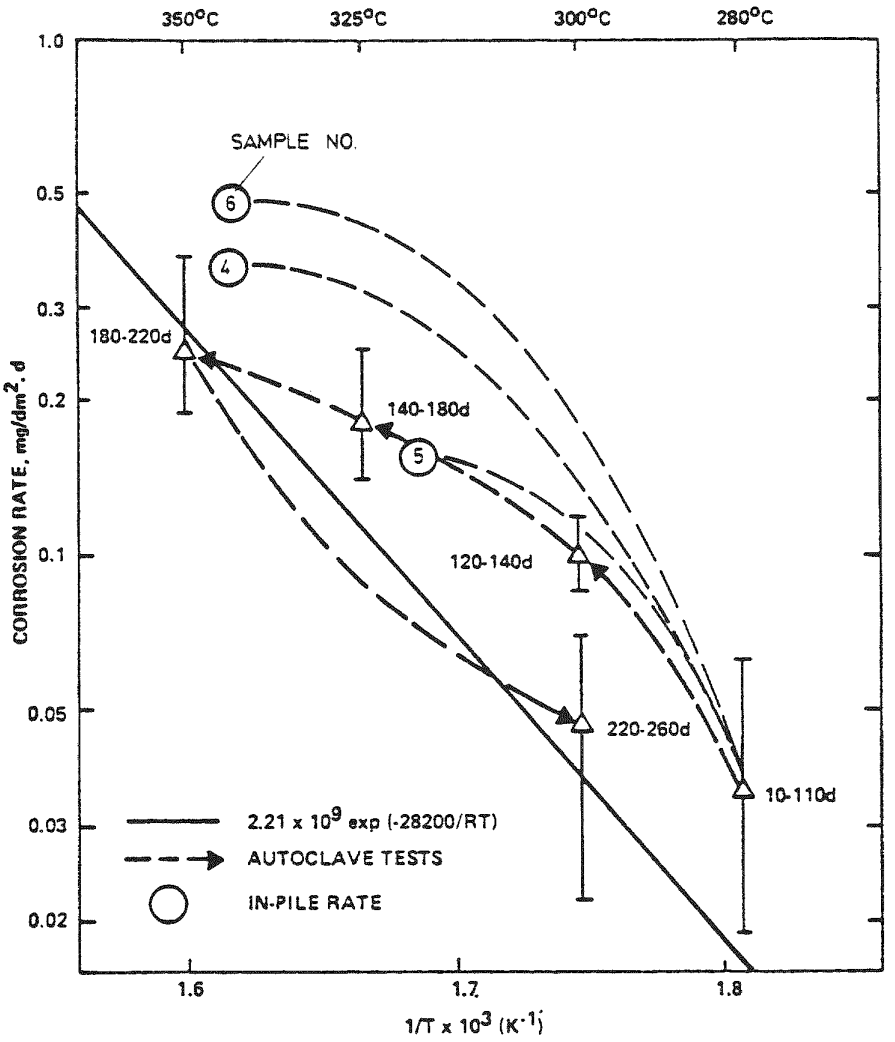

Figure 4-14. Post-Irradiation Autoclave Corrosion Tests of Samples from PWR-D

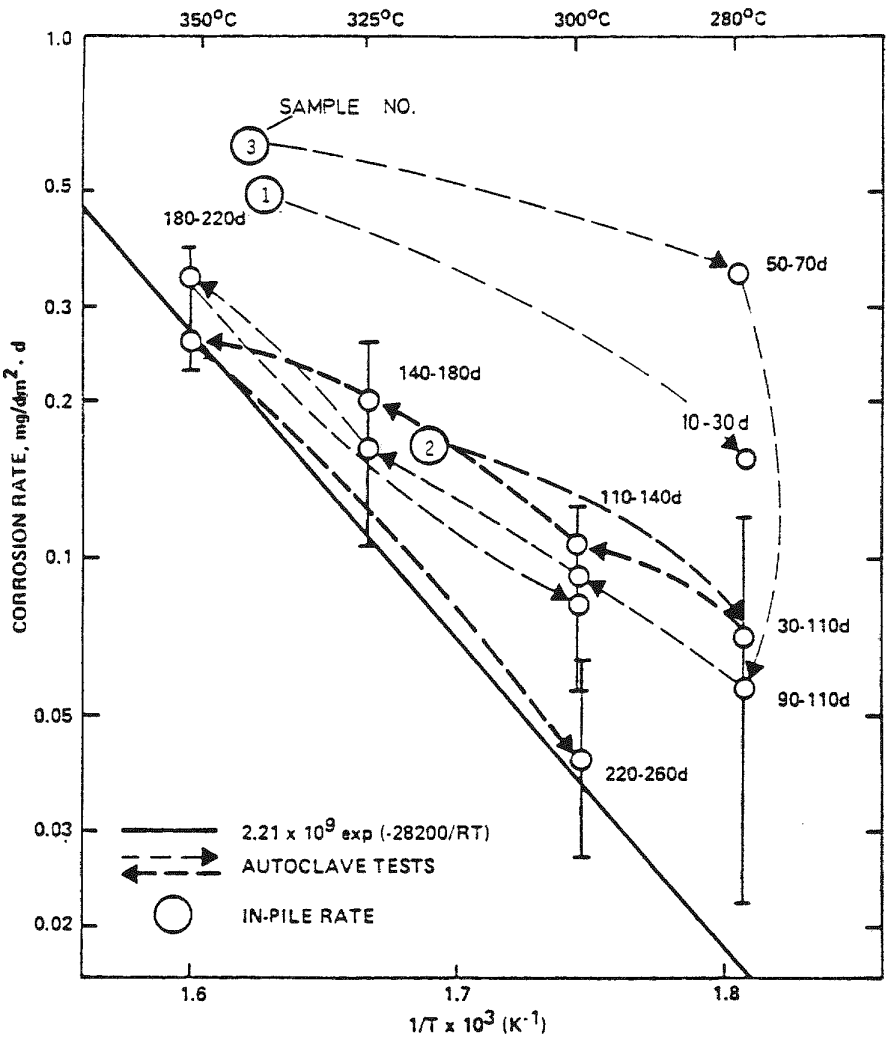

Figure 4-15. Post-Irradiation Autoclave Corrosion Tests of Samples from PWR-A

These autoclave corrosion data are presented in Figure. 4-16. The enhancement of the measured post-irradiation corrosion rate, relative to that expected from ex-reactor tests, is shown as a function of the oxide layer thickness formed during the autoclave tests. The memory effect in the BWR samples disappeared after an additional 0.5 μm of oxide layer had developed. The memory effect of the samples from PWR-D and from the lower temperature position of PWR-A disappears when the oxide layer is 1.5 μm thicker. The samples from the peak temperature position of PWR-A show a more lasting memory effect; corrosion is still enhanced even after an additional oxide layer thickness of 2 μm. For comparison, the post-transition corrosion rate corresponds to the pre-transition corrosion rate when a 1 μm thick layer has formed.

DISCUSSION

The most important outcome of this investigation is that oxide films formed in PWRs maintain their integrity up to thicknesses of 70 μm and burnups of 52 GWd/t without any local breakdown which could degrade heat transfer. Fuel rod axial growth of up to 1% and fuel rod creep-down of up to 0.8% that occur during irradiation have no effect on the integrity of the oxide layer. This conclusion is based on the examination of large bulk samples of oxides to determine the oxide film thermal conductivity. The local cracking observed during the SEM and metallographic examinations, even if present in the bulk samples, did not degrade the measured thermal conductivity. Measurements made by Cox (20) and Bryner (21) suggest that these cracks may be formed during sample preparation, although this cannot be determined conclusively.

The elemental analyses of potential impurities in the oxide gave no indication of any significant enrichment of chemical species (including lithium) in the oxide layer. Thus, pickup of impurities by the oxide does not appear to be responsible for the observed in-reactor acceleration of Zircaloy corrosion.

Irradiation does not cause large changes in the oxide layer density or thermal conductivity. The thermal conductivity values are quite high in oxides formed during autoclave tests and in oxides formed in-reactor; the conductivity of the unirradiated oxide of 2.2 W/m-K falls within the scatter-band of the values for sintered ZrO_2 (1.8 - 2.7 W/m-K) reported in the literature; the conductivity of irradiated oxides is about 30% lower (1.5 -2.0 W/m-K). These new values are substantially higher than those determined previously on unirradiated samples by the same laboratory using the identical method (22). The use of larger

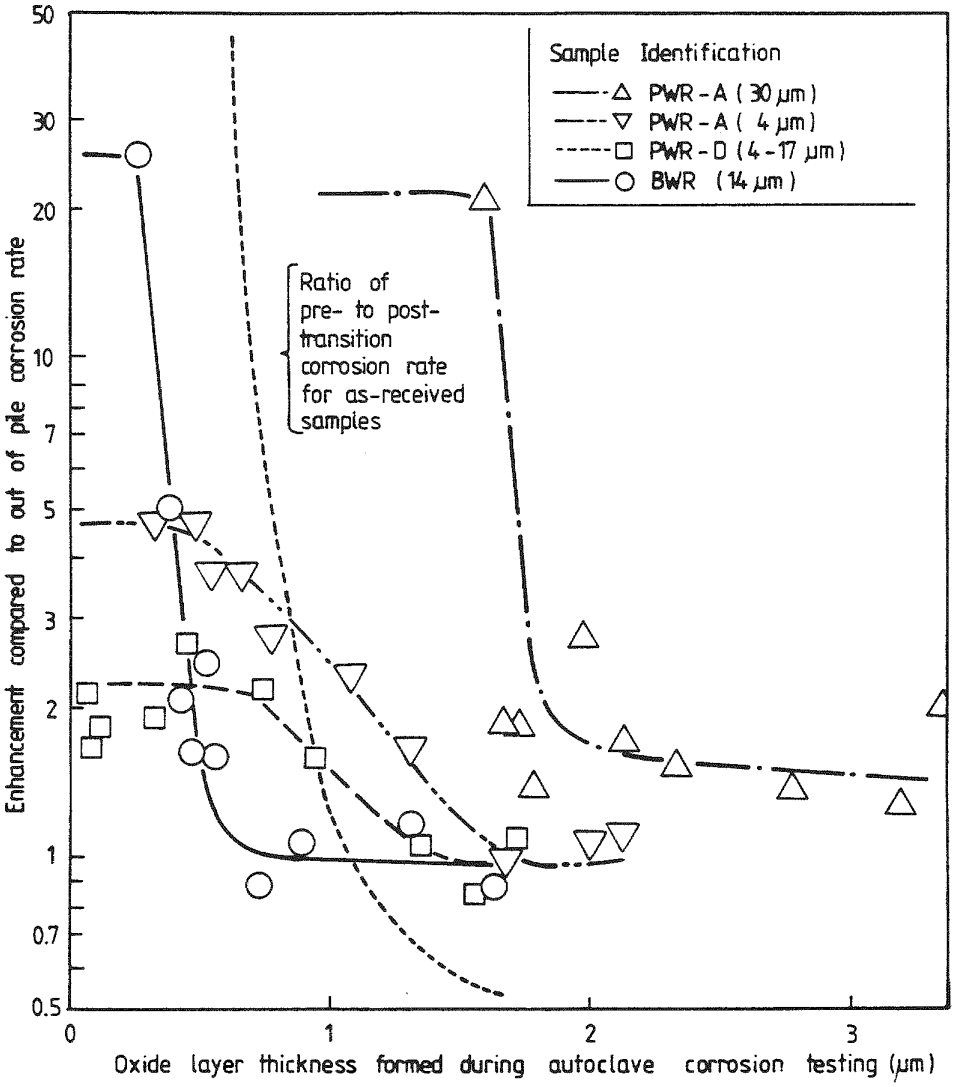

Figure 4-16. Summary of Post-Irradiation Autoclave Corrosion Tests

samples in the present investigation minimizes any potential damage to the oxide layer that may degrade the oxide thermal conductivity. For this reason the data obtained in this program are believed to be representative of the thermal conductivity of zirconium oxide corrosion films that form in-reactor.

The X-ray data show that irradiation does not modify the oxide crystal structure and that the bulk of the oxide consists of the monoclinic phase with some tetragonal oxide. X-ray diffraction analysis indicated some radiation-induced damage to the crystal lattice.

The modest in-reactor enhancement of corrosion in PWRs is in agreement with the slight changes in the physical properties of the irradiated oxides. As discussed in Section 7, the in-reactor enhancement is small for thin oxide layers and appears to increase and then saturate as the oxide layer thickens.

Several models for the corrosion of Zircaloy have been proposed in the past, and two are currently under consideration. Based on the observed laminated structure of the oxide, one model (21, 24), explains the post-transition corrosion mechanism by repeated cycles of cube-root kinetics. During each cycle, a new protective layer grows at the metal/oxide interface. The other model (20) attributes the transition from pre-transition corrosion kinetics to post-transition corrosion kinetics to a change in the oxide morphology which produces a porous microstructure in the bulk of the oxide. The post-transition corrosion rate is controlled by a thin, inner layer close to the metal substrate, which may be partially amorphous.

A laminated oxide structure also has been seen in the present investigation with negligible interlinkage through radial cracks. These cracks may be formed in-situ during the corrosion process or may become fully developed during sample preparation. If the cracks form during preparation, or are present in-reactor, but do not control corrosion, then the observations from this program may be explained on the basis of a crystallization and porosity model. The SEM observations show that the bulk of the oxide has a granular structure with spherical granules providing pores at the triple points. Porosity of less than 10 nm has been reported from porosimetry measurements of unirradiated specimens (25). Preliminary absorption/desorption measurements at liquid nitrogen temperature using a micro-balance confirmed the existence of open porosity in the oxide layer with an average pore size just in this range. The time-

averaged thickness of the inner layer close to the metal substrate and its thickness fluctuation may result from the dynamic equilibrium between the rate of crystallization and the rate of formation. The kinetics and the rate of oxidation are mainly controlled by the average thickness of the inner layer and by the fraction of the surface covered by this layer. The x-ray line broadening implies radiation damage to the oxide lattice. The stored energy due to this damage may increase the driving force for crystallization of the inner layer.

The appearance of the dense, inner layer was found to be different in both the irradiated and unirradiated samples examined. As mentioned previously, the SEM examination revealed a clear difference in structure between the water and steam-autoclave samples. Differences in the effective inner layer thickness were also inferred from some preliminary impedance measurements of unirradiated specimens in which the electrolyte used penetrated the open porosity. These latter measurements revealed that the effective thickness of the electrically insulating barrier layer was about 1 μm for oxides formed in water and less than 0.1 μm for oxides formed in steam. The characteristics of the oxides formed in-reactor (Table 4-3) may correlate with the corrosion enhancement factors (Table 4-1). In the samples with higher enhancement factors, the inner layer appeared to be predominantly crystalline, whereas the inner layer in the samples with the lower enhancement factors was found to be more or less diffuse.

It is proposed that there are two reasons for the enhancement of the corrosion rate in a PWR environment: (1) irradiation might accelerate the crystallization of the oxide in the inner layer close to the metal substrate, thereby reducing the equilibrium thickness and the degree of coverage of the dense protective layer, and (2) the environmental conditions (i.e., the concentration of the radicals in the coolant), the impurity concentration, and the physical structure of the oxide may vary across the cross-section of the outer non-protective oxide. This may be the reason for the increase of the in-reactor enhancement factor with increasing oxide thickness. However, it is very difficult to evaluate the detailed chemistry of the medium within an oxide having an extremely fine interconnected porosity, especially in an environment where both irradiation and a heat flux are present. On the other hand, it can be concluded from the various elemental analyses performed, that only traces of foreign atoms are incorporated in the oxide crystal lattice. Under heat flux conditions, it is possible to have steam and water present in the oxide pore system. In this respect, attention should also be given to the work of Asher

(5) who concluded that the irradiation enhancement is higher in a steam environment than in hydrogenated water.

The findings with respect to the memory effect also fit into this picture. There was a pronounced and lasting memory effect in only those samples which exhibited high in-reactor enhancment and where crystalline oxide extended up to metal substrate. The samples with the lower corrosion enhancement factors had a more diffuse inner layer and exhibited a less pronounced memory effect. This hypothesis is also in line with studies of the temperature memory effect in autoclave testing as reported by Kass (26) where a strong memory effect was only found if the prior exposure was performed in steam. As we have shown, under such conditions the interfacial oxide morphology is predominantly crystalline.

CONCLUSIONS

The integrity of the oxide layer was found to be excellent without any indication of local changes in appearance for thicknesses up to 70 μm and burnups up to 52 GWd/t(U).

The thermal conductivity of oxides formed in a PWR environment does not change significantly; there is only a 30% decrease from that measured on unirradiated oxide samples.

The observations of the oxide microstructure, as well as the memory effect, can be explained on the basis of a mechanism which considers oxide crystallization near the metal/oxide interface and the formation of interconnected fine porosity in the outer bulk of the oxide.

The modest in-reactor corrosion enhancement observed in the PWR environment may be partly due to accelerated crystallization and grain growth of the oxide and partly due to changes of the corrosion environment within the porous outer section of the oxide film. Within the fine pores of the oxide layer, the localized concentration of alloying elements, impurities and chemical species generated by radiolysis may result in a change in the corrosion environment.

REFERENCES

1. Cox, B., Journal of Nuclear Materials, Vol. 28, 1968, pp 1-47.

2. Hillner, E., Zirconium in the Nuclear Industry, ASTM STP 663, American Society for Testing and Materials, 1977, pp 211-235.

3. Garzarolli, F. and Manzel R., "Corrosion Resistance of Zircaloy in KWU Power Reactors", presented at the Reactortagung, 1977, Mannheim, Germany.

4. Videm, K., Nuclear Engineering and Design, Vol. 33, 1975, pp 170-177.

5. Asher, R. C., Davies, D., Kirstein, T.B.A., McCullen, P. A. J., and White, J. F., Corrosion Science, Vol. 10, 1970, p 695-707.

6. Johnson, Jr., A. B., Applications-Related Phenomena in Zirconium and its Alloys, ASTM STP 458, American Society for Testing and Materials, 1968, pp 301-324.

7. Garzarolli, F., Manzel, R., Reschke, S., and Tenckhoff, E., Zirconium in the Nuclear Industry, ASTM-STP-681, American Society for Testing and Materials, 1978, pp 91-106.

8. Trowse, F. W., Summerling, R., and Garlick, A., Zirconium in the Nuclear Industry, ASTM-STP-633, American Society for Testing and Materials, 1977, pp 211-235.

9. Dalgaard, S.B., Abstract 31, Electrochemical Society Extended Abstracts, Vol 76-1, May 1976.

10. Stehle, H., Kaden, W., and Manzel, R., Nuclear Engineering and Design, Vol. 33, 1975, pp 155-169.

11. Hillner, E., Zirconium in Nuclear Applications, ASTM-STP-551, American Society for Testing and Materials, 1973, pp 449-462.

12. Dickson, I. K., Evans, H. E., and Jones, K. W., "A Comparison Between the Uniform and Nodular Forms of Zircaloy Corrosion in Water Reactors", London, England: Central Electricity Generating Board, Berkeley Nuclear Laboratories, November 1977, RD/B/N3964.

13. Urquhart, A. W. and Vermilyea, D. A. "Characterization of Zircaloy Oxidation Films", ASTM STP 551, 1974, pp 463-478.

14. Dawson, J. K. Long, G., Seddon, W. E., and White, J. F., "The Kinetics and Mechanism of the Oxidation of Zircaloy at 350-500°C", J. of Nuclear Materials Vol 25 (1968) pp 179-200.

15. Gilchrist, K. E., and Brocklehurst, J. E., Atom No. 240, 1976.

16. Gilchrist, K. E., First European Conference on Thermophysical Properties of Solids at High Temperatures, Baden, BMBW-FBK 70-01 1968.

17. Garzarolli, F., H. Schoenfeld, D. B. Scott and P. G. Smerd. CE/KWU/EPRI Task C Interim Report "Characterization of Corrosion Films on Irradiated Zircaloy Clad PWR Fuel Rods", RP 1250-01. Combustion Engineering, Inc., May 1982, CE NPSD-192.

18. Gilchrist, K. E., "Measurements of the Thermal Conductivity of Zirconium Oxide Corrosion Films on Irradiated and Unirradiated PWR Zircaloy Fuel Cladding", SL-CON-38, December, 1981.

19. Garzarolli, F., Jorde, D., Manzel, R., Parry, G. W., and Smerd, P. G., "Review of PWR Fuel Waterside Corrosion Behavior", EPRI NP-1472, June, 1979.

20. Cox, B., "Mechanism of Corrosion of Zirconium Alloys in High Temperature Water", presented at the Electromechanical Soc. Meeting, Denver, Colorado, October 1981.

21. Bryner, J. S., Journal of Nuclear Materials, Vol. 82, 1979, pp 84-101.

22. Gilchrist, K. E., Journal of Nuclear Materials, Vol. 82, 1979, pp 193-194.

23. Garzarolli, F., Suchy, P., and Smerd, P. G., American Nuclear Society Topical Meeting on LWR Extended Burnup Fuel Performance and Utilization held in Williamsburg, Virginia, April 4-8, 1982, pp 4-71 - 4-87.

24. Sabol, G. P. and McDonald, S.G., "Stress Effects and the Oxidation of Metals", Ed. J. V. Cathcart published by AIME 1979, pp 353-372.

25. Cox, B., Journal of Nuclear Materials, Vol 27, 1968, pp 1-11.

26. Kass, S., Corrosion, Vol 23, 1967, pp 374-378.

Section 5

COOLANT CHEMISTRY EFFECTS

INTRODUCTION

The in-reactor corrosion of Zircaloy fuel cladding can be influenced by the presence of oxygen and oxidizing radicals formed by the radiolysis of water. In PWRs, a hydrogen overpressure is maintained to suppress the formation of oxygen and oxidizing radicals in the coolant water. Calculations (1) have shown that for hydrogen concentrations greater than 0.5 ppm, the oxygen concentrations in water become undetectable, and the effect of oxidizing radicals is minimized for hydrogen levels of more than 2 ppm. Consequently, most PWRs operate at hydrogen concentrations of 2 to 4 ppm in the coolant. However, subcooled boiling in PWRs may preferentially strip the hydrogen from water locally (1), thereby increasing the local concentration of oxygen and oxidizing radicals. Furthermore, the simple oxidizing radicals may react with other impurities such as N, NH_3 or metal ions present in water to form complex stable oxidizing species (e.g., NO_x, chromate, trivalent Fe, etc). Under typical PWR conditions, the complex oxidizing species may be stable for a longer period than the simple parent oxidizing radicals. This may be the reason for the recently reported high concentrations of NO_x during periods of high NH_3 concentrations in the Neckarwestheim PWR (2). The principal consequence of such stable oxidizing species is to shift the corrosion potential of the coolant/metal interface to more positive values. The extent of this shift depends on the redox potential of these species and on their concentration. The oxidizing compounds formed in regions of subcooled boiling may have sufficiently long half lives to migrate to areas where subcooled boiling does not occur. The high concentration of the migrating oxidizing compounds may influence the redox potential and therefore the extent of corrosion even in areas where sub-cooled boiling does not occur.

In addition, certain impurities may concentrate on the surface of a fuel rod which may in turn influence corrosion. One such impurity is lithium. Lithium hydroxide is used to control the pH of the bulk coolant and can concentrate in the oxide film. Isothermal laboratory experiments conducted by Hillner and Chirigos (3), performed in 360°C water, have shown that the presence of lithium

hydroxide accelerates Zircaloy corrosion and increases the hydrogen pickup fraction only when the pH exceeds 11.3. No effect was observed for lower pH values. In PWRs a local concentration of lithium in the thick oxide layers, especially those formed under local boiling conditions, may enhance corrosion even for the standard PWR pH conditions. However, the results reported in Section 4 suggest that lithium was not picked up in sufficient quantities by the oxide film to account for the observed in-reactor accelerated corrosion of Zircaloy. There are other species which are either known or have been suspected to increase corrosion, e.g. fluorides, chlorides, various metal oxides, various suspended metallic compounds and resin compounds.

The following evaluations were conducted to assess the effects of impurities on Zircaloy waterside corrosion:

1. Electrochemical measurements of the corrosion potential in high temperature water to evaluate the effects of oxidizing species present in the water in low concentrations.

2. Autoclave corrosion tests in high-temperature water to study the influence of a range of impurities on the corrosion behavior of Zircaloy.

3. Special impurity concentration measurements of coolant from two PWRs.

4. Collection of data on primary coolant water chemistry for six PWRs.

EXPERIMENTAL

Autoclave Electrochemical Measurements

In many systems, corrosion resistance is generally influenced by the corrosion potential. To investigate the influence of corrosion potential on the waterside corrosion of Zircaloy, the corrosion potentials of specimens A to D (Table 5.1) were measured using Ag/AgCl reference electrode in water at 290°C in a 10-liter Inconel-600 autoclave at the KWU Laboratories in Erlangen (4). The measurements were performed in a 30 liter volume dynamic system with water flowing through the autoclave at a rate of 7 liters/hour. The environmental conditions (impurity concentration in the water) during the electrochemical tests were varied. The types of aqueous media investigated are listed in Table 5.2. The oxygen level was varied either by adjusting the partial pressure over the tank or by the addition of N_2H_4. The other additives listed in Table 5.2 were directly added to the feed tank and their concentration levels determined by a quantitative analysis of the

Table 5-1

SAMPLES USED FOR ELECTROCHEMICAL MEASUREMENTS IN 290°C WATER

Sample	Oxide Layer Thickness (μm)	Oxidation Conditions, Temperature Time	Additional Oxides Deposited on the Zircaloy Samples
A	20-40	350°C/1000d	---
B	20-40	350°C/1000d	Fe_3O_4
C	20-40	350°C/1000d	74% Fe_3O_4+18% NiO+7% Cr_2O_3+1% SiO_2
D	(0.3-0.6)	290°C/750d	---

Table 5-2

AQUEOUS SOLUTIONS USED IN THE ELECTROCHEMICAL TESTS

Type	Concentration Range O_2 (ppm)	Li (ppm)	B (ppm)	Other Additions
I	<0.01 to 8	0 to 6	0 to 2200	None
II	<0.01 to 8	0 to 6	0 to 2200	$Fe_2(SO_4)_3$+$Fe_3(SO_4)_2$
III	<0.01 to 8	0 to 6	0 to 2200	$Cr_2(SO_4)_3$+K_2CrO_4
IV	<0.01 to 8	0 to 6	0 to 2200	NH_4NO_3
V	<0.01 to 8	0 to 6	0 to 2200	$K_2S_2O_7$+$Na_2S_2O_5$

water samples from the condenser outlet. The potential was measured using a Wenking PPT 70 electrometer and polarization measurements were performed at polarization rates of 0.09 and 1.0 V/h using an AMEL 552 potentiostat.

Mini-autoclave Corrosion Tests with Addition of Impurities

Corrosion tests were conducted at KWU laboratories in Erlangen in small tubular autoclaves fabricated from Zircaloy. The dimensions of the autoclaves were 10.74 mm OD, 80 mm length and wall thickness 0.72 mm. The corrosion specimens were 50 mm long quarter circumference segments cut from 10.75 mm OD, 0.72 mm wall thickness Zircaloy-4 tubes from two lots with different final heat-treatment: stress-relief annealed and recrystallized. The corrosion samples were pickled after machining. After loading the corrosion specimen in the autoclave, the autoclave was approximately half filled with water containing several additives (Table 5.3), and the tubular autoclave was sealed by resistance welding the end plugs. The mini-autoclaves were placed in a furnace at 350°C. The autoclaves were opened periodically at 50 day intervals to measure the weight gain of individual specimens after rinsing and drying. The autoclave solution was replaced with fresh solution after each inspection.

Special Chemical Analyses of the PWR Coolant Chemistry

Special analyses of the impurities in the PWR coolant were conducted at Reactors A and E in October 1981 and March 1982. The October 1981 measurements were based on water samples taken from the 1-liter routine sampling tank (Fig. 5.1) and the concentrations of the following species were measured: NH_3, NO_2^-, NO_3^-, Cr^{6+} and total Cr. Water from the reactor purification circuit was circulated through the sampling tank for some time before collecting the water samples for analysis. In March 1982, 100 to 400 liters of the reactor coolant was subjected to high pressure filtration and ion-exchange sampling using various micropore filters and ion-exchange papers (Fig. 5.1).

The circulating crud collected from the high pressure filtration system was analyzed by SEM and X-ray diffraction techniques at KWU hot cells in Karlstein. Chemical analyses were conducted using the techniques listed in Table 5.4.

Table 5-3

CORROSION MEDIA USED FOR TESTS IN MINI-AUTOCLAVES

a	Pure water
b	PWR-water Chemistry (Li + B)
c.1	PWR-water Chemistry + 1 ppm Fe
c.2	PWR-water Chemistry + 10 ppm Fe
c.3	PWR-water Chemistry + 100 ppm Fe
c.4	PWR-water Chemistry + 0.05 ppm Cr
c.5	PWR-water Chemistry + 0.5 ppm Cr
c.6	PWR-water Chemistry + 5 ppm Cr
c.7	PWR-water Chemistry + 50 ppm Cr
d	same as c.3 or c.7 + 23 wt % Fe_3O_4
e	same as c.3 or c.7 + mixed oxide*
f.1	PWR-water Chemistry + 23 wt % Fe_3O_4
f.2	PWR-water Chemistry + 23 wt % Mixed Oxide*
f.3	PWR-water Chemistry + 23 wt % Cr_2O_3
f.4	PWR-water Chemistry + 23 wt % NiO
f.5	PWR-water Chemistry + 23 wt % $NiFe_2O_3$
g.1	PWR-water Chemistry + 23 wt % Resins
g.2	PWR-water Chemistry + 100 ppm Fe-Nitrate
g.3	PWR-water Chemistry + 100 ppm Fe-Chlorate
g.4	PWR-water Chemistry + 10 ppm Ag
g.5	PWR-water Chemistry + 10 ppm Cu

* Composition of Mixed Oxide is 0.37 wt % Fe_3O_4 + 0.4 wt % NiO + 0.02 wt % Cr_2O_3.

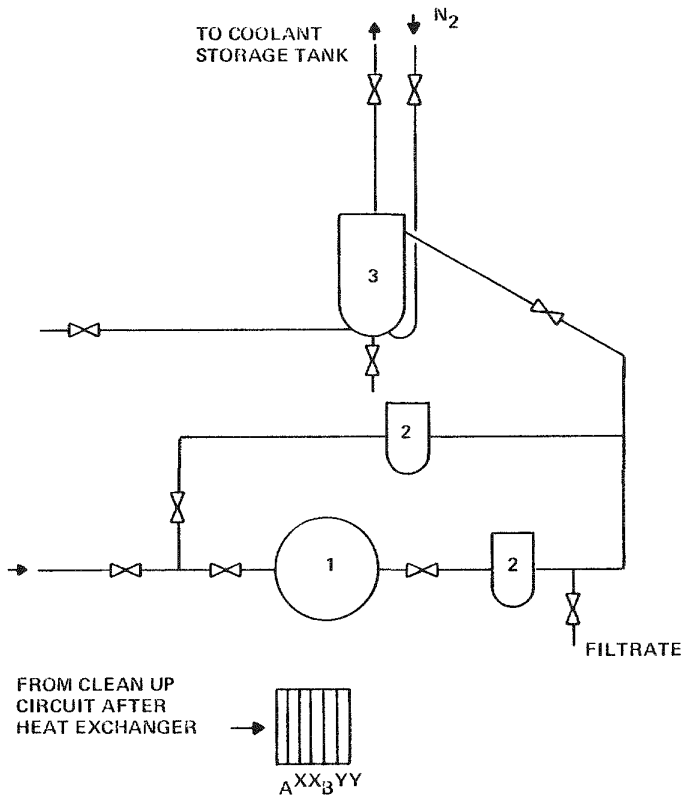

1 HIGH PRESSURE FILTRATION UNIT
2 WATER GAGE
3 SAMPLING TANK FOR ROUTINE ANALYSIS

SAMPLING PAPERS
A 0.1 μm FILTER MEMBRANE
B 0.45 μm FILTER MEMBRANE
X CATION-RESIN PAPER
Y ANION-RESIN PAPER

Figure 5-1. Primary Coolant Sampling System

Table 5-4

CHEMICAL ANALYTICAL METHODS USED IN THE ANALYSES OF IMPURITIES IN THE PWR COOLANT

Chemical	Methods
Ni	Photometry
Cr	Photometry after oxidation
Cr^{6+}	Photometry
NH_3	Photometry with gas sensitive electrode
NO_2^-	Photometry
NO_3^-	Photometry after reduction
Crud particles	EDMA - SEM

RESULTS

Electrochemical Measurements

The results of the electrochemical measurements are listed in Tables 5.5, 5.6 and 5.7 and given in Fig. 5.2. The duplicate test results shown in Table 5.5 indicate good reproducibility of the measurement techniques. The results for specimen A in Table 5.6 show that for a typical PWR water chemistry (600 ppm B and 1.5 ppm Li) without any additional impurities, the corrosion potential of Zircaloy covered with thick zirconium oxide (without any crud layer) at 290°C is between -0.61 to -0.62 volts with reference to a standard hydrogen electrode (SHE). The results shown in Fig. 5.2 demonstrate the shift in the corrosion potential with impurity addition to the coolant. Oxygen and Cr^{6+} ions have a strong effect on the corrosion potential in the concentration ranges of 0.01 to 0.1 ppm and 0.1 to 1.0 ppm respectively. A steep increase in corrosion potential is also observed for NO_3^- additions in the 5 to 100 ppm concentration range. The increase in the corrosion potential due to the addition of Fe^{3+} and SO_4^{2-} is less dramatic. Whereas the effect of nitrate and trivalent iron-additions was long lasting (the effect persisting for test times greater than 50 h) the effect of chromate additions appeared to diminish after a test time of 40 h because of the rapid drop in the chromate concentration. From this drop in concentration, the half-life of the various oxidizing species under typical PWR-water chemistry conditions can be determined. The half-life time was estimated to be 100 to 1000 h for nitrate and trivalent iron and only 2 h for chromate ions.

The corrosion potential of a platinum reference electrode (Table 5.7) was found to be almost the same as for Zircaloy samples with a thick oxide layer (Specimen 8). As expected, a Zircaloy sample with only a thin oxide layer (Specimen D with 0.3 - 0.6 μm oxide) showed more negative corrosion potentials, at least during the initial measurements, where the anticipated corrosion rate is much higher than the rate expected for samples with thick oxide. Deposition of a layer of synthetic crud or Fe_3O_4 had a little effect on the corrosion potential of oxidized Zircaloy as evident from the results for Specimens A, B and C in Table 5.6.

The results of the polarization measurements are shown in Figs. 5.3 and 5.4. Fig. 5.3, shows that the anodic polarization behavior, measured at 290°C in water with PWR chemistry (600 ppm B, 1.5 ppm Li), of platinum and oxidized Zircaloy specimens with different oxide thicknesses (Specimen B and D) is similar (-0.6 V_{SHE}). At current densities greater than 3 x 10^{-6} A/cm^2, a significant potential drop

Table 5-5

RESULTS OF CORROSION POTENTIAL MEASUREMENTS AT 290°C
FOR SAMPLES A1 AND A2

Concentration of Impurities in the water			Corrosion Potential of Zircaloy-4, mV with reference to SHE.	
Li (ppm)	B (ppm)	O_2 (ppm)	Sample A1**	Sample A2**
-	-	(<0.01)*	-480	-480
-	-	8	+200	+180
6	-	8	+ 30	+ 20
6	2200	8	+110	+ 90
6	2200	(<0.01)*	-310	-320

* Value in ( ) based on experience with additions of excess amounts of hydrazine. All others calculated.

** Duplicate Samples

Table 5-6

RESULTS OF CORROSION POTENTIAL MEASUREMENTS AT 290°C
FOR SAMPLES A, B AND C

Concentration of Impurities in the water							Corrosion Potential of Zircaloy, mV with reference to SHE		
B ppm	Li ppm	O_2 ppb	Fe^{3+} ppm	Fe^{2+} ppm	Cr^{6+} ppm	Cr^{3+} ppm	Sample A	Sample B	Sample C
600	1.5	(<10)*	-	-	-	-	-620	-600	-610
600	1.5	(<10)	-	-	-	-	-620	-600	-610
600	1.5	(<10)	-	-	-	-	-610	-590	-590
600	1.5	(<10)	0.073	0.024	-	-	-520	-590	-560
600	1.5	(<10)	0.023	0.059	-	-	-510	-540	-550
600	1.5	(<10)	-	63	-	-	-430	-440	-410
600	1.5	(<10)	-	56	-	-	-400	-420	-390
600	1.5	(<10)	20	20	-	-	-400	-410	-400
600	1.5	(<10)	-	-	-	-	-610	-500	-580
600	1.5	(<10)	-	-	<0.005	<0.005	-550	-520	-540
600	1.5	(<10)	-	-	<0.005	0.020	-570	-540	-560
600	1.5	(<10)	-	-	<0.005	0.050	-580	-570	-580
600	1.5	(<10)	-	-	<0.005	0.060	-480	-480	-480
600	1.5	(<10)	-	-	<0.005	0.080	-320	-280	-280
600	1.5	(<10)	-	-	13	33	+180	+290	+290
600	1.5	(<10)	-	-	6.9	16.8	+180	+280	+280
600	1.5	(<10)	-	-	3.0	8.7	- 10	+260	+270
600	1.5	(<10)	-	-	0.125	5.87	-380	-300	-310
600	1.5	(<10)	-	-	<0.005	<0.005	-470	-450	-460

* Value in ( ) estimated based on experience with additions of excess amounts of hydrazine. All others measured.

Table 5-7

RESULTS OF CORROSION-POTENTIAL-MEASUREMENTS at 290°C
FOR PLATINUM AND ZIRCALOY B AND D SAMPLES

Concentration of Impurities in the water							Corrosion Potential mV with reference to SHE		
B ppm	Li ppm	O_2 ppb	N_2H_4 ppm	NO_3^- ppm	SO_4^- ppm	SO_3^- ppm	Platinum	Zircaloy Sample D	Zircaloy Sample B
600	1.5	200	-	-	-	-	- 40	- 30	- 30
600	1.5	200	-	-	-	-	0	-360	- 60
600	1.5	50	-	-	-	-	-400	-520	-280
600	1.5	(<10)*	-	-	-	-	-560	-580	-580
600	1.5	(<10)	0.073	3.77	-	-	-430	-450	-360
600	1.5	(<10)	0.019	7.80	-	-	-440	-370	-300
600	1.5	(<10)	<0.010	9.10	-	-	-210	-370	-230
600	1.5	100	<0.010	8.45	-	-	-140	- 60	+ 60
600	1.5	(<10)	-	37.6	-	-	-	-	- 30
600	1.5	(<10)	-	72.3	-	-	-	-	+100
600	1.5	(<10)	-	85.3	-	-	+ 80	-	+140
600	1.5	(<10)	-	97.8	-	-	+ 80	+100	+190
600	1.5	(<10)	-	-	-	-	-	-	-630
600	1.5	(<10)	-	-	-	-	-	-	-560
600	1.5	(<10)	-	-	8.77	9.1	-540	-	-540
600	1.5	(<10)	-	-	51.6	50.5	-470	-440	-480
600	1.5	(<10)	-	-	66.1	64.6	-460	-440	-470
600	1.5	(<10)	-	-	73.3	70.7	-450	-430	-460

*Value in ( ) estimated based on experience with additions of excess amounts of hydrazine. All others measured.

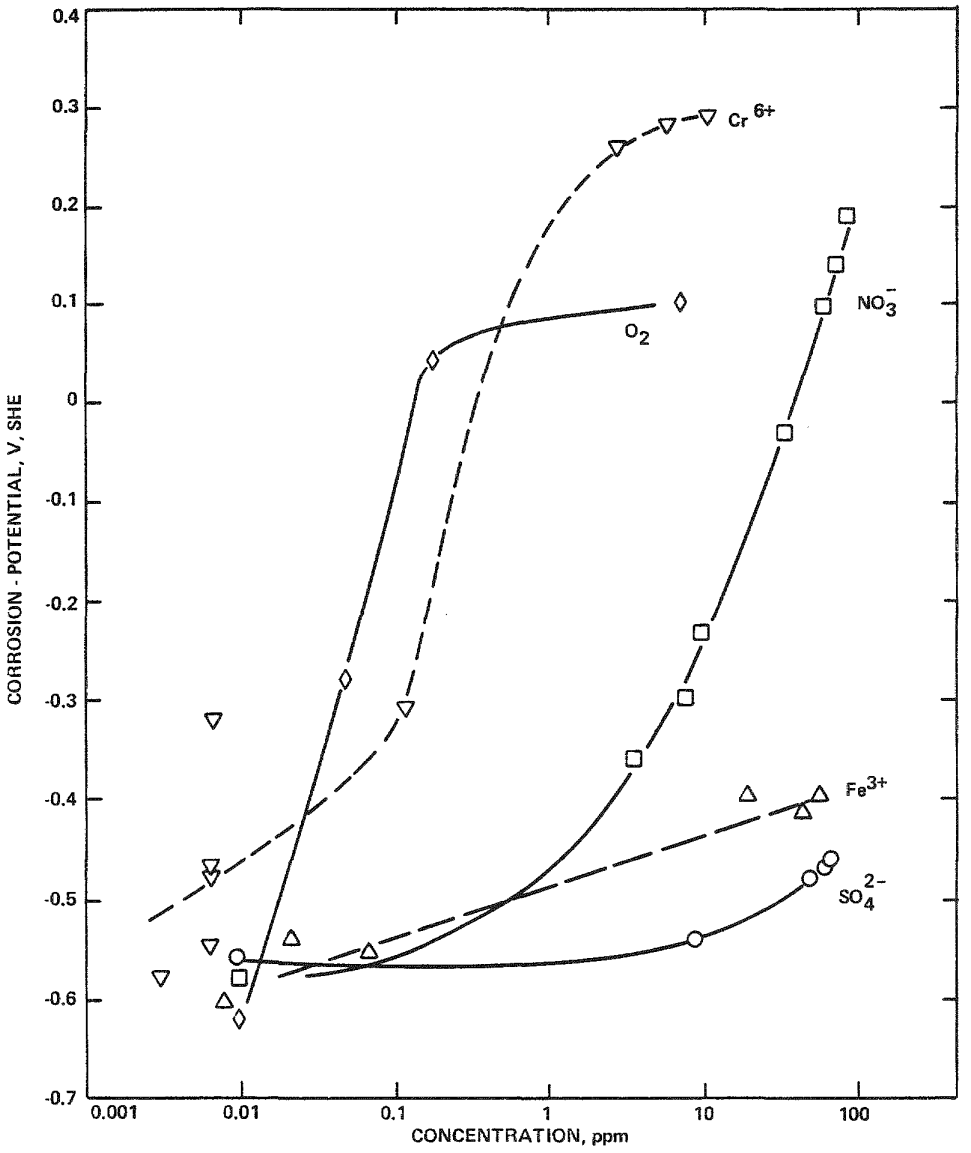

Figure 5-2. Influence of Various Impurities on the Corrosion Potential of Oxidized Zircaloy in Pressurized Water (1.5 ppm Li, 600 ppm B) at 290°C

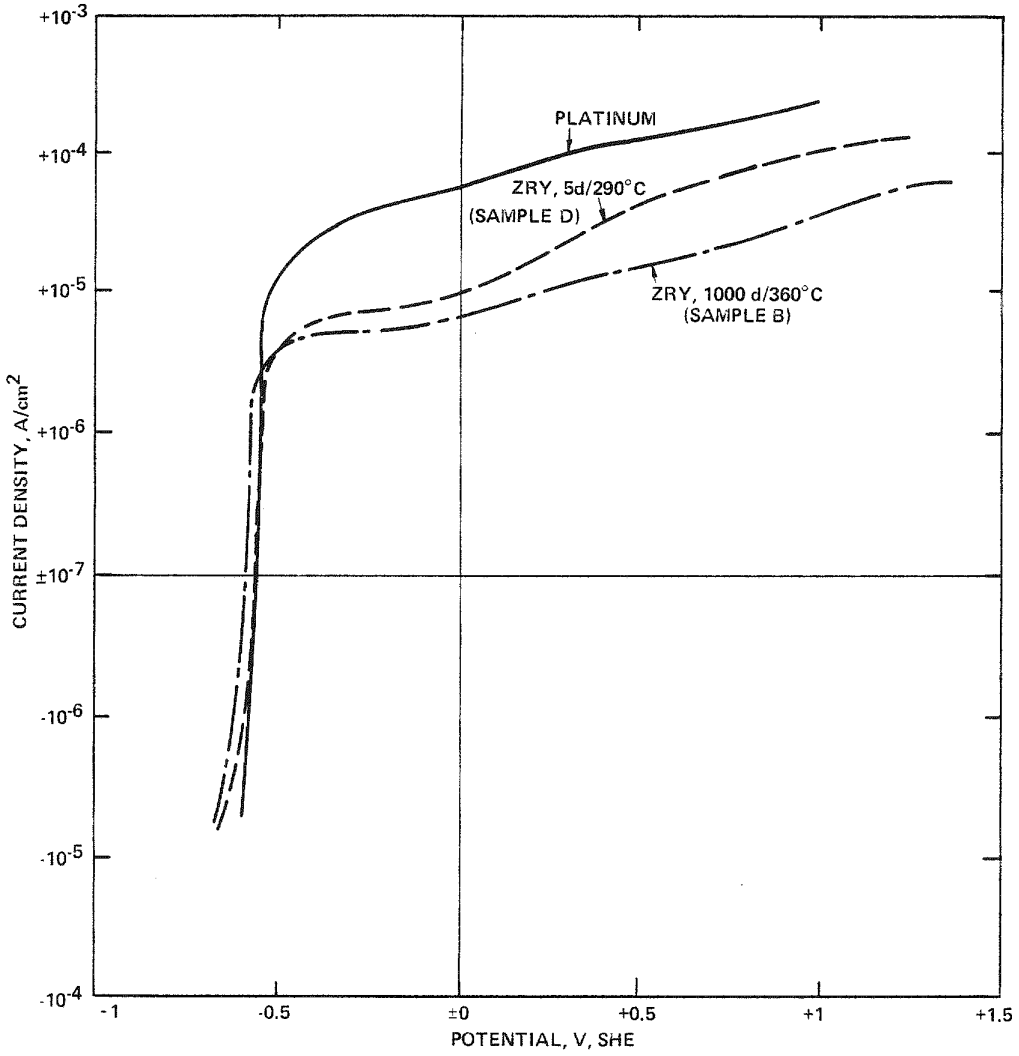

Figure 5-3. Comparison of the Polarization Behavior of Oxidized Zircaloy and Platinum at 290°C in Pressurized Water (1.5 ppm Li, 600 ppm B and < 10 ppb O_2)

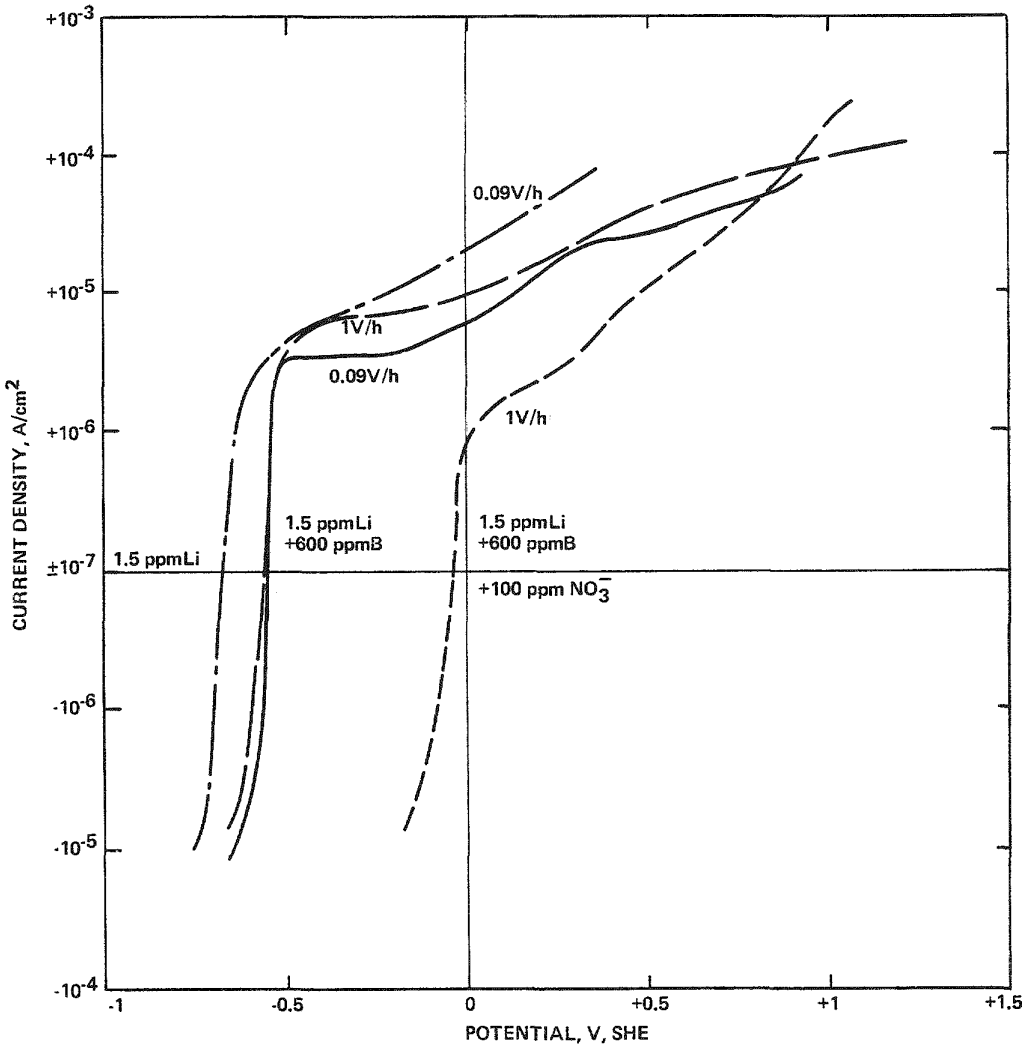

Figure 5-4. Influence of Various Impurities in 200°C Water on the Polarization Behavior of Zircaloy Sample D Pre-oxidized at 290°C for 750 Days

occurs in all three cases. In Figure 5.4, a change in the polarization rate from 0.09 V/h to 1.0V/h has a negligible effect on the anodic polarization curve. Additions of oxidizing species such as NO_3^- to the PWR water chemistry (600 ppm B, 1.5 ppm Li) affects the polarization behavior mainly with respect to the corrosion potential and to a lesser degree the polarization behavior at high potentials.

Measurements in water with only 1.5 ppm Li without any B addition show a lower corrosion potential due to the increasing pH value and a slight deviation in the polarization behavior at potentials between -0.5 and 0 V_{SHE}.

Influence of Impurities on Corrosion

The results of mini-autoclave corrosion tests at 350°C are summarized in Table 5.8. Recrystallized Zircaloy corrosion specimens showed longer transition times and/or lower post transition corrosion rates than stress-relief annealed specimens. Compared to the distilled water environment, the water with PWR chemistry (600 ppm B, 1.5 ppm Li) showed slightly longer transition times or lower post-transition corrosion rates. Addition of the following individual impurities to the water of PWR chemistry (600 ppm B + 1.5 ppm Li) did not influence the corrosion of Zircaloy: 1 ppm Fe added as a sulfate; 0.5 ppm Cr added as a sulfate; Fe_3O_4; 100 ppm of $Fe_2(NO_3)_3$ and anion resin. The following additions slightly increased corrosion (a decrease in time to transition and/or increase in the post transition corrosion rate): 10 to 100 ppm Fe; 5 to 50 ppm Cr; 10 ppm Ag; 10 ppm Cu; Cr_2O_3; $NiFe_2O_3$; NiO; mixed oxides; 100 ppm Fe + Fe_3O_4; 100 ppm Fe + mixed oxides; 50 ppm Cr + Fe_3O_4; 50 ppm Cr + mixed oxides. In these latter tests the mixed oxides consist of a mixture of 16.8 wt % Fe_3O_4, 4 wt % NiO and 2 wt % Cr_2O_3.

However, for the above cases, the increase in the post-transition corrosion rate or the decrease in transition time is within the experimental measurement accuracy. Therefore no pronounced effect of these additions on Zircaloy corrosion could be demonstrated. The addition of cation resin or 100 ppm $FeCl_3$, however, had an effect on Zircaloy corrosion that was greater than the experimental measurement uncertainty. These additions increase the post-transition corrosion rate and decrease the time to transition.

Table 5-8

INFLUENCE OF IMPURITIES ON OUT-OF-PILE CORROSION AT 350°C IN MINI-AUTOCLAVES

Test Environment		Lot A, Stress-Relief Annealed Zircaloy			Lot B, Recrystallized Zircaloy	
Type	Form	Max. Exposure Time (d)	Time to Transition (d)	Post Transition Rate (mg/dm^2d)	Time to Transition (d)	Post Transition Rate (mg/dm^2d)
Distilled water		200	~100	0.46	~150	0.34
PWR-water	(600 ppm B + 1.5 ppm Li)	200	~100	0.39	~170	
PWR+ 1ppm Fe	50% Fe^{2+}	200	~100	0.41	~160	0.32
PWR+ 10ppm Fe	+ 50% Fe^{3+}	150	~ 50	0.45	~150	
PWR+100ppm Fe	as the Sulfate	150	~ 80	0.40	~150	
PWR+ 0.05ppm Cr	50% Cr^{3+}	200	~100	0.40	~170	
PWR+ 0.5 ppm Cr	+ 50% Cr^{6+}	200	~100	0.34	~170	
PWR+ 5 ppm Cr	as the Sulfate	150	~ 80	0.36	~130	
PWR+50 ppm Cr	and Chromate	150	~ 60	0.32	~120	
PWR+10ppm Ag	50% Ag^{+} + 50% Ag^{2+} as the Nitrate	150	~ 80	0.36	~130	
PWR+10ppm Cu	50% Cu^{+} + 50% Cu^{2+} as the Sulfate	150	~ 80	0.42	~130	

Table 5-8 (Continued)

INFLUENCE OF IMPURITIES ON OUT-OF-PILE CORROSION AT 350°C IN MINI-AUTOCLAVES

Test Environment		Lot A, Stress-Relief Annealed Zircaloy			Lot B, Recrystallized Zircaloy	
Type	Form	Max. Exposure Time (d)	Time to Transition (d)	Post Transition Rate ($mg/dm^2 d$)	Time to Transition (d)	Post Transition Rate ($mg/dm^2 d$)
PWR + 23 wt % Fe_3O_4		200	~120	0.39	~170	
PWR + 23 wt % Cr_2O_3		150	~120	0.57	~140	
PWR + 23 wt % $NiFe_2O_3$		200	~ 90	0.44	~150	0.35
PWR + 23 wt % NiO		200	~ 70	0.42	~130	0.37
PWR + 23 wt % Mixed Oxides*		150	~ 70	0.45	~130	
PWR+100ppm Fe+Fe_3O_4		140	~100	0.41	~140	
PWR+100ppm Fe+Mixed Oxide*		150	~ 70	0.30	~130	
PWR+50ppm Cr+Fe_3O_4		150	~ 60		~140	
PWR+50ppm Cr+Mixed Oxides*		150	~ 60		~120	
PWR + 23 wt % Anion resin		200	100	0.41	170	
PWR + 23 wt % Cation resin		200	< 50	0.50	100	0.50
PWR + 100ppm $Fe_2(NO_3)_3$		150	100	0.39	130	
PWR + 100ppm $FeCl_3$		150	60	0.52	106	0.50

* Mixed oxide composition 0.37 wt % Fe_3O_4 + 0.4 wt % NiO + 0.02 wt % Cr_2O_3

Primary Coolant Chemistry

Primary coolant chemistry data for different cycles of six KWU reactors were compiled and are presented in Table 2-4.

The electrical conductivity, pH, and the concentrations of lithium, oxygen, and chloride ions are measured on a daily to weekly basis. Hydrogen is typically determined on a weekly basis, whereas ammonia and iron are only measured a few times during a cycle. The concentration of nitrates was measured in cycles 2, 3 and 4 of Reactor E only. With the exception of Cycle 2 of Reactor A, the water chemistry of all other cycles of different reactors was similar. In Reactor E, Cycles 2 to 4, the lithium content was intentionally reduced to values in the range of 0.7 to 1.0 ppm in order to obtain information on the possible influence of lithium concentration on clad corrosion. Cycle 2 of Reactor A was operated without lithium additions. Cycles 4 and 5 of Reactor A and Cycle 1 of Reactor D were operated with relatively low lithium concentrations over longer periods. With the exception of Cycle 5 of Reactor A, the iron concentration in the coolant ranged between <5 and 100 ppb. A somewhat higher iron concentration (up to 150 ppb) was measured at the end of Cycle 5 in Reactor A during a stretchout operation with high lithium concentration (about 1 ppm) and high pH (9) in the first part of Cycle 5 and a low lithium concentration (<0.1 ppm) in the later part of Cycle 5. Relatively high concentrations of nitrate (10 to 200 ppb) were measured in Cycle 4 of Reactor E. Generally, high concentrations of nitrate were associated with high concentrations of ammonia as can be seen from Table 2-4.

Special Measurements of Impurities in the Reactor Coolant

Special measurements of the concentrations of Fe, Ni, Cr, Cr^{6+}, NH_3 and NO_3^- in the coolant of Reactors A and E were conducted in October 1981 and March 1982. The results are presented in Table 5.9. For comparison, results of earlier routine measurements are also listed. Because of the availability of the high pressure filtration technique, the total individual element content from March 1982 could be subdivided into the categories of crud particles, cations and anions in solution. The earlier routinely measured values are higher than the special analysis values. The reasons for these differences are the time, volume and method of sampling. The routinely measured values were based on samples taken out after power shutdowns and power changes. In such periods higher impurity levels are normal. The other difference is that the routine analysis was based on a 1 liter

Table 5-9

IMPURITY CONCENTRATIONS IN THE PRIMARY COOLANT OF PWR-A AND E

Reactor	Species	Routine Analysis (later cycles) ppb	Special Analysis October 1981 ppb	Special Analysis, March 1982 (1) Particles %	(2) Cations* %	Total of (1) & (2) %	(3) Anions %	Total ppb (1+2+3)
A	Fe	< 5 - 50	-	-	-	86	14	1.9 - 2.4
	Ni	<10 - 30	-	-	-	100	0	0.2 - 0.6
	Cr	< 5 - 20	1.4	-	-	100	0**	0.09 - 0.11
	Cr^{+6}	-	<0.5	-	-	-	-	-
	NH_3	-	0.46	-	-	-	-	-
	NO_3	-	<4	-	-	-	-	-
E	Fe	< 5 - 40	-	59	31	90	10	0.7 - 1.3
	Ni	<10 - 15	-	50	30	80	20	0.03 - 0.14
	Cr	< 2 - 16	2.5	44	22	66	33**	0.12 - 0.24
	Cr^{+6}	-	<0.5	-	-	-	-	-
	NH_3	-	0.38	-	-	-	-	-
	NO_3	< 5 - 200	<4***	-	-	-	-	-

* M^+

** CrO_4^-

*** NO_3^-

volume static sample whereas the special analysis was based on a 100-400 liter dynamic sample.

The limited sample volume and static sampling may promote deposition of oxide particles on the walls of the sampling tank and in the valve connected to the sampling tank, resulting in higher measured impurity concentrations. The results from the special measurement in March 1982 are based on dynamic sampling of larger volumes (100 to 400 liters) of water and therefore are to be considered more accurate. However, the high pressure filtration technique has not yet been used to sample PWR primary coolant water in reactors other than those listed in Table 5.9.

According to the results of the March 1982 special analysis, listed in Table 5.9, the concentration of iron in the coolant at steady state operation is between 0.7 to 2.4 ppb for the two plants listed. The concentration of nickel is higher (0.2 to 0.6 ppb) in plant A where a nickel-base alloy (Inconel 600) is used for the steam generator tubes compared to Plant E (0.03 to 0.15 ppb) where an iron-base alloy (Incoloy 800) is used. The concentration of chromium in the coolant is very low (0.1 to 0.25 ppb) in both plants.

The solid oxide particles of the circulating crud were collected by the high pressure filtration technique in March 1982. The particle size of the filtered solids was greater than 0.1 μm. For reactor E coolant, the impurity concentration of solid particles accounted for almost half of the total impurity concentration in the coolant (Table 5.9). The chemical composition of the solid filtrate was obtained by energy dispersive X-ray analysis. The results are presented in Table 5.10. The major constituents of the crud were Zr, Fe, Ni and Cr for Reactor A and Fe, Cr, Ni for Reactor E. X-ray diffraction analysis was used to identify the phases in the crud and the results are presented in Table 5.10.

Monoclinic ZrO_2 and intermetallic α phase (Fe, Ni, Cr) were identified as phases in crud from Reactor A. Most of the diffraction lines from the samples from PWR-E were identified as those of a $(Fe, Ni, Cr)_3 O_4$ spinel.

An examination of the crud particles under SEM showed differences in the particle shapes for samples from Reactor A and E (Fig. 5.5). Crud particles from Reactor E appeared to be less porous (Fig. 5.5.a) compared to those from Reactor A (Fig. 5.5.b).

Table 5-10

X-RAY DIFFRACTION AND EDMA-ANALYSIS
OF CIRCULATING CRUD FROM REACTOR A AND E

Reactor	Phase Identified	Chemical Composition
A	st: ZrO_2 monocl.	st: Zr, Fe, Cr, Ni
	m : α-(FeNiCr),	w : Ti, Sn, Pb
E	st: $(FeNiCr)_3O_4$ (a_o = 8.35Å)	st: Fe, Cr, Ni
		w : Ti, Zr

st = strong
m = Medium
w = weak

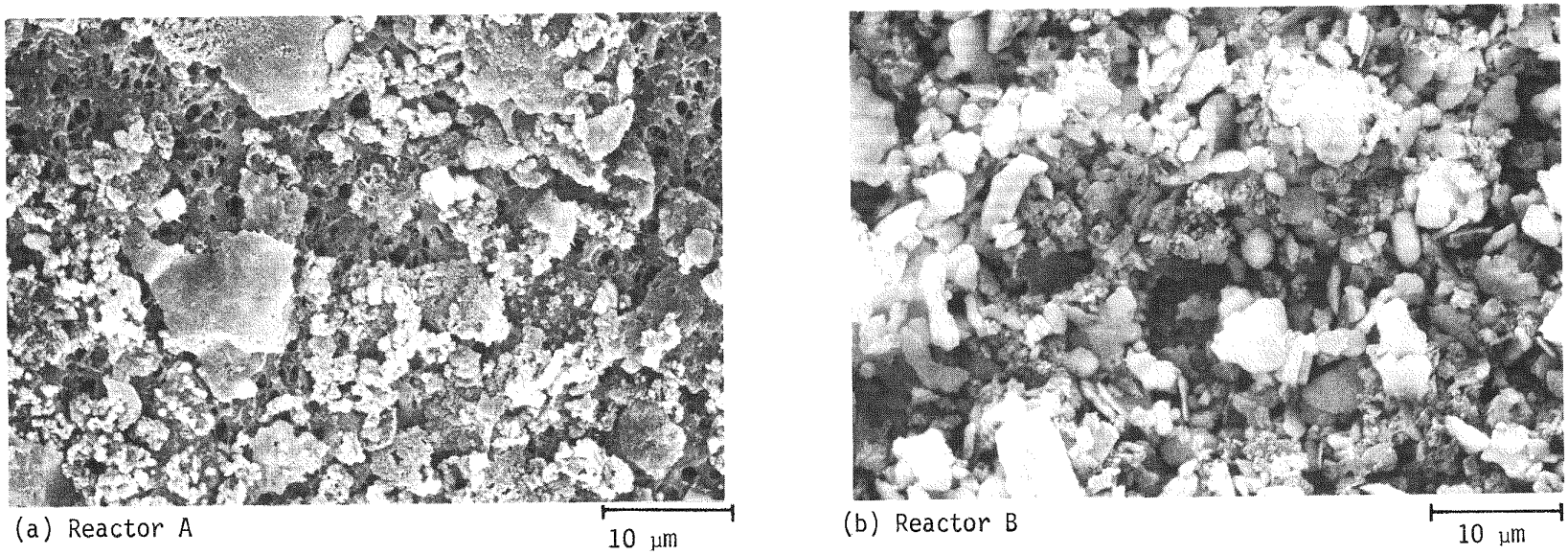

Figure 5-5 SEM Examination of Crud Formed in Reactors A and E Illustrating the Differences in Porosity

An analysis of the anion resin papers in March 1982 from Reactor A revealed only iron, (Table 5.9) whereas for Reactor E, iron, nickel and chromium (probably in the form of the chromate) were detected. Based on the March 82 results the estimated chromate concentration in the Reactor E coolant, is about 0.1 ppb. Chromates were not detected in the coolant of Reactor E in the October 81 measurements, possibly due to the higher detection limit at that time. The presence of NO_3^- is another indication of oxidizing conditions. The concentration of NO_3^- ions was measured in the coolant of Reactors A and E in October 1981. A quantitative determination of the NO_3^- concentration in the coolant of Reactor A was possible. However, for Reactor E coolant such determination was not possible due to the low concentration levels.

DISCUSSION OF COOLANT CHEMISTRY EFFECTS

Coolant chemistry may be partially responsible for the observed enhancement of cladding corrosion in PWRs. The coolant chemistry contribution may arise due to 1) variations in the electrochemical corrosion potential, 2) different radiolytic species and 3) impurities in the coolant. The influence of corrosion potential on the corrosion rate of passivated metals is not as well known as its influence on the electrochemical dissolution at active surfaces which increases exponentially with the potential. The corrosion rate of passivated metals, although slower than that of the metals with active surfaces, is also expected to increase with potential.

The electrochemical measurements performed in this investigation reveal a strong influence of concentration of oxygen, chromate and NO_3^- ions on the corrosion potential. However, the concentration levels necessary to increase the corrosion potential are much larger than the measured concentration levels in the coolant of several PWRs. Therefore, with the exception of oxygen, the observed in-reactor enhancement of corrosion cannot be explained on the basis of the actual impurity concentration levels observed in the coolant of reactors where oxide thickness measurements were obtained. Although the concentration level is low, detection of NO_3^- in the coolant of Reactor E implies that even in the presence of a hydrogen overpressure, very mild oxidizing conditions may exist in part of the core.

In modern PWRs, a hydrogen overpressure is used to suppress the formation of oxidizing radicals due to radiolysis of water. Subcooled boiling, however, may strip the hydrogen from the water phase by transferring it to the steam bubbles. No

subcooled boiling is predicted during the normal operations of Cycles 2 to 4 of Reactor A and of all cycles of Reactors C and D. For later cycles of Reactor A, as well as for all cycles of Reactors E and F, a small fraction (0.5 to 1.5%) of the fuel rod surface is expected to be in subcooled boiling. A clear correlation between the degree of subcooled boiling and corrosion enhancement is not observed in any of the reactors investigated. These results indicate that small amounts of subcooled boiling do not have a significant effect on the in-reactor corrosion behavior of Zircaloy in PWRs operated with a hydrogen overpressure.

Another possible reason for the observed variations in the corrosion enhancement could be the presence of impurities (or additions) in the coolant and their incorporation into the oxide layer. The chemical, microprobe, SIMS and IMA results reported in Section 4 indicate very negligible local concentration of Li or other impurities in the oxide. The observed Li concentration in the oxide is significantly lower than that necessary to account for the observed enhancement according to the model of Hillner and Chirigos (3).

Some information regarding the effect of lithium on the in-reactor corrosion enhancement can be derived by comparing the corrosion rate during different cycles of Reactor E. The first cycle of Reactor E was operated at a lithium level of 1.5 ppm and was reduced to 0.85 ppm for subsequent cycles. The derived corrosion enhancement factors for Cycle 1 and subsequent cycles of Reactor E were, however, practically identical. Thus the results of the present program do not support the postulate that lithium may be responsible for the observed in-reactor corrosion enhancement.

SIMS results show higher concentrations of Fe and Cr at the oxide/water interface, which are probably indicative of the presence of crud. The corrosion tests performed on Zircaloy surfaces with a deposit of synthetic crud show that various oxides, which may deposit on fuel rods during in-reactor exposure, can cause slight enhancement of the corrosion rate. The X-ray analysis of crud samples from PWR-A failed to identify an (Fe Cr, Ni) oxide. The crud sample from PWR-E was mainly a $(Fe\ Ni\ Cr)_3\ O_4$ spinel that is quite similar to $NiFe_2O_4$ spinel which was found to cause a slight enhancement of corrosion rate out of pile. Thus some of the slight enhancement of in-reactor corrosion of Zircaloy may be due to the thin crud deposit film on the fuel rods.

Although the presence of cation resins can enhance Zircaloy corrosion, the conductivity of coolants from PWRs A to F do not suggest that they are present in significant concentrations. Chlorides and fluorides can enhance corrosion of Zircaloy. However, the actual concentration levels measured in the PWR coolant are well below the concentrations necessary to cause the corrosion enhancement.

CONCLUSIONS

Summarizing, the electrochemical measurements show that some impurities in coolant, for example O^{2-}, Cr^{6+} and NO_3^- can have a strong influence on corrosion potential and therefore the corrosion rate of Zircaloy in water at 350°C. However, the actual concentration levels of these impurities are too low to cause accelerated corrosion. Therefore the in-reactor corrosion enhancement cannot be explained on the basis of the coolant chemistry effects in the bulk coolant.

REFERENCES

1. Solomon, Y., Proc British Nuclear Society, "Water Chemistry of Nuclear Reactor Systems", London, 1978, pp 101.

2. Garzarolli, F., et al. IAEA Specialist Meeting on the Influence of Power Reactor Water Chemistry on Fuel Cladding Reliability, San Miniato, Italy, 1981.

3. Hillner, E. and Chirigos, J. N., "The Effect of Lithium Hydroxide and Related Solutions on the Corrosion Rate of Zircaloy in 680°F Water", WAPD-TM-307, 1962.

4. J. Hickling and N. Wieling, "Electrochemical Investigations of the Resistance of Inconel 600, Incoloy 800 and Type 347 Stainless Steel to Pitting Corrosion in Faulted PWR Secondary Water at 150 - 250°C". Corrosion (NACE) Volume 37 No. 3, March 1981, pp 147-152.

Section 6

THERMAL-HYDRAULIC CALCULATIONS

INTRODUCTION

In reference (1), the clad surface temperature under non-boiling heat transfer conditions was calculated assuming that the heat transfer coefficient (α) from the coolant to the clad does not vary with axial position. However, as discussed in Section 3, the axial profiles of the oxide layer thickness on PWR fuel rods have a "sawtooth" shape, with reduced corrosion layers at and just above the spacer grid positions. Figure 3.7 shows a typical oxide layer thickness profile. The corrosion layer thickness also varies around the rod circumference. The purpose of this section is to evaluate some of the thermal hydraulic factors that could contribute to these axial and circumferential variations in oxide layer thickness. Some of these analyses have already been reported in detail (2).

SURVEY OF CORRELATIONS FOR FULLY DEVELOPED FLOW

One of the most important parameters controlling Zircaloy corrosion in a normal PWR environment is the temperature at the metal/oxide interface. In the presence of a heat flux, several factors influence the metal/oxide interface temperature, one of which is the heat transfer coefficient between the coolant and the fuel rod surface.

The heat transfer coefficient is calculated from:

$$\alpha = NuK/d_H \qquad 6\text{-}1$$

where α = heat transfer coefficient between coolant and cladding, $W/cm^2.K$

Nu = Nusselt number
K = coolant thermal conductivity, W/cm.K
d_H = hydraulic diameter, cm

Of the parameters used to calculate α, both the hydraulic diameter (d_H) and the Nusselt number (Nu_∞) may vary within a spacer grid and along an undisturbed section of fuel rod. Flow entrance effects and thermal entrance effects may influence the Nusselt number for distances from 5 to 50 hydraulic diameters from the flow entrance (spacer grid). Beyond this distance, the flow will be fully developed and the average Nusselt number will approach a constant value which is defined as Nu_∞ .

Some of the correlations for the Nusselt number under conditions of fully developed flow (Nu_∞) are listed in Table 6.1; these were empirically derived from measurements made in single tube experiments. The heat transfer characteristics of a fuel rod located within a rod bundle may be different.

Measurements were conducted of heat transfer coefficients within bundles of rods with square (3, 4) and triangular (3 to 14) lattices. Reviews of these data (5, 15) indicate that the pitch-to-diameter ratio will influence the Nusselt number, although the extent will vary depending on the bundle geometry (square versus triangular). Weisman (16) showed that all these data can be explained with a single correlation if the results are evaluated as a function of, "ε", which is the ratio of the coolant flow area to the total cross sectional area of the unit cell of an infinite lattice. In Figure 6.1, the data from reference (5) are plotted as a function of ε. At the value of ε applicable to KWU Reactors A-F, the Nu_∞ value for rod arrays is 1.0 to 1.4 times that of the single tube (as defined by reference 16). While in single tubes the Nu-number is constant over the circumference, a circumferential variation in ε (which depends on the pitch to diameter ratio) will be observed in rod bundles. Again, for illustration, with the pitch-to-diameter ratio appropriate to KWU Reactors A-F, reference (5) indicates that a circumferential variation of α of $\pm$ 10% can be expected.

A sample calculation was performed to analyze the thermal-hydraulic behavior of a fuel assembly of the type in KWU Reactor A. The analysis considered a hypothetical fuel rod with a linear heat generation rate of 200 W/cm and addressed the portion of the rod in and between the sixth and seventh spacer grids. Table 6-1 lists the heat transfer coefficients, α, calculated by using the various single tube correlations presented in Table 6.2. Also given in Table 6.1 are the upper and lower values of α_∞ which have been inferred from measurements on bundles using the ratio applicable to Reactor A (Figure 6.1). The value 2.41 $W/cm^2.K$ for α_∞, which was used initially (1) for KWU Reactor A, is well bounded by the values presented in Table 6.1.

Table 6-1

CALCULATED HEAT TRANSFER COEFFICIENTS FOR KWU REACTOR A

Type of Correlation	Developed from	Heat Transfer Coefficient ($W/cm^2.K$)	
		Between Grids 6 & 7	In Grid 7
Single Rod	Dittus and Boelter (23)	2.50	3.60
	Colburn (24)	2.51	3.61
	Hausen (25)	2.10	3.15
	Michejev (16)	2.27	3.28
	Friend and Metzner (26)	2.09	3.13
Rod Bundles (Fig. 6-1)	Lower bound	2.27	3.28
	Mean	2.76	3.48
	Upper bound	3.25	4.68

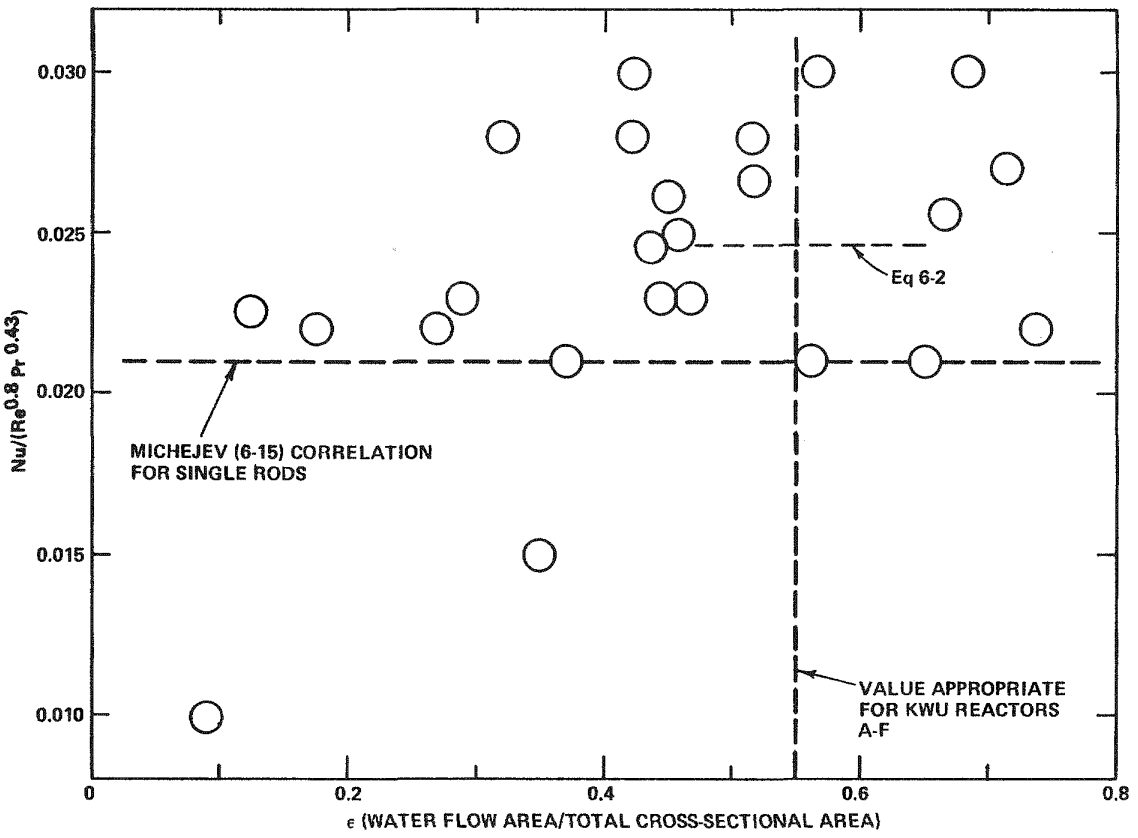

Figure 6-1. Influence of Water Flow Area to Total Cross-Sectional Area on Heat Transfer Characteristics of Tube Bundles

Table 6-2

SUMMARY OF NUSSELT NUMBER CORRELATIONS
FOR FULLY DEVELOPED FLOW CONDITIONS (Nu)

Source	Correlation Nu =	Limits of Applicability	
		Pr**	Re***
Dittus and Boelter* (23)	$0.023\ Re^{0.8}Pr^{0.4}$	-	10^4-10^6
Colburn (24)	$0.023\ Re^{0.8}Pr^{1/3}$	-	-
Hausen (25)	$0.037(Re^{0.75}-180)Pr^{1/3}(\ F/\ W)^{0.14}$	-	-
Michejev (16)	$0.021\ Re^{0.8}Pr^{0.43}$	0.6-2500	10^4-$5x10^6$
Friend and Metzner (26)	$0.037(Re^{0.75}-180)Pr^{0.42}(\ F/\ W)^{0.14}$	0.46-346	10^4

* Often used in the nuclear industry
** Pr - Prandtl number
*** Re - Reynolds number
F Viscosity of film
W Viscosity of bulk coolant

The following correlation best describes the bundle measurements appropriate to the KWU fuel assembly.

$$Nu = 0.025\ Re^{0.8} Pr^{0.43} \qquad 6\text{-}2$$

where

Pr = Prandtl numbers
Re = Reynolds numbers

INFLUENCE OF SPACER GRIDS

Each spacer grid causes hydraulic disturbances and local turbulence and serves to reduce temperature gradients within the coolant channel. For these reasons, hydraulic and thermal effects similar to entrance effects for single tubes may occur at and above the spacer grid positions. According to Grass (16), a correlation of the following form can be used to relate the local heat transfer coefficient, α_x, to the fully developed values, α_∞, in the region downstream of the disturbance:

$$\alpha_x = \alpha_\infty [1 + c/(x/d)] \qquad 6\text{-}3$$

where

α_x = local heat transfer coefficient, W/cm^2-K,
α_∞ = fully developed heat transfer coefficient, W/cm^2-K,
c = constant,
x = distance from point at upstream edge of spacer grid, cm,
d = hydraulic diameter, cm.

For single tubes, the constant c depends on the particular geometry of the fuel assembly at the inlet and was found to vary between 0.4 and 5.8 (16).

Very few measurements of entrance effects in rod bundles have been reported. The flow channel entrance effect in rod bundles depends on the geometry of the end of the fuel rod (5) and was found to be low in magnitude (c in Eq. 6.5 was found to be $0.2>c>0.4$ for a Reynolds number of more than 10^5 when the hydraulic diameter is used for d instead of the tube diameter). A disturbance within the subchannel of a bundle may lead to greater flow distortions than the entrance effects in rod bundles (5). Thus for subchannel disturbances c is at least 0.4. Experiments conducted by Stiefel (18) on the influence of disturbance within the subchannel on flow

inhomogeneities indicate a possible maximum value for c of about 2.5. Thus c for spacer grids should range from 0.4 to 2.5.

Figure 6.2 shows a profile of oxide layer thickness in the region between Grids 6 and 7 of a fuel rod from Assembly 365 of Reactor A. The corrosion behavior along this length of rod was analyzed using the methodology and equation of Appendix B in reference (1). At several positions along the thickness profile, the α-value was inferred by comparison with the α-value assumed at the peak corrosion position. The resultant α-values are plotted in Figure 6-3 and are found to decrease with increasing distance from grid 6; α is a maximum within the spacer grid.

The ratios (α_x/α_∞) of the calculated α-values for the various axial positions are plotted as a function of distance in Figure 6.3. Also shown is the theoretical curve calculated from Eq. 6-3 with a c-value of 1.0. There is reasonable agreement with the data. Grass (17) found that Eq. 6-3 is appropriate for distances greater than $5d_H$; this application appears to fit the data for values of x down to $2d_H$. Assuming that Eq. 6-3 with c = 1.0 is valid, then at the maximum temperature position (which is ~35 cm or 25 d_H) above Spacer Grid 6 in KWU Reactor A, there is a small entrance effect of ~4%. The data in Figure 6.4, adjusted to reflect this effect, show good agreement with the theoretical curve for c = 1.0. Using this correlation, which is based on data from Reactor A, it was possible to predict the axial oxide profiles for rods from Reactor A and from other reactors. The measured and predicted oxide profiles for a four cycle rod from Reactor D are given in Figure 6.4.

INFLUENCE OF SUBCHANNEL GEOMETRY WITHIN THE FUEL ASSEMBLY

The different types of subchannels present in the KWU fuel assembly from Reactor A are illustrated in Figure 6.5. It can be seen that the subchannel size varies depending on the proximity of the fuel rod to other fuel rods, guide tubes or water gaps. Ideally the fuel rods can be subdivided into several categories, depending on the neighboring fuel rods and the neighboring subchannels.

- internal fuel rods with fuel rods as nearest neighbors, (Type 0),
- internal fuel rods with fuel rods and 1 or 2 guide tubes as nearest neighbors, (Types 1, 2 and 3)
- peripheral fuel rods (Types 4 and 5)

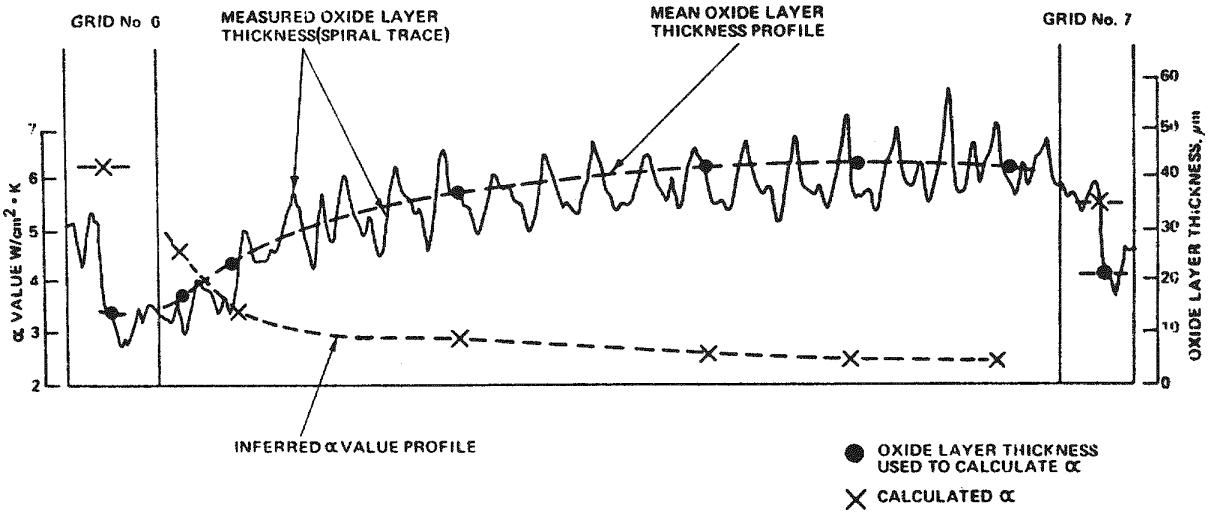

Figure 6-2. Oxide Layer Thickness Profile, Heat Transfer Coefficient Profile of Rod 365/41008, Reactor A

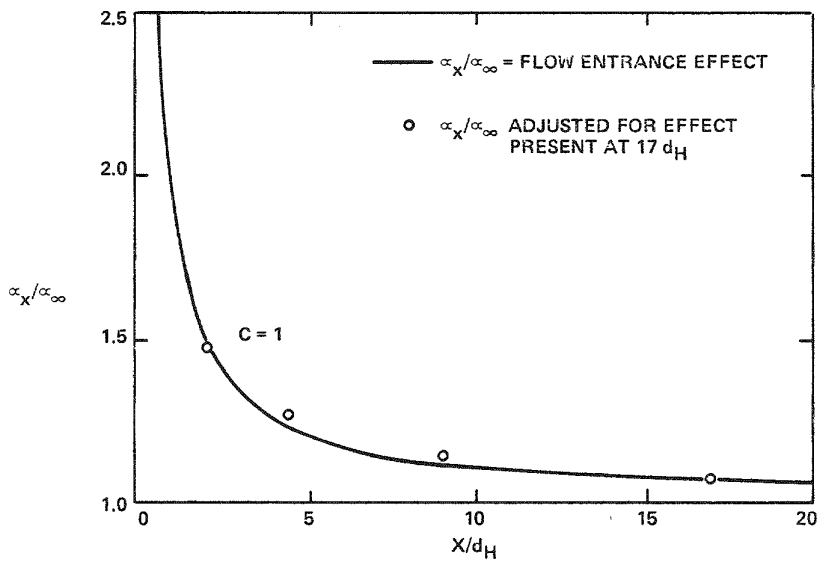

Figure 6-3. Comparison of Calculated Heat Transfer Coefficient with Empirical Correlations

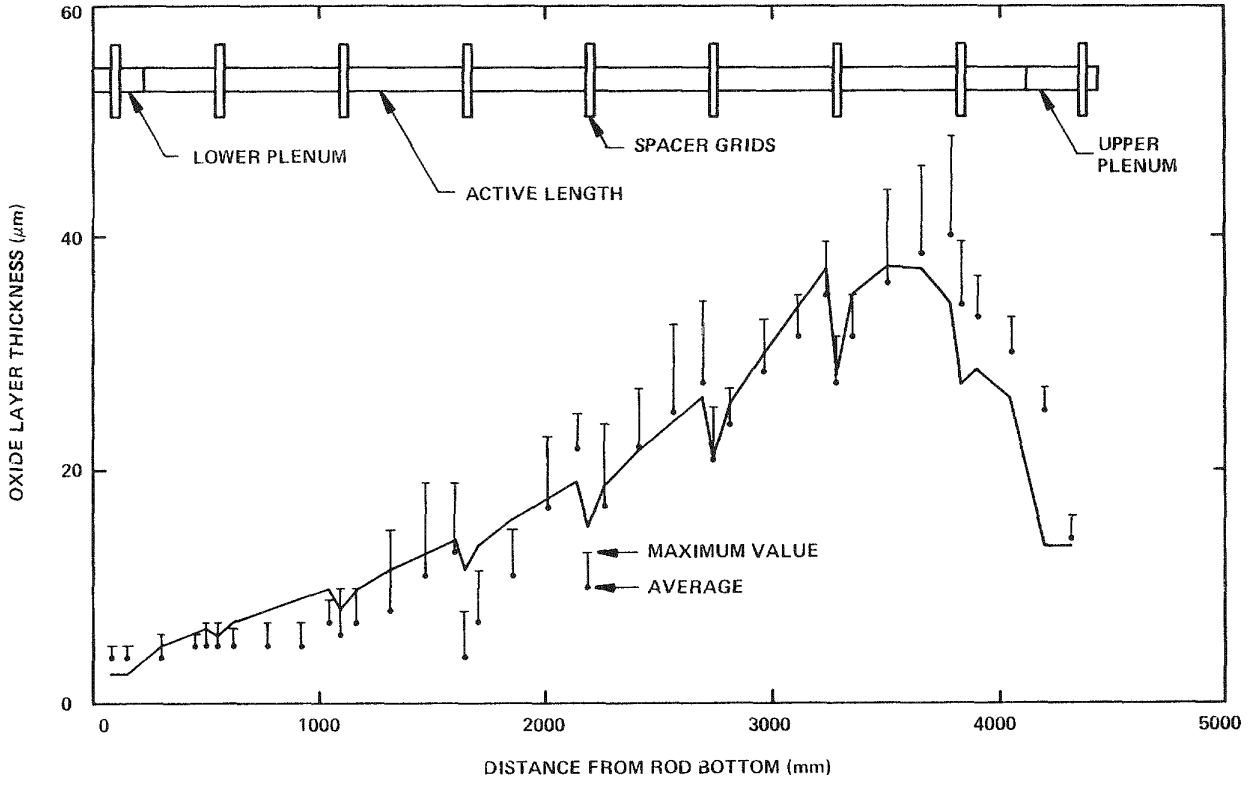

Figure 6-4. Comparison of Measured and Calculated Oxide Layer Thickness Profile for a 4 Cycle Rod from PWR-D

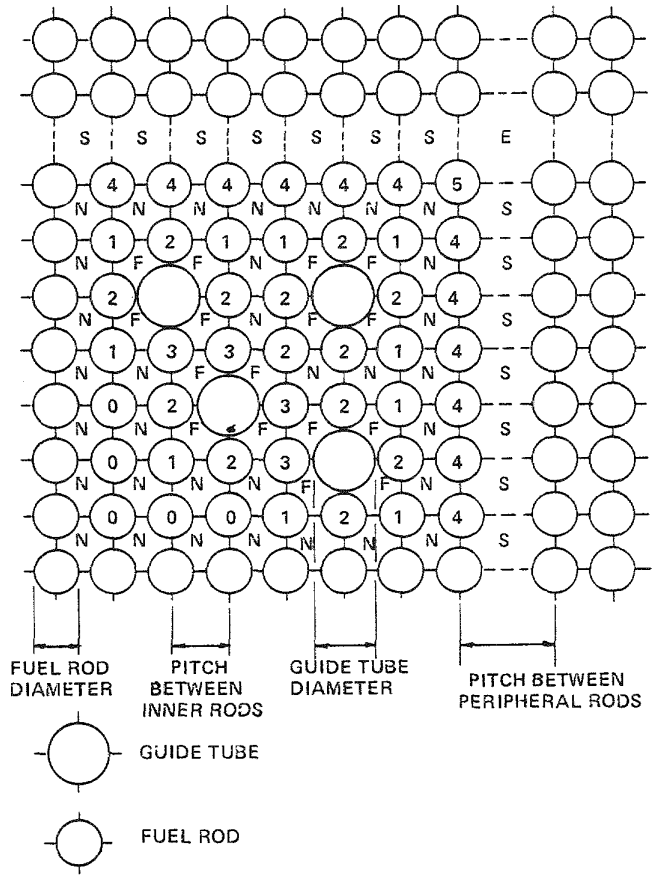

Figure 6-5. Differences in Sub-Channel Geometry Within the Core Illustrated with a One Quarter Fuel Assembly Schematic

In the case of oxide layer measurements made on peripheral fuel rods while they are still located in the bundle, the measurement is made at a circumferential position just opposite the water gap separating the two fuel assemblies. An additional rod type was developed to account for the local proximity of the fuel rod to the water gap between fuel assemblies and its effect on heat transfer. Because of their unique geometry the different subchannels will have differences in their associated flow areas and hydraulic diameters which might result in different specific coolant flow rates and heat transfer coefficients. Codes such as COBRA (19) can predict the differences in fuel and surface temperature due to such effects. However, the codes are complex and were not incorporated as a subroutine in the analysis of waterside corrosion data.

In order to assess the effect of variations in local flow on corrosion, an approximation (20) was developed relating the mass flow velocity to the hydraulic diameter.

$$G_i/G_{av} = (d_{hi}/d_{av})^{1/2} \qquad 6\text{-}4$$

where

G_i = local mass flow density
G_{av} = average fuel assembly mass flow density
d_{hi} = local hydraulic diameter
d_{av} = average fuel assembly hydraulic diameter

This equation assumes that the water density and the frictional factor are constant.

Using equation 6-2, equation 6-4, and the methodology of Appendix B of reference (1), it became possible to account for the effects of local flow within the fuel assembly on fuel rod corrosion. A preliminary analysis has been conducted for fuel rods located in different positions within the KWU fuel assembly; all other parameters were maintained constant. The results are given in Table 6-3. The corrosion is compared to that predicted for a rod located in an infinite lattice. For a peripheral fuel rod or for an interior rod not completely surrounded by fuel rods less corrosion is predicted. More corrosion is predicted for an interior fuel rod entirely surrounded by other fuel rods. This analysis suggests that a fuel rod located in a peripheral position in a fuel assembly could corrode up to 20% less than an interior rod operating at the same power level. The analysis conducted is

Table 6-3

PREDICTED VARIATION IN WATERSIDE CORROSION
DUE TO DIFFERENCES BETWEEN SUBCHANNELS WITHIN A FUEL ASSEMBLY

Rod Subchannel Type	Relative Corrosion Film Thickness
Rod in an infinite lattice	1
Inner rod with fuel rods as nearest neighbors	1.01 - 1.06
Inner rod with fuel rods and guide tube as nearest neighbors	0.91 - 0.97
Peripheral rod	0.96 - 1.01
Peripheral rod (peripheral face only)	0.88 - 0.93

preliminary and further effort is required to rigorously quantify the magnitude of the subchannel effects. However, this evaluation suggests that fuel rod corrosion is affected by the particular subchannel occupied and that further analysis of the corrosion data should take this into account.

CIRCUMFERENTIAL TEMPERATURE VARIATIONS

For a fuel rod located in a fuel assembly with a square lattice, the distance to the neighboring fuel rod will vary depending on the circumferential position. The coolant velocity is lowest where the nearest neighbor separation is a minimum. Hence the surface temperature is a maximum at this circumferential position. The minimum surface temperature is expected to be at the circumferential position of maximum neighbor separation. A theoretical analysis indicated that the variation in surface temperature depends inversely on the pitch to diameter ratio (20). In the KWU design the situation is further complicated by the presence of mixing vanes.

Destructive and nondestructive measurements of the oxide layer thickness demonstrate that it varies around the circumference of the fuel rod. If this variation is attributed to circumferential variations in the local surface temperature which are solely caused by variation in the local heat transfer coefficient, (α), then it is possible to assess the magnitude of this variation in α . This analysis is based on the methodology outlined in Appendix B of reference (1) assuming that the corrosion enhancement does not vary with circumferential position. The analysis of ten 3 cycle fuel rods from Reactor A at a total of 51 axial positions where the average oxide layer thickness was more than 40 μm showed that the ratio of minimum to average heat transfer coefficient was 0.8 with a standard deviation of 0.06. This value is higher than measured by Dingee et al. (3) and Presser (4) for similar geometries but is smaller than theoretically predicted by Deissler and Taylor (21).

Work published by Groeneveld (22) deals with local heat transfer effects and needs to be considered in any future developmental effort that may be undertaken.

CONCLUSION

In reference 1 a simple thermal hydraulic model was used to predict waterside corrosion. A more recent evaluation of available thermal hydraulic models has refined the calculation of the heat transfer coefficient α by using an equation to describe N_{u_∞} of the form:

$$Nu = 0.025Re^{0.8}Pr^{0.43}$$

where Pr = Prandtl Number
Re = Reynolds Number
Nu = Nusselt Number for fully developed flow

The axial profile of the oxide layer thickness has a saw-tooth shape. This shape has been attributed to the local flow effects of grids. An expression describing the axial variations in α has been inferred from the data. It is of the form

$$\alpha_x = \alpha_\infty [1 + c/(x/d)]$$

where α_x = local heat transfer coefficient, W/cm^2-K
α_∞ = fully developed heat transfer coefficient, W/cm-K
x = distance from point at upstream edge of spacer grid, cm,
d = hydraulic diameter, cm,
c = constant.

Some preliminary subchannel analyses have been completed. It is concluded that differences between subchannels within a KWU fuel assembly will lead to a variation of up to 20% in the corrosion of a fuel rod operating at a given power level. Further, the variations in flow around the rod circumference may be responsible for the circumferential variation in oxide layer thickness. If this is the case there may be a 20% difference between the average and minimum heat transfer coefficient.

REFERENCES

1. F. Garzarolli, D. Jorde, R. Manzel, G. W. Parry and P. G. Smerd. "Review of PWR Fuel Rod Waterside Corrosion Behavior", RP 1250-01. Task A. Combustion Engineering, Inc., June 1979, CE NPSD-79, August 1980, EPRI NP-1472.

2. F. Garzarolli, R. Manzel, P. Suchy and J. R. Politano. CE/KWU/EPRI "Recent PWR Waterside Corrosion Data Acquisition and Review of Clad Surface Temperature Calculation", RP 1250-01. Combustion Engineering, Inc., June 1981, CE NPSD-140.

3. D.A. Dingee, W.B. Bell, J.W. Chastain and S.L. Fawcett, "Heat Transfer From Parallel Rods in Axial Flow", Battelle Memorial Institute, BMI-1026, 1955.

4. J.L. Wantland, "Compact Tubular Heat Exchangers", Reactor Heat Transfer Conference of 1956.

5. K. Presser, "Warmeubergang und Druckverlust an Reaktorbrennelementen in Form langsdurchstromter Rundstabbundel D82", Dissertation, TH Aachen.

6. J.L. Wantland and R.L. Miller, "Heat Transfer in Septafoil Geometries by Mass Transfer Measurements", ORNL 59-6-9, 1959.

7. D. Palmer and L. Swanson, "Measurement of Heat Transfer Coefficients Friction Factor and Velocity Profiles for Air Flowing Parallel to Closely Spaced Rods", Reactor heat transfer Conference of 1956, p 535.

8. V.I. Subbotin, P.A. Ushakov and B.N. Gabrianovich, "Hydraulischer Widerstand bei durch Flussigkeiten langsumstromten Stabbundeln", Kernenergie 4. Jahrg., H. 8, 1961.

9. P.I. Khristenko, P.A. Petrov, and V.A. Mitropolevsky, "Rod Fuel Element for a Gas Cooled Heavy Water Power Reactor", Genfer Bericht P 2053, 1956.

10. W.A. Sutherland and W.M. Kays, "Heat Transfer in Parallel Rod Arrays", GEAP 4637, 1965.

11. P. Miller, J. Byrnes and D. Benforado, "Heat Transfer to Water Flowing Parallel to a Rod Bundle", A.I.Ch.E. Journal, Vol. 2, No. 2, 1956.

12. R.E. Grimble, W.H. Bell, and S.L. Fawcett, "Heat Transfer and Friction Flow Characteristics of Cylindrical Parallel Rods With Transverse Cylindrical Spacers", AECD-3975, 1954.

13. H.W. Hoffman, J.L. Wantland, and W.J. Stelzman, "Heat Transfer With Axial Flow in Rod Clusters", Reactor Heat Transfer Conference of 1956, p 553-560.

14. A. Inayotov and M.A. Uikheyev, "Heat Transfer in Longitudinally Wetted Banks of Tubes", Teploenergetika Nr. 3, 1957.

15. J. Weisman, Journal of Nuclear Science and Engineering 6 , 79, 1959.

16. M.A. Michejev, "Grundlagen der Warmeubertragung", V.E.B., Verlag Technik, Berlin, 2. Auflage.

17. G. Grass, "Warmeubergan an turbulent stromende gase im Rohreinlauf", Allgemeine Warmetechnik, 7. Jahrg., H. 3, p 58-64, 1956.

18. U. Stiefel, Proc. Reaktortagung Bonn (1971), p146.

19. D. S. Rowe, BNWL-1695, 1975.

20. P. Suchy, G. Ulrych, H. Kemner and E. Kurz. "Applications of Critical Heat Fluxes to Rod Bundles", European Nuclear Conference, Hamburg, 1979.

21. R. G. Deissler and M. F. Taylor. "Analysis of Axial Turbulent Flow and Heat transfer Through Banks of Rods or Tubes", Reactor Heat Transfer for Conference of 1956, TID 7529, 1957.

22. D. C. Groeneveld. " Forced Convective Heat Transfer to Superheated Steam in Rod Bundles", AECL-4450, April 1973.

23. P. Dittus and G. Boelter. Heat and Mass Transfer , McGraw-Hill Book Co., 1059.

24. A.P. Colburn, "A Method of Correlating Forced Convection Heat Transfer Data and a Comparison With Fluid Friction", Transactions of the American Institute of Chemical Engineers, 29 , 1933.

25. H. Hausen, "Neue Gleichungen fur die Warmeubertragung bei freier oder erzwungener Stromung", Allgemeine Warmetechnik, Band 9, 1959 (Nr 4/5).

26. W.L. Friend and A.B. Metzner, "Turbulent Heat Transfer Inside Tubes", Journal of the American Institute of Chemical Engineers, 4 , 1958.

Section 7

ANALYSIS OF OXIDE THICKNESS DATA

INTRODUCTION

The oxide film thickness data obtained from reactors A-F have been discussed qualitatively in Section 3. There are differences in corrosion behavior from reactor to reactor. This variation in behavior has been attributed to several factors, including

- fuel and power history,
- reactor thermal hydraulic designs,
- reactor coolant chemistry
- cladding lot to lot variability,

and

- measurement error.

This section presents the analysis of the oxide layer data and a corrosion model. This analysis should provide a basis from which to assess the influence of other factors such as reactor coolant chemistry. There are very few data from Reactor B, while data from Reactor F have only recently become available. These data have not yet been analyzed.

The data from reactor A are compared with the in-pile model of Dalgaard (1) and the out-of-pile model of Stehle (2) in Figures 7-1 and 7-2, respectively. Both models underpredict the data. The difference between the observed corrosion and the predictions of the latter model were explained on the basis that irradiation enhances corrosion and that the model is based on unirradiated corrosion data (2). These models also underpredict corrosion in Reactor C, D and E.

In previous analyses of PWR corrosion data (3) a corrosion model had been used which is based on ex-reactor models developed by Stehle (3) and Dyce (4). A fitting factor was used to account for the increase in corrosion observed in PWRs. This approach has been used briefly in section 6 that discussed localized thermal hydraulic effects. More recently a trend analysis has been conducted using data from reactors A, C, D, and E. A preliminary corrosion model describing the

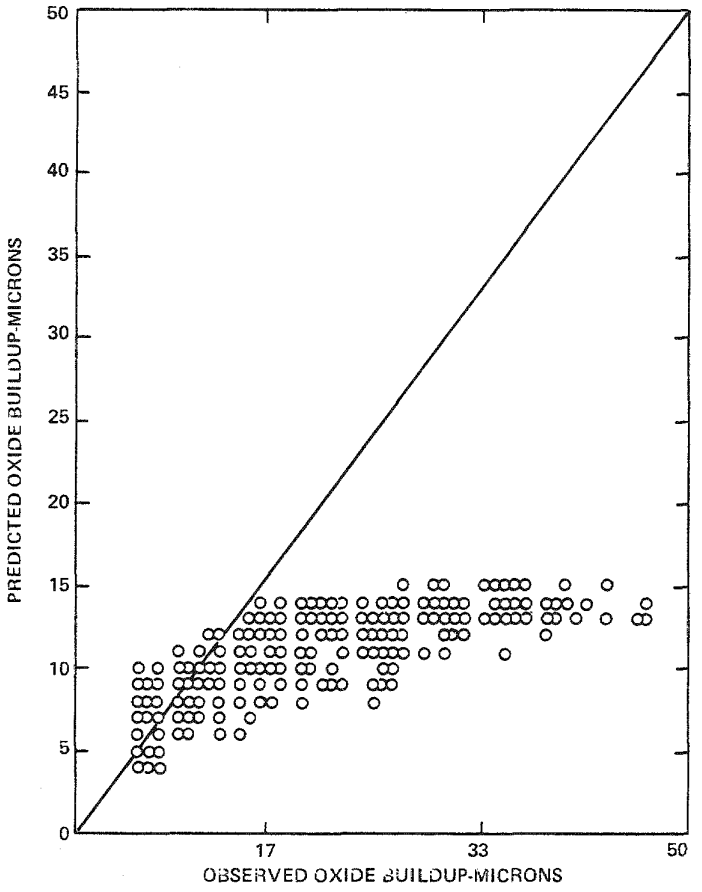

Figure 7-1. Comparison of the Predictions of the Dalgaard Model with Reactor A Corrosion Observations

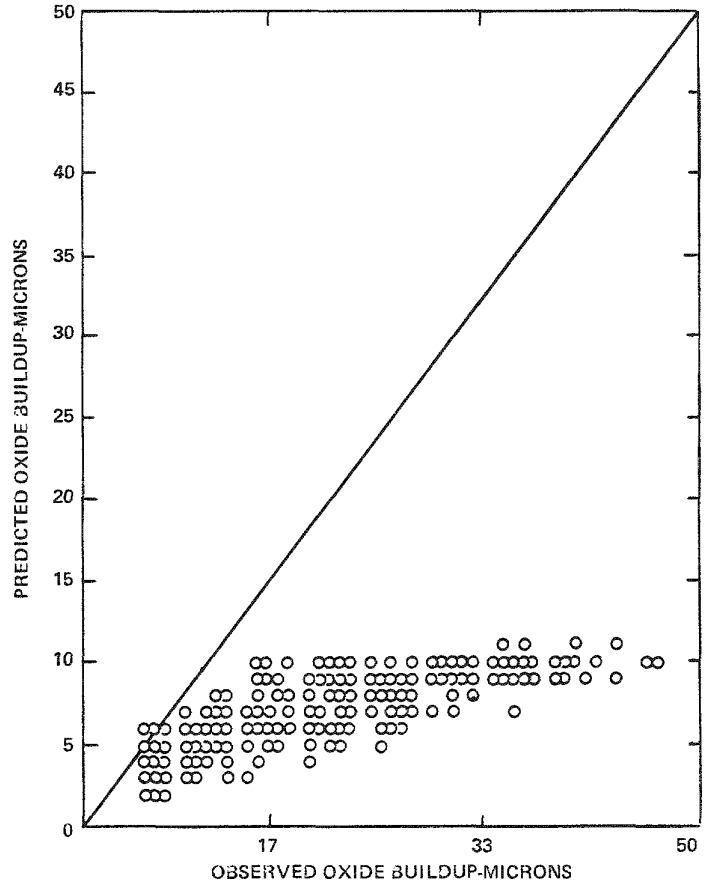

Figure 7-2. Comparison of the Ex-Reactor Stehle Corrosion Model with the Reactor A Corrosion Observations

corrosion in PWRs was then developed and optimized using a statistical least squares approach. The results of the more recent analyses are presented in the following sections.

STATISTICAL ANALYSIS METHODOLOGY

The methodology used to develop the new corrosion model is summarized in Figure 7-3. The corrosion layer thickness data obtained from the present program have been stored in a computer data bank. These data are presented in Part 2 of this report. In addition this data base, (Item A), contains the associated rod average power and time history (Table 2-2) on a cycle by cycle basis, the rod burnup and the key reactor design parameters such as inlet temperature (Table 2-3), mass flow rate, and the reactor pressure (Table 2-1). Only data well away from grids were used in the development of the corrosion model. Corrosion at these positions is not expected to be affected by local turbulence at the grids.

Based on these data the "simulator" computer code, (Item B), is able to calculate the temperature at the metal-oxide interface just prior to the shutdown when the oxide film measurements were made. The simulator can also calculate the associated temperature-time history given a particular corrosion model. As shown in section 6, the axial variation in oxide layer thickness close to grids can be predicted using a more complete thermal hydraulic model. This model accounts for variations in the local heat transfer coefficient due to grid effects and variations due to changes in local water temperature. Since the development of a more complex thermal hydraulic model was outside the scope of the program, the simpler thermal hydraulic model outlined in (2), which assumes that α is a constant for a given reactor, was used.

The data were subjected to several statistical evaluations in order to determine the major variables controlling in-reactor corrosion and to obtain their functional form. In these analyses several approximations were made. For multi-cycle fuel rods a time-average heat flux was computed as an approximation of the more complex power-time history. During the corrosion process the temperature at the metal-oxide interface will vary depending, among other things, on the precise power history and the local oxide layer thickness. The temperature at the metal-oxide interface just prior to the oxide layer measurements was used to provide an indication of the more complex temperature-time history. The time-average corrosion rate and the oxide layer thickness were the two dependent variables evaluated.

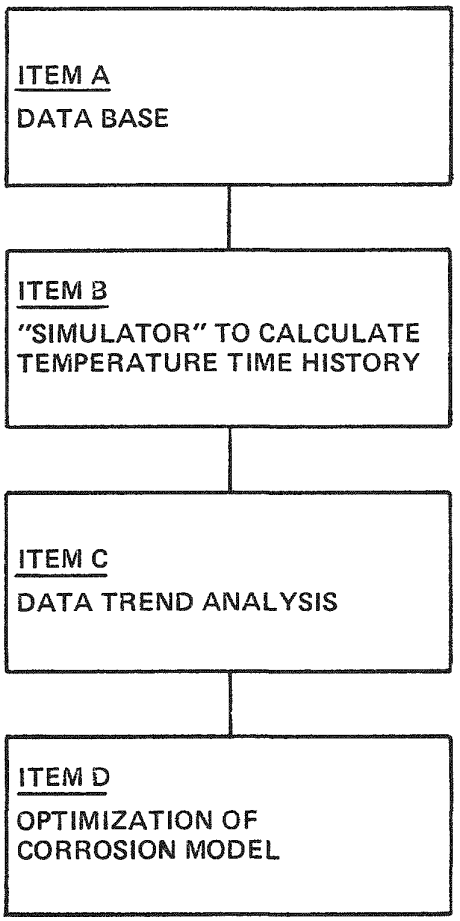

Figure 7-3. Methodology Used to Develop the Corrosion Model

A factor screening analysis was conducted on this modified data base (Item C) in order to assess the relative importance of the variables evaluated. This forces a linear dependence between the dependent variable (oxide layer thickness or corrosion rate) and the variable of interest. The coefficient of correlation for each parameter (5) provides an assessment of its relative importance. It varies from 0 to 1 and the closer the coefficient is to unity the greater is the importance of that particular variable.

A pairwise correlation analysis was also conducted (Item C) to obtain an indication of the functional relationship that exists between the dependent variables and the more important independent variables identified by the correlation coefficient analysis. In this analysis the computer evaluated the effect of a particular independent variable by dividing its range into 15 equal increments and then calculating the average corrosion layer thickness or average corrosion rate associated with each particular increment. The results were plotted to provide an indication of the possible functional relationships. The Bartlett test (6) was used to assess whether or not the relationship was fortuitous - a value for the Bartlett test parameter of >0.03 indicates that there is a strong relationship.

Having obtained the approximate functional dependencies, a statistical least squares analysis was conducted to develop a best estimate predictor of the data (Item D). The computer code considers the differential form of the corrosion equations. It is able to calculate the local metal/oxide interface temperature based on the local oxide thickness, the detailed power history as a function of time and the reactor design parameters. The code then performs an integration using these parameters. A Monte Carlo analysis approach (8) was used to arrive at the optimum values for the constants in the equations.

7.3 RESULTS

The results of the screening analysis are presented in Table 7-1. It can be seen that the corrosion rate is strongly dependent on the temperature and that the corrosion rate is only weakly dependent on the burnup, heat flux or modified heat flux. The burnup is approximately proportional to the fast neutron fluence*.

---

* A regression analysis of data from physics calculation gave:

$\emptyset = 1.182 \times 10^{-2} + 1.5197 \times 10^{-1} B + 1.4605 \times 10^{-3} B^2 - 6.542 \times 10^{-6} B^3$

where $\emptyset$= neutron fluence x 10^{-21} n/cm^2 (E>0.821 MeV) B= burnup (GWd/t)

Table 7-1

RELATIVE IMPORTANCE OF VARIABLES

Parameter	Correlation Coefficient	
	Corrosion Rate	Oxide Layer Thickness
Time	0.1	0.53
Temperature	0.66	0.43
Burnup	0.21	0.55
Heat Flux	0.24	0.1
Neutron Flux*	0.24	0.23

* This is assessed by means of a parameter called the "modified heat flux".

The heat flux is approximately proportional to the fast neutron flux. Since the heat flux also causes the temperature at the metal/oxide to increase, a new parameter "modified heat flux" was developed in which the effect due to temperature was removed and the residual reflects additional effects such as neutron flux. However the change in modified heat flux reflecting the change in fast neutron flux does not appear to have a strong influence on the corrosion of the PWR fuel examined. The oxide layer thickness is also strongly influenced by the metal-oxide interface temperature as well as exposure time or burnup.

The key results of the pairwise correlations are presented in Figures 7-4 to 7-8. The dependencies shown are strong as determined by the Bartlett test (6). The dependence of oxide layer thickness on exposure time indicates an incubation period where a low corrosion rate was followed by more rapid corrosion rate. This is in agreement with the experimental results of other corrosion programs which show an incubation period or pretransition region which may be described by cubic kinetics. This region is followed by a period of more rapid kinetics in which corrosion is linear with time.

The dependence of corrosion rate on temperature is strong, Figure 7-5. A linear relationship with absolute temperature, or an exponential relationship with reciprocal of absolute temperature, are both equally promising although the latter is expected from classical corrosion theory, Figure 7-5. There is a somewhat weak dependency of the corrosion rate on the modified heat flux, a measure of the dependency on the fast neutron flux, Figure 7-6. Also shown for completeness is the dependency of corrosion film thickness on burnup, Figure 7-7. The correlation is actually better than that with exposure time, probably because this burnup parameter reflects the effect of both time and power (temperature).

Based on these analyses it is concluded that the time and temperature dependencies utilized to describe classical ex-reactor corrosion are also applicable to in-reactor PWR corrosion. These equations are:

Pre-transition corrosion

$$dS/dt = (A/S^2) \exp(-Q_1/RT) \qquad 7\text{-}1$$

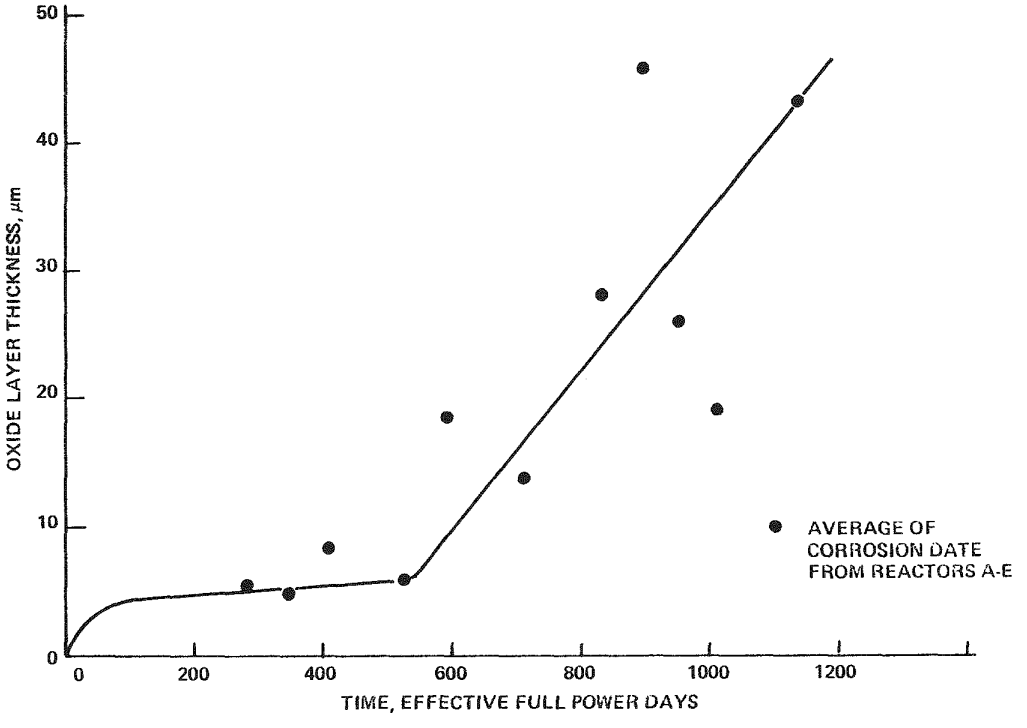

Figure 7-4. Time Dependence of Corrosion (Pairwise Correlation)

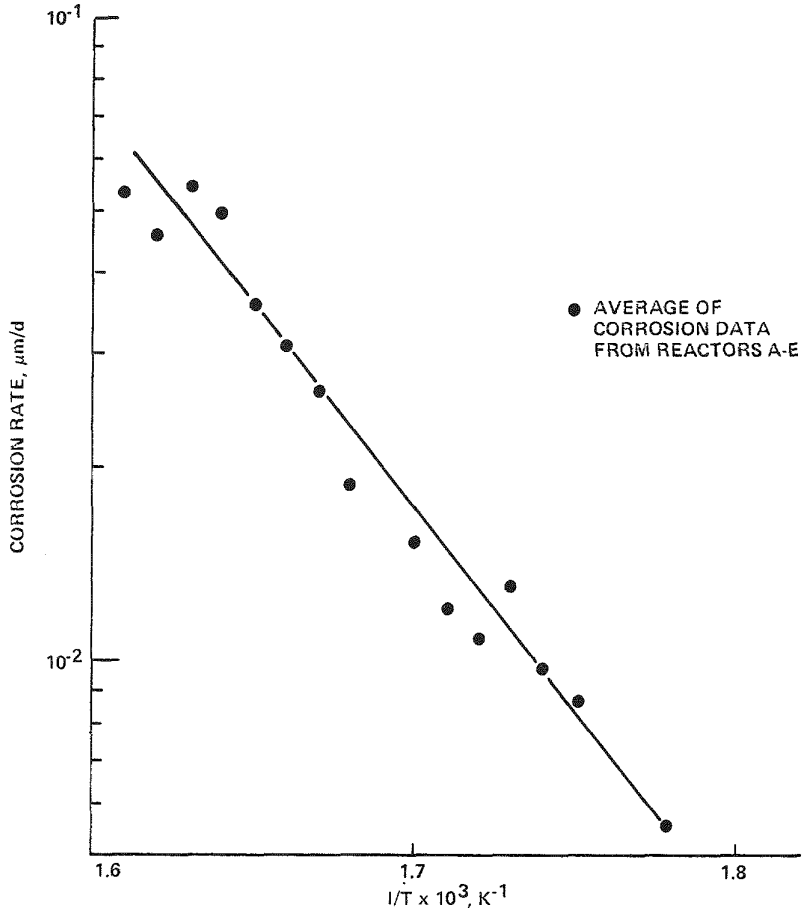

Figure 7-5. Temperature Dependence of Corrosion (Pairwise Correlation)

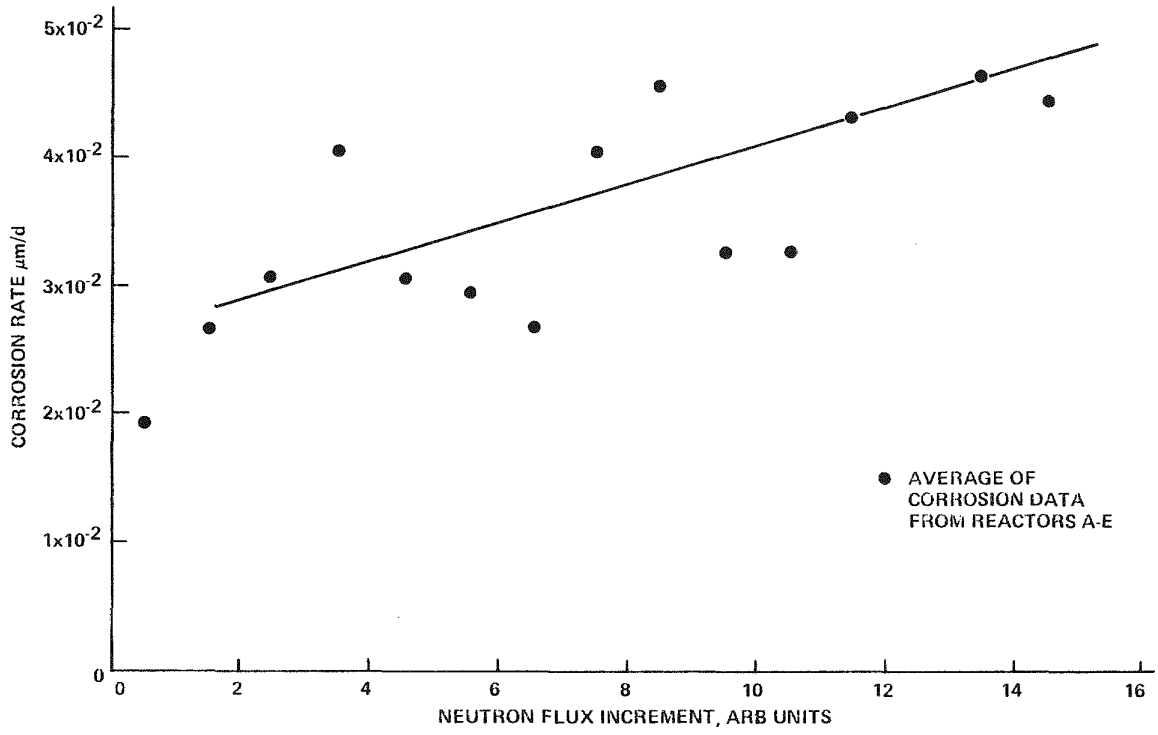

Figure 7-6. Neutron Flux Dependence of Corrosion (Pairwise Correlation)

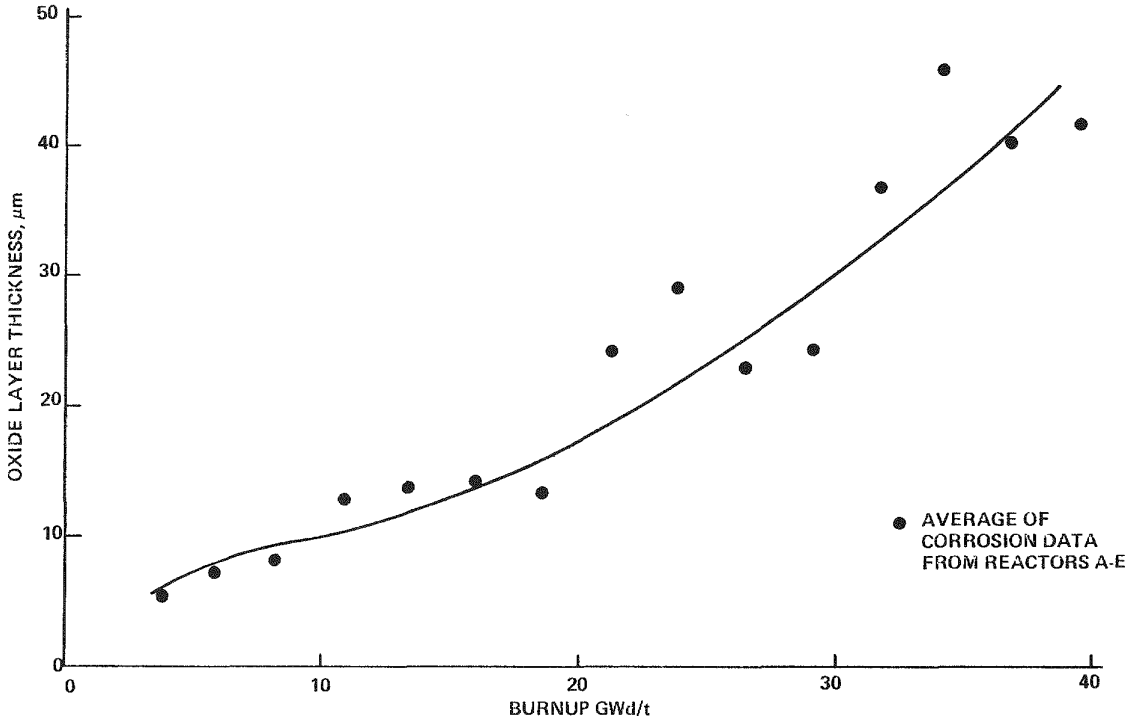

Figure 7-7. Burnup Dependence of Corrosion (Pairwise Correlation)

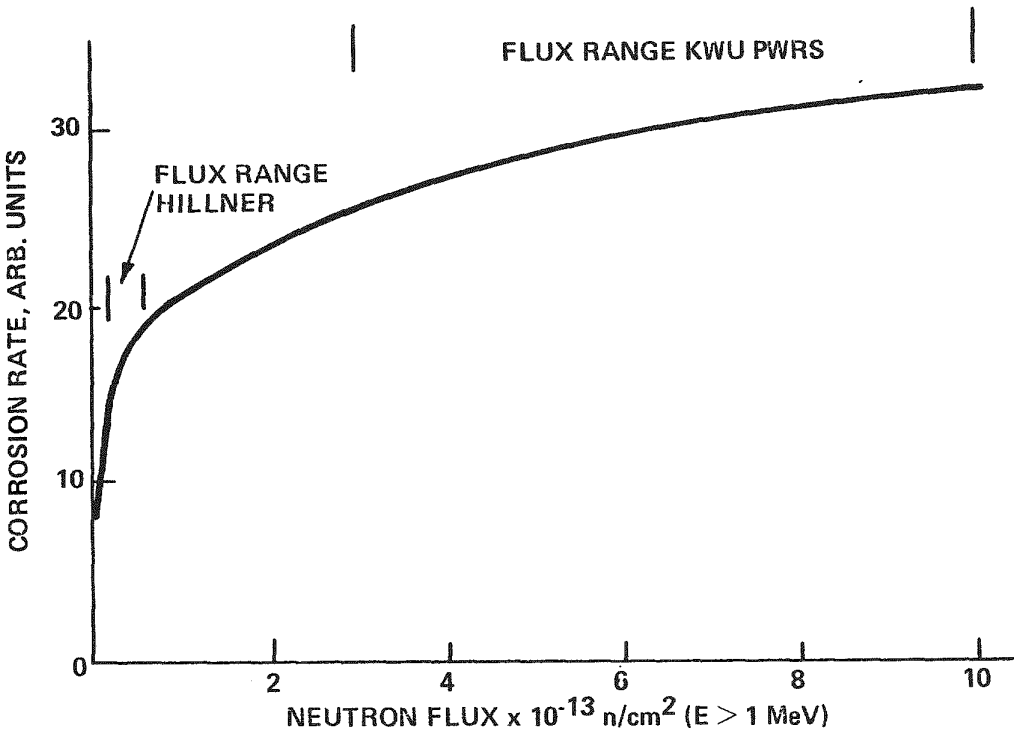

Figure 7-8. Flux Dependence of Corrosion (Temperature Constant)

Post-transition corrosion

$$dS/dt = C\exp(-Q_2/RT) \qquad 7\text{-}2$$

Thickness at transition

$$S_t = D \exp(-Q_3/RT - ET) \qquad 7\text{-}3$$

where dS/dt = corrosion rate

S = oxide layer thickness (μm)

T = metal/oxide interface temperature (K)

B, D, and E are constants

A, C are parameters which are a function of the fast neutron flux.

Based on an analysis of the PWR corrosion data it appears that post-transition corrosion is about 2-3 times that found ex-reactor. The pairwise analysis showed that the corrosion rate was not that sensitive to changes in fast neutron flux for fluxes ranging from 3 to 10 x 10^{13} n/cm^2-sec (E>0.821 MeV). Hillner (7) found a linear dependence of post-transition corrosion rate on fast neutron flux for fluxes in the narrow range 2.5 - 5 x 10^{12} n/cm^2-sec. However since the enhancement relative to Hillner's ex-reactor equation ranged from 1.5-3.5 it is proposed that the flux dependency of post-transition corrosion rate be of the form

$$C = C_o + U(M\,\emptyset)^P \qquad 7\text{-}4$$

where $\emptyset$ = fast neutron flux

C_o, U, M and P are constants

The general form of the equation is given in Figure 7-8. (It was actually generated using the final optimization constants of Table 7-2). Also shown are the range of fast neutron fluxes for the present corrosion program and that of Hillner (7). The pre-exponential factor A in equation 7-1 was assumed to be constant and not dependent on the fast neutron flux. This is based on Hillner's observations (7) which show that the pre-transition kinetics were not influenced by irradiation. For this same reason the equation which is used to calculate the oxide layer thickness at transition, equation 7-3, is based on the analysis of ex-reactor corrosion data conducted by Stehle (3). The activation energy for the pre-transition equation

was not included in the optimization for similar reasons and because the pre-transition corrosion data encompass a rather narrow temperature range.

The least squares Monte Carlo analysis of the corrosion data optimized the remaining constants A, Q_2, C_0, U, M and P. In an analysis of some of the early Reactor A data and in an analysis of some of the early reactor C, D and E data combined, it was found that the pre-transition constant A was almost identical. A further evaluation of the later reactor D data also showed this to be the case.

A least squares fit of the early reactor A data and an independent fit to the later reactor D data gave almost identical correlations. The constants are given in Table 7-2. The observed versus predicted data plots are given in Figure 7-9 and 7-10. The predictions of this same model for reactors C and E are shown in Figure 7-11 and 7-12 where it can be seen that corrosion is overpredicted.

DISCUSSION

The corrosion model described in the results section is based on the trend analyses of the KWU corrosion data which span burnups of up to 45 GWd/t, times of up to 1446 EFPD, powers ranging from 45 to 338 W/cm and neutron fluences of 3 to 9 x 10^{21} n/cm^2 (E>0.821 MeV). The preponderance of the data were obtained from reactors A and D. A least squares fit of data from Reactor A yielded an identical best estimate model to one obtained from a fit of data from Reactor D. This model overpredicts the data from Reactors C and E.

The extent of under-prediction or over-prediction may be measured by the mean ratio of oxide thickness observed/oxide thickness predicted, which is shown in Table 7-3 for each reactor examined. For Reactors A and D the average ratio of observed to predicted oxide layer thickness is close to 1.0 (0.98 for Reactor A and 0.94 for Reactor D). However for Reactors C and E these ratios are 0.5 and 0.74 respectively. These values are significantly different from unity. Interestingly, the reactors which behave similarly, and where the model predicts the extent of corrosion correctly, are the two low inlet temperature plants. The reactors where corrosion is over-predicted by the equation are the two high inlet temperature plants. Of course it is also possible that this difference in corrosion behavior from reactor to reactor may be due to local variations in coolant chemistry. Certainly the analysis presented in section 5 concludes that impurities present in the bulk coolant are in concentrations too low to have caused the in-reactor corrosion enhancement. The apparent variation may be a consequence of the

Table 7-2

OPTIMUM CORROSION EQUATION CONSTANTS

Constant	Value
A	6.3×10^{9} $(\mu m)^3$ d^{-1}
Q_1	32289 (cals/mol)
Co	8.04×10^{7} (μm) d^{-1}
U	2.59×10^{8} (μm) d^{-1}
M	7.46×10^{-15} $(cm^2\text{-sec/n})$
P	0.24
Q_2	27354 (cals/mol)
D	2.14×10^{7} (μm)
Q_3	10763 (cals/mol)
E	1.17×10^{-2} (K^{-1})

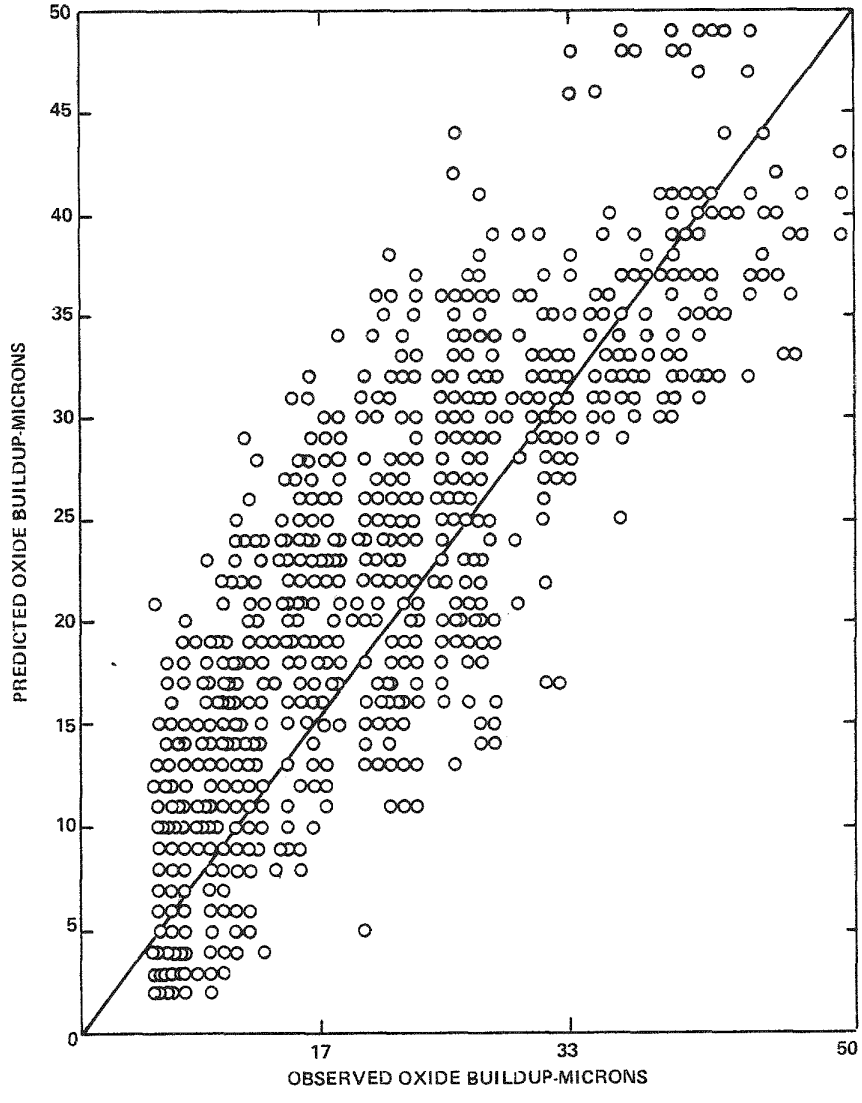

Figure 7-9. Comparison of the Corrosion Predictions of Equations 7-1 to 7-4 with the Reactor A Observations

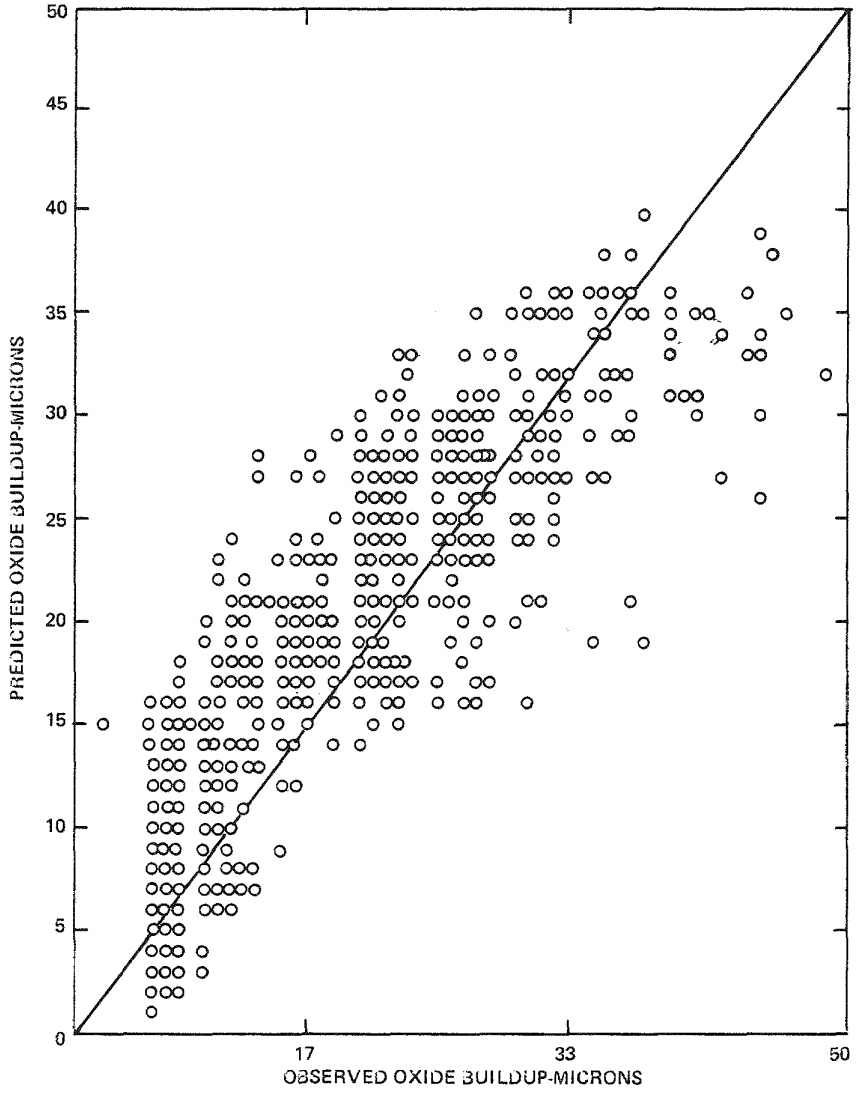

Figure 7-10. Comparison of the Corrosion Predictions of Equations 7-1 to 7-4 with the Reactor D Observations

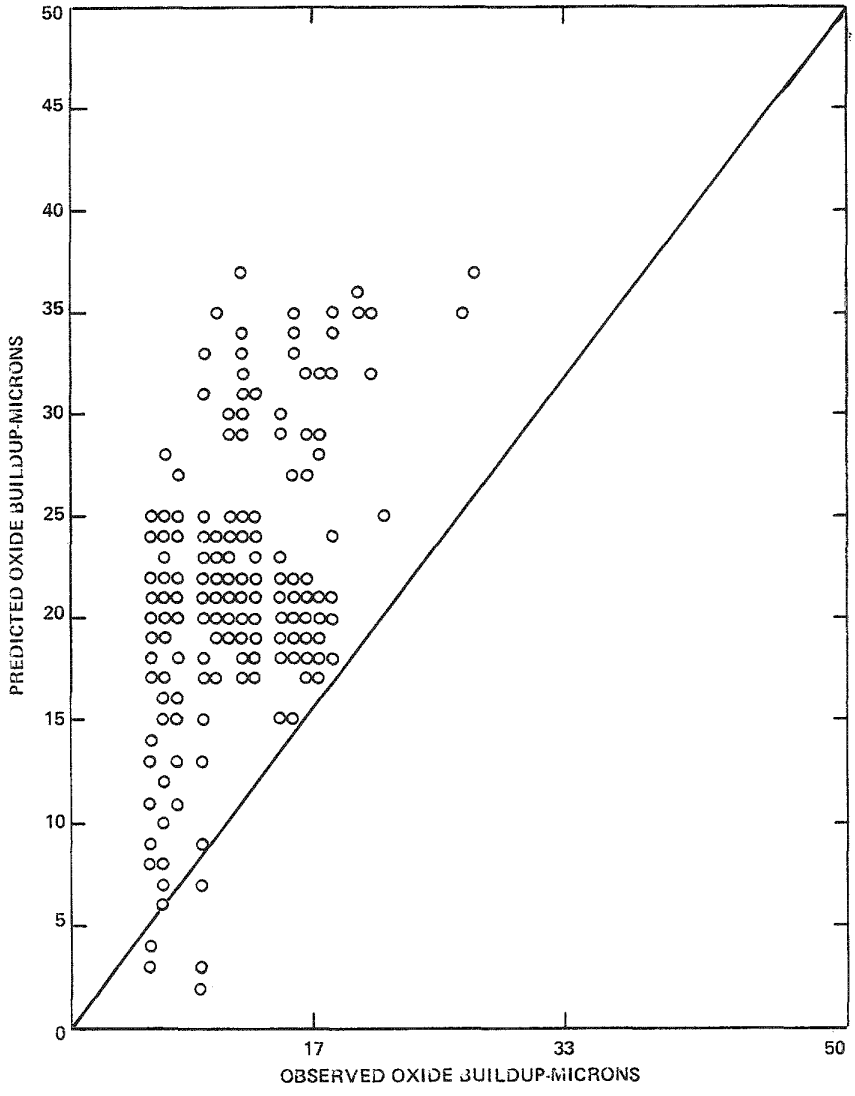

Figure 7-11. Comparison of the Corrosion Predictions of Equations 7-1 to 7-4 with the Reactor C Observations

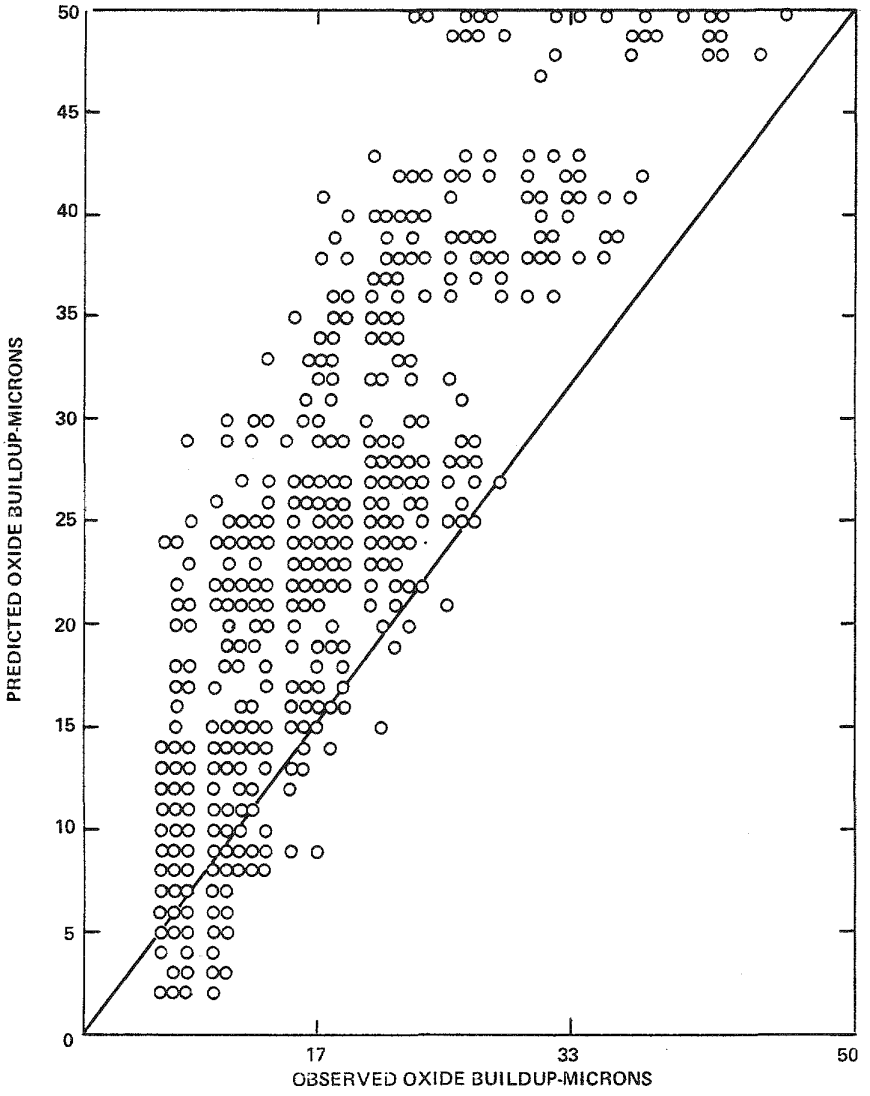

Figure 7-12. Comparison of the Corrosion Predictions of Equations 7-1 to 7-4 with the Reactor E Observations

Table 7-3

COMPARISON OF MODEL PREDICTIONS FOR THE
DIFFERENT REACTORS EXAMINED

Reactor	Average Ratio $S_{observed}/S_{predicted}$	Number of Data Points	Inlet Temp. (°C)	Fuel Assembly Type	No. of Grids	Coolant Flow Rate KG/S, Rod
A	0.98	1329	281 - 284	14X14	8	0.292
C	0.50	295	289	15x15	7	0.375
D	0.94	1127	283	16x16	9	0.426
E	0.74	942	290 - 291	15x15	7	0.393

simplified thermal hydraulic assumptions made during this analysis. One major simplification which would explain the variation is the assumption that there is a sudden transition from forced convection to nucleate boiling heat transfer. In fact, this transition is gradual and could begin at heat fluxes substantially below the computed heat flux at which nucleate boiling begins. Explicit treatment of this transition region would yield lower clad temperatures for fuel rods operating at high power levels. However it is beyond the scope of the present program to examine the use of more refined thermal hydraulic models in conjunction with the statistical approach described here. The corrosion model appears to be a good predictor of the corrosion behavior of fuel rods in Reactors A and D, but it should be used with caution in predicting the corrosion performance of fuel rods in plants having higher inlet temperatures. It is interesting to note that the model overpredicts the amount of oxide buildup for the high coolant inlet temperature plants.

The corrosion model tends to modestly overpredict corrosion in Reactors A and D for oxides up to 25 μm thick and to underpredict corrosion for thicker oxides. This can be seen in Figure 7-13. Recent long term ex-reactor corrosion tests conducted by Peters (8) also showed that, for a given test temperature, the corrosion rate depends on the oxide layer thickness.

CONCLUSIONS

A corrosion model has been developed to describe the corrosion of KWU fuel rods. It is able to accurately predict the corrosion performance of Reactors A and D. The model tends to overpredict the corrosion of Reactors C and E. The differences in corrosion performance may be due to reactor to reactor variations in coolant chemistry. However it is possible that the inability to predict the corrosion behavior is a consequence of the simplified thermal hydraulic model which has been used. Further effort on this subject appears to be advisable.

It appears that development is warranted for a more sophisticated thermal-hydraulic model that explicitly accounts for local flow patterns and heat transfer effects due to grids and subchannel variations as well as a more accurate treatment of the transition between forced convection and boiling heat transfer. For plants which have crud present in the coolant it will be necessary to provide a more explicit treatment of its effects.

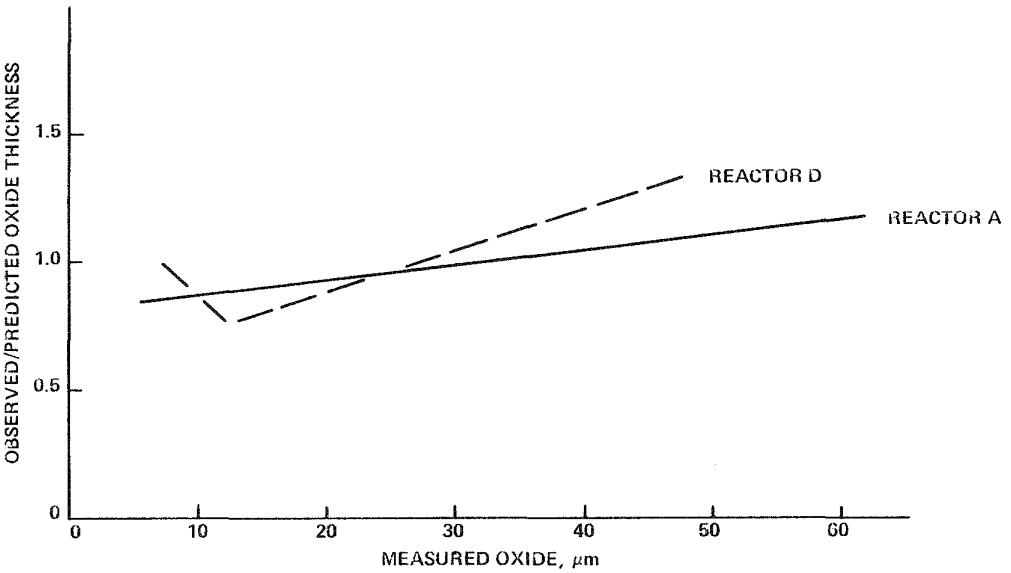

Figure 7-13. The Interrelationship Between Measured Oxide Film Thickness and the Bias in the Prediction of Corrosion

REFERENCES

1. S. B. Dalgaard, "Long-Term Corrosion and Hydriding of Zircaloy-4 Fuel Clad in Commercial Pressurized Water Reactor with Forced Convective Heat Transfer"Presented at the Electrochemical Society, Inc. Washington, D.C., May 1976.

2. F. Garzarolli, D. Jorde, R. Manzel, G.W. Parry, and P.G. Smerd "Review of PWR Fuel Rod Waterside Corrosion Behavior", EPRI NP-1472, August 1980.

3. H. Stehle, W. Kaden and R. Manzel. "External Corrosion of Cladding in PWR's" Nuclear Engineering and Design, Vol. 33, 1975, pp 155-169.

4. I. H. Dyce, "Corrosion of Zircaloy Fuel Cladding - The Influence of High Heat Fluxes." Nuclear Engineering, Vol. 9, 1964, pp 253-255.

5. E. L. Filshtein, C-E, Private Communication, January 1982.

6. O. L. Davies and P. L. Goldsmith, "Statistical Methods in Research and Production" Published by Imperial Chemical Industries Ltd. London 1976.

7. E. Hillner, "Long-term In-reactor Corrosion and Hydriding of Zircaloy-2 Tubing Zirconium in the Nuclear Industry, Ed. D.G. Franklin, ASTM STP-754, 1982.

8. H. R. Peters, "Improved Characterization of Aqueous Corrosion Kinetics of Zircaloy-4" presented at the 6th International Conference on Zirconium in the Nuclear Industry, Vancouver, British Columbia, Canada 28 June - 1 July 1982.